FINITE ELEMENT MODELING OF REINFORCED CONCRETE COLUMNS SUBJECTED TO AIR AND UNDERWATER EXPLOSIONS

by

Getu Zewdie Abyu
A Thesis
Submitted to the
Graduate Faculty
of
George Mason University
in Partial Fulfillment of
The Requirements for the Degree
of
Master of Science
Civil and Infrastructure Engineering

Committee:

G. P. Urgessa	Dr. Girum Urgessa, Thesis Director
Doaa Bondok	Dr. Doaa Bondok, Committee Member
	Dr. David Lattanzi, Committee Member
	Dr. Elise Miller-Hooks, Interim Department Chair

Date: July 28, 2023

Summer Semester 2023
George Mason University
Fairfax, VA

Finite Element Modeling of Reinforced Concrete Columns Subjected to Air and Underwater Explosions

A Thesis submitted in partial fulfillment of the requirements for the degree of Master of Science of Civil and Infrastructure Engineering at George Mason University

by

Getu Zewdie Abyu
Bachelor of Science
Jimma University, 2009

Director: Girum Urgessa, Associate Professor
Sid and Reva Dewberry Department of Civil and Infrastructure Engineering

Summer Semester 2023
George Mason University
Fairfax, V

DEDICATION

To my beloved wife Honey, my stylish and young scholar daughter Loza, and my genius son Nolawi,

This thesis is dedicated to you with heartfelt appreciation and boundless love. Throughout this academic journey, your unwavering support, understanding, and encouragement have been the guiding light that propelled me forward.

Honey, you have been my rock, my confidante, and my source of strength. Your love and belief in me have given me the courage to overcome challenges and pursue my dreams. Thank you for standing by my side, cheering me on every step of the way.

Loza, my stylist, your innate sense of fashion and impeccable taste have guided my journey with a radiant glow. You are my young scholar, your thirst for knowledge, unwavering dedication to academic excellence, and intellectual curiosity will see its flame within you. Nolawi, my brilliant son, your relentless pursuit of knowledge and your endless curiosity inspire me to be a better version of myself. Your inquisitive nature and thirst for understanding the world around you remind me of the importance of lifelong learning.

To my dear family, I am profoundly grateful for your patience during late nights, your understanding during moments of intense focus, and your unyielding belief in my abilities. You have been my anchor, providing the love, warmth, and stability that fuel my determination.

This thesis represents not only my academic achievements but also the collective triumph of my family. It stands as a testament to the love, sacrifices, and unwavering support that you have showered upon me.

ACKNOWLEDGEMENTS

During my thesis journey, I have been profoundly grateful and deeply appreciative for the divine guidance, unwavering support, and limitless strength bestowed upon me by the Almighty God of Israel. With heartfelt sincerity and deepest reverence, I acknowledge the tremendous role that God has played in shaping my path and ensuring my triumph throughout this extensive endeavor, and I am forever grateful to God.

I would like to express sincere gratitude to my advisor, Dr. Girum Urgessa, for granting me the invaluable opportunity to undertake this thesis research under his guidance and supervision. I will never forget his unwavering support, kindness and inclusive thoughts and remarkable flexibility in accommodating my constantly evolving schedules. I would also like to acknowledge Dr. Bondok and Dr. Lattanzi for graciously agreeing to serve on my thesis committee.

I extend my heartfelt gratitude to Mr. Ameen Topa, a research collaborator from Universiti Malaysia Terengganu, for his unwavering support in the numerical simulation efforts. I am consistently impressed by his exceptional professionalism, renowned expertise on a global scale, timely contributions, as well as his humble and supportive nature. His invaluable assistance and collaborative spirit have greatly contributed to the success of the numerical simulations, and I am truly grateful for his dedication and expertise throughout the research process.

I am deeply grateful to my beloved wife Honey, my lovely daughter Loza, and my son Nolawi for their immense patience and understanding during the extended period of my thesis research work. Throughout this demanding journey, they selflessly supported me, sacrificing our family time and enduring my absence.

I would like to extend my sincere gratitude to my extended family members, friends, and relatives for their continued encouragement throughout my thesis journey. I am particularly grateful to my brothers-in-law, Fikireslase and Tesfamichael, and of course, my deep gratefulness must also go to my caring and loving immediate elder brother, Showie, for his valuable advices and encouragements he nourished me. I would also like to express my gratitude to my dear friend Muluken for his invaluable technical support during my thesis work.

TABLE OF CONTENTS

Page

LIST OF TABLES

LIST OF FIGURES

Figure **Page**

LIST OF EQUATION

Equation **Page**

LIST OF ABBREVIATIONS

Underwater Explosion .... UNDEX
Reinforced Concrete ....RC
Concrete-Filled Circular Steel Columns ....CFCSC
Steel Fiber-Reinforced Concrete..SFRC
Trinitrotoluene...TNT
Ultra-High Performance Cementitious Composite Filled Steel Tube……….. ...UHPCC-FST
Fiber-Reinforced Plastic ....FRP
Arbitrary Lagrangian-Eulerian.. ALE
Hurricane Boundary..HBL
Smoothed Particle Hydrodynamics.. SPH
Dynamic Increase Factor .... DIF
Comite Euro-International du Beton...CEB
Johnson & Holmquist .... JH
Riedel-Hiermaier-Thoma..RHT
Ramberg-Osgood .... RO
Johnson-Cook...JC
Particle-In-Cell ....PIC
Computational Fluid Dynamics...CFD
Computational Structure Mechanics.. CSM
Fluid-Structure Interactions...FSI
Ordinary Differential Equation ....ODE
Courant-Friedrichs-Lewy .... CFL
Concrete-Filled Steel Tubes ....CFST
Federal Emergency Management Agency.. FEMA
Fiber-Reinforced Plastic ....FRP
Underwater Shock Analysis ....USA
Coupled Lagrangian and Eulerian... CLE
Equation of State .... EOS
Johnson & Holmquist .... JH
Riedel-Hiermaier-Thoma..RHT
Johnson-Cook...JC
Jones, Wilkins, and Lee ....JWL
Fluid-Structure Interactions...FSI
Livermore Software Technology Corporation ....LSTC

ABSTRACT

FINITE ELEMENT MODELING OF REINFORCED CONCRETE COLUMNS SUBJECTED TO AIR AND UNDERWATER EXPLOSIONS

Getu Abyu, M.S.

George Mason University, 2023

Thesis Director: Dr. Girum Urgessa

Ever since the tragic events of the 9/11 attacks in New York, global infrastructures have suffered significant damage caused by acts of terrorism, military strikes, and accidental explosions. Coastal regions and critical infrastructure, including bridges, face a significant threat from maritime terrorism. Furthermore, intentional car bomb explosions in acts of terrorism and military assaults also pose substantial risks to the structural integrity of bridges. Among the various components comprising a bridge structure, bridge piers play a crucial role in providing vertical support. Hence, it is crucial to study the structural response of reinforced concrete (RC) columns under blast loading.

This study involved the development of two comprehensive numerical models, using LS-DYNA software, to analyze the air blast and underwater explosion (UNDEX) responses of RC columns. The validation process entailed comparing the simulation results with experimental data obtained from previous studies by Yuan et al. (2017), Yang et al. (2019), and Zhuang et al. (2020). Both numerical models exhibited reasonably good agreement with the experimental findings, demonstrating their reliability in replicating real-world air blast and UNDEX scenarios. With the numerically calibrated and verified

UNDEX model, a parametric study was conducted to examine the effects of blast loads from TNT explosive charges on RC columns. The study considered various parameters, including stand-off distance, charge weight, and water depth. Nonlinear finite element analysis using LS-DYNA was performed, investigating a total of 60 cases. The simulation results provided valuable insights and findings regarding the behavior of RC columns under different air blast and UNDEX loading scenarios. This study is particularly pioneering in its investigation of RC columns subjected to partially submerged explosions. Additionally, the response of RC columns for both contact and non-contact air and UNDEX explosions were investigated.

CHAPTER ONE

1.1 Motivation

During an explosion, there is a rapid occurrence of chemical reactions that transform the original substance into a gaseous state and release a substantial amount of heat. The resulting gases reach temperatures as high as 3,000°C and exert pressures at levels around 50,000 atmospheres (Cole, 1948) [1]. The energy release can manifest in various environments, including the atmosphere, Earth's surface, underground, or underwater. Among these scenarios, underwater explosions (UNDEX). UNDEX phenomena are primarily influenced by multiple fundamental physical laws and properties, with particular emphasis on the characteristics of the surrounding water. Understanding and analyzing the complexities of underwater explosions requires a comprehensive examination of these factors (Zare & Janghorban, 2013) [2].

The motivation for this thesis stems from the increasing occurrence of explosive incidents, both accidental and deliberate, that pose a significant threat to public safety and critical infrastructure systems worldwide. The shift towards deliberate explosive assaults by terrorist organizations targeting densely populated areas and critical structures necessitates a proactive understanding of how different structures respond to explosive forces. By comprehensively analyzing the behavior of structures under air blast and UNDEX this research aims to enhance structural resilience, design robust protective measures, and implement effective risk management protocols.

The preservation of human life and public safety is a paramount concern driving this research. The devastating consequences of explosive events, as evidenced by the high death toll and numerous injuries documented in recent reports, highlight the urgent need to investigate the response of structures to explosions. Understanding these effects enables engineers to develop strategies to mitigate the impact of such events, thereby safeguarding lives and minimizing injuries. The protection of critical infrastructure systems is another significant motivation. Infrastructure systems, such as bridges, power plants, and communication networks, are prime targets for deliberate explosive attacks. By studying how these structures respond to explosive forces, engineers can develop innovative design solutions and reinforce existing infrastructure, reducing vulnerability, and ensuring their continued functionality in the face of hostile acts. Furthermore, the research aims to contribute to the advancement of protective measures and technologies.

In conclusion, the motivation for this thesis lies in the need to understand and analyze the response of structures to explosive forces, driven by the evolving nature of explosive incidents, the preservation of human life and public safety, the protection of critical infrastructure, and the advancement of protective measures and technologies. Through this research, valuable insights can be gained to enhance structural resilience, develop effective mitigation strategies, and contribute to the overall safety and security of communities.

1.2 Significance/Contribution of the Study

The significance and contribution of this study is to present a pioneering work in the investigation of RC columns subjected to partially submerged explosions and fill the knowledge gap that exists in published literature. This study aims to address critical gaps in the current understanding of the response of structures to explosive loads, particularly in the context of bridge engineering and emerging maritime terrorism. The research focuses on investigating the damage endured by reinforced concrete (RC) columns, specifically RC bridge columns, when subjected to blast loading. Understanding the behavior of bridge piers, which provide vital vertical support to bridge structures under explosive forces is crucial in informing decisions for protective design of vulnerable structures.

The study also seeks to tackle the increasing occurrence of explosive incidents, both accidental and deliberate, that pose significant threats to public safety and critical infrastructure systems worldwide. With deliberate explosive assaults by terrorist organizations targeting densely populated areas and critical structures on the rise, it is essential to proactively understand how different structures respond to explosive forces. Through comprehensive analysis of structures under air blast and UNDEX, this research aims to advance the understanding of RC columns under both air and UNDEX loads.

Furthermore, the study recognizes the heightened risk of maritime terrorism, particularly incidents involving waterborne boat bombs, which pose a significant threat to coastal regions and critical infrastructure like bridges. Understanding the effects of near-surface and partially submerged explosions on reinforced concrete bridge columns and components is crucial. However, there is a research gap in this area, as there are not many available studies on this research area. of near-surface and partially submerged air and UNDEX loading. Specifically, no available previous works on the behavior of RC columns subjected to partially submerged air and UNDEX loading was found on open source literature. On top of other topics in UNDEX and air blasts, by addressing this gap, this study aims to contribute pioneering research on the response of RC columns under partially submerged explosive loading scenarios, filling an important knowledge void.

1.3 Thesis Organization

The thesis is structured into six chapters to systematically address the research objectives. Chapter one introduces the study, presenting the motivation, significance, and contribution of the research. Chapter two offers critical reviews of existing research findings, focusing on the behavior and analysis of RC columns when subjected to both air blasts and UNDEX. This chapter serves as a foundation for understanding the current state of knowledge in the field. In chapter three, the development and validation of the air blast numerical model are discussed. This section outlines the methodology used to create the model and presents the validation process to ensure its accuracy and reliability. Chapter four focuses on the development and validation of the UNDEX numerical model. It details the steps taken to construct the model and verifies its effectiveness by comparing the simulation results with experimental data.

Chapter five encompasses a parametric study conducted using the validated UNDEX model. This study investigates the effects of blast loads from TNT explosive charges on RC columns, considering parameters such as stand-off distance, charge weight, and water depth. A comprehensive analysis of 60 cases is performed, providing valuable insights into the behavior of RC columns under different UNDEX loading scenarios. Finally, chapter six concludes the thesis by summarizing the key findings, presenting recommendations, discussing the limitations of the study, and suggesting areas for future research.

General objective: The aim of this study is to examine the behavior and dynamic responses of RC columns when subjected to air blast and UNDEX loadings.

Specific objectives:

- Develop, calibrate, verify, and validate a numerical model to simulate the air blast responses of RC columns.
- Develop, calibrate, verify, and validate a numerical model to simulate the UNDEX responses of RC columns.
- Conduct a parametric study to analyze the effects of explosive charges, including stand-off distance, charge weight, and water depth, on RC columns.
- Investigate the behavior of RC columns under partially submerged explosions.

CHAPTER TWO

2.1 Introduction

This section encompasses critical reviews of research findings that explore the behavior and analysis of RC columns when subjected to air blasts and UNDEX. This comprehensive review considers both experimental testing and numerical studies employed to investigate the aforementioned phenomena.

2.2 Literature Review

2.2 Behavior of RC Columns Subjected to Air Blast

2.2.1 Experimental Findings

Luki´ & Draganic (2021) [3] stated that conducting experiments on real-scale bridge columns is challenging and expensive due to the complexity of the experimental setup. Conversely, experiments on building columns are predominantly carried out in full scale as their maximum height ranges from 2.5 to 3 m. The authors further highlighted that these types of experiments necessitate specialized testing grounds, typically military field ranges, and trained personnel to handle explosives. However, these testing grounds also have limitations concerning the maximum quantity of explosives that can be detonated at once, which consequently restricts the size of the specimens used. In lieu of full-scale tests scaled tests are shown to yield dependable results and provide essential knowledge for analyzing the impact of blast loads on structures (Fouché et al., 2016) [4].

Bruneau et al. (2006) [5] developed a multi-hazard pier concept to enhance protection against failure caused by explosions and earthquakes. The study used concrete-filled circular steel columns (CFCSC) with three different diameters (10.16 cm, 12.7 cm, and 15.24 cm) and a minimum steel thickness of 3.2 mm, scaled at 1:4 of the prototype bridge columns. The experimental results indicated that increasing the standoff distance and column diameter even slightly can significantly reduce column deformation. The CFCS columns demonstrated ductile behavior and high resistance to explosion effects.

Fujikura et al 2008 [6] studied the effect of explosives under the bridge in a car located near the column. They assumed charge weights similar to blast weights predicted in FEMA (2003) [7]guidelines. Charges were set at heights of 0.25 m and 0.75 m, corresponding to the actual height of a car bomb and half the column height, respectively. The study concluded that steel jacketing alone is insufficient in providing adequate resistance to the shear forces affecting the column's base. Instead, they proposed the use of fully concrete-filled steel tubes (CFST) continuously embedded into the footing. CFST columns exhibited ductile behavior, adequate resistance to lateral forces from explosions and earthquakes, and did not produce flying.

Fujikura et al 2008 presented a connection concept between the foundation beam and the CFST column that provided full moment capacity without concrete cracking. Plastic deformation became visible at a rotation of 3.8° at the bottom of the column, with the first concrete cracks occurring at a rotation of 8.3°. The fracture of the steel tube was observed at 17°. At the height of the explosive charge, pits and notches appeared on the steel tube, while concrete cracks occurred on the tension side at the bottom and top of the column due to the rigid boundary conditions.

Furthermore, Fujikura et al. [6] conducted experiments on a similar blast scenario as in the previous study but with four columns in the test specimen instead of three. The RC column exhibited shear failure at the base with concrete cracking along the column. RC SJ (steel jacketed) columns experienced shear failure as well, while CFST columns demonstrated flexural failure and buckling. Fujikura and Bruneau (2010) [8] investigated seismically ductile RC columns and non-ductile RC columns retrofitted with steel jackets. The explosive charge was set at a height of 0.25 m, resulting in the maximum deflection of the column. While all columns in the Fujikura and Bruneau (2010) study failed in direct shear at the base, the RC columns with steel jackets did not suffer structural damage but spalling of concrete occurred at the bottom. In comparison, the CFST columns exhibited ductile behavior, unlike the other columns.

Burrell et al. [9] tested two half-scale reinforced concrete columns and six Steel Fiber-Reinforced Concrete (SFRC) columns using a shock tube. The SFRC columns had steel fiber content ranging from 0 to 1.5% by volume of concrete, and both seismic and non-seismic detailing were considered.

During the experiments, an axial load equivalent to 30% of the columns' load capacity was applied utilizing a hydraulic jack. The results of the study indicated that columns designed with seismic detailing, specifically with a 38 mm distance between transverse reinforcement, exhibited smaller maximum displacements and demonstrated greater resistance against blast loads. This suggests that the seismic design approach contributes to enhanced structural performance under blast loading conditions. Furthermore, SFRC columns with non-seismic detailing, featuring a 75 mm distance between transverse reinforcement, displayed reduced maximum displacements and no secondary blast fragments. This highlights the potential benefits of incorporating steel fiber reinforcement in columns designed without seismic considerations, as it contributes to improved blast resistance and reduced fragmentation.

In summary, Burrell et al.'s [9] research findings indicate that columns designed with seismic detailing and closer spacing between transverse reinforcement exhibit superior performance in terms of displacement limitation and blast load resistance. Additionally, SFRC columns with non-seismic detailing and larger spacing between transverse reinforcement can also effectively mitigate displacements and minimize the generation of secondary blast fragments. These insights are valuable for understanding the behavior of reinforced concrete and SFRC columns subjected to blast loading scenarios, and they provide important considerations for structural design and mitigation strategies.

Wang et al. (2020) [10] conducted a comprehensive study aimed at investigating the impact of contact explosions involving various quantities of TNT (1 kg, 2 kg, and 3 kg) on Ultra-High Performance Cementitious Composite Filled Steel Tube (UHPCC-FST) bridge columns. To simulate real-world conditions, the columns were scaled down to a 1:4 ratio and subjected to horizontal testing. The experimental setup involved fixing the bottom of the column while allowing the top to be pinned. In order to replicate the positioning of explosives within a vehicle at a height of 1 m, a cylindrical explosive was placed at a distance of 25 cm from the lower support. This positioning ensured that the blast effects were accurately represented in the tests.

When 1 kg or 2 kg of TNT was detonated, the columns exhibited the formation of a crater, indicating localized damage. However, with a 3 kg explosion, the tube of the column fractured, and the core material was severely crushed, signifying more extensive structural failure. Furthermore, the study conducted axial compression tests on the columns to assess their resistance under vertical loading. The results demonstrated that all columns, regardless of the quantity of explosives used, experienced diagonal shear failure. This failure mode highlights the vulnerability of the UHPCC-FST bridge columns to the combination of explosive loading and axial compression.

In summary, Wang et al. (2020) [10] provides valuable insights into the behavior of UHPCC-FST bridge columns subjected to contact explosions. It demonstrates the varying levels of damage and failure modes observed at different explosive quantities, shedding light on the structural response and failure mechanisms under blast loading conditions.

Yuan et al. (2017) [11], conducted tests on two RC bridge columns subjected to scaled testing using a contact explosion involving 1 kg of TNT positioned 33 cm above the ground. The columns were securely fixed in the ground and constrained at the top using a steel hoop attached to a reaction wall, which was positioned 1.4 meters away to minimize the reflection of blast waves. These tests were chosen to calibrate the numerical model for the air blast in this thesis in chapter 3. To further minimize wave reflection, a large opening was incorporated into the reaction wall. The dynamic response of the columns was predominantly influenced by the propagation of stress waves within the columns rather than shock waves in the surrounding air. The TNT charge comprised five blocks of 0.2 kg

TNT placed on the surface of each column. No axial load was applied to the columns during the test since it was anticipated to have minimal impact on their response to contact detonations.

Yuan et al.'s [11] experimental results revealed significant compressive failure on the front surface of both square and circular columns, with the side surface experiencing severe damage and the rear surface exhibiting relatively less damage. They explained that the contact detonation initiated three-dimensional wave propagation within the columns. Once the concrete on the front surface was destroyed, the remaining blast energy propagated as compressive waves. When these waves interacted with the side surface, they transformed into tensile waves, leading to severe tensile concrete failure. The extensive concrete failure on the front and side surfaces absorbed a substantial amount of the blast energy, while the rear surface, which experienced a longer travel distance for the blast wave, suffered lower levels of tensile failure.

They also revealed that the square column sustained more severe damage compared to the circular column, particularly in terms of core concrete loss and stirrup fracture. They attributed the level of damage due to the low net blast loading on curved surfaces when compared to the square column. Additionally, the shape of the stirrups played a role, with the circular stirrups providing better confinement. Stirrup fracture occurred in the square column but not in the circular column. The larger effective front reflective surface of the square column, along with its shape, led to a more substantial impact on the front face, causing concrete expansion perpendicular to the loading direction and resulting in stirrup fracture. Furthermore, the square column exhibited extensive concrete damage in the height direction, primarily due to stress concentration at its corners, which led to severe stress concentrations and concrete fracture caused by multiple reflections.

Regarding the rear surfaces of both columns, no noticeable concrete spalling was observed. However, extensive cracks were present. These cracks were a result of tensile fracture when the blast wave reflected and transformed into a tensile wave upon reaching the column's free surface. Nevertheless, the tensile stress on the rear surface was lower than the tensile strength of the concrete, preventing spalling. The cracks were generated during the subsequent flexural response of the columns.

To summarize, the study by Yuan et al. (2017) [11] provided valuable insights into the behavior of RC bridge columns when subjected to contact explosions. It demonstrated significant compressive and tensile concrete failures on the front, side, and rear surfaces of the columns. The square column experienced more severe damage due to differences in blast load application and stress concentration at the corners. These findings contribute to the understanding of blast-resistant design considerations for RC bridge columns and can inform the development of strategies to enhance their performance in contact explosion scenarios.

2.2.2 Numerical Findings

With the rise in the frequency of terrorist attacks, engineers are faced with new and complex challenges that require assessments beyond limited physical testing. Numerical simulations play a pivotal role in gaining a deeper understanding of the impact of blasts on RC columns as well as their individual components and they are also vital for designing future experimental tests (Luki´ et. al., 2021) [3].

Wu et al. (2011) [12] employed numerical simulations using LS-DYNA to investigate the behavior of RC and composite columns subjected to contact-placed TNT charges varying from 2.5 kg to 25 kg. Notably, the positioning of the explosive charge played a crucial role in determining the residual bearing capacity of the columns. Specifically, when the explosive charge was positioned at a height of 1.5 m from the bottom of the column, a higher residual bearing capacity was observed compared to when the charge was placed at the bottom. This finding highlights the importance of the explosive placement location in assessing the structural response of columns to blast loading.

Hao et al. (2010) [13] conducted an analysis on three reinforced concrete columns that shared the same dimensions, material strengths, and reinforcement ratios. The columns were subjected to blast loads at different scaled distances, aimed at assessing the failure probability using the computer code CARLER, and validated through Monte Carlo simulations. They defined four damage levels based on the ratio of the residual axial load carrying capacity of the damaged column to the axial load of the undamaged column. They found that random variations in the blast loading played a significantly greater role in determining the probability of failure.

These findings highlight the importance of considering the uncertainties associated with blast loading in assessing the structural response of reinforced concrete columns. While the material properties of the columns may have limited impact on the failure probability, variations in blast loading can significantly influence the likelihood of failure. Therefore, it is crucial for engineers to account for these random changes in blast loading when evaluating the structural performance and failure probability of reinforced concrete columns under blast loads.

Crawford (2013) [10] developed numerical simulations were carried out in LS-DYNA to investigate the behavior of RC columns and columns retrofitted with fiber-reinforced plastic (FRP) under blast loads. The objective was to assess the effectiveness of FRP in enhancing the resistance of RC columns to blast loads. Four different concrete models, namely KC, Winfrith, Continuous Smooth Cap, and RHT model, were utilized for the analysis. These models allow for the characterization of the concrete's response under dynamic loading conditions. The results of the simulations demonstrated that the choice of concrete material model played a significant role in accurately capturing the behavior of the columns subjected to blast loads. Among the four models examined, the KC model yielded the most favorable outcomes in terms of accurately representing the response of the RC columns and FRP retrofitted columns.

Yi et al. (2014) [14] introduced a method called HBL (Hybrid Blast Load) and conducted numerical simulations using LS-DYNA to investigate a typical highway bridge with column bent piers. The HBL method is a coupled Load_Blast_Enhanced (LBE) and ALE approach that considers the reflection and diffraction of the blast wave. Through extensive simulations, various damage modes of the bridge were observed, and a relationship between the ratio of ductility and strength reduction factor was established based on the obtained results.

Similarly, Liu et al. (2015) [15] employed the LBE approach proposed by Yi et al. (2014) [14] to apply blast loads and conducted numerical simulations using LS-DYNA for the column bent pier of the same bridge. The findings revealed that the simplified approach used in previous studies might lead to unconservative predictions. To address this issue, a compensatory measure involving amplifying the explosive charge in the simulations was proposed. Furthermore, the study demonstrated that reinforcing the column bent pier with strengthened transverse reinforcement can significantly enhance its resistance to blast loads.

Yi et al. (2014) [14] and Liu et al. (2015) [15] contributes to the field by introducing the HBL method, which accounts for the complex phenomena of blast wave reflection and diffraction in bridge structures. Through their numerical simulations, they observed various damage modes in bridge components and established a relationship between ductility and strength reduction. Liu et al. (2015) further emphasizes the limitations of simplified methods and proposes a compensatory measure to improve the accuracy of blast load predictions. Additionally, the effectiveness of strengthened transverse reinforcement in enhancing the blast resistance of bridge piers was demonstrated. Incorporating these findings into the design and analysis of bridge structures can lead to improved blast resilience and overall safety.

Magali et al. (2013) [16] investigated the influence of various parameters on the damage of reinforced concrete columns through a parametric numerical analysis using Abaqus. The six parameters considered in the study were the section ratio, compressive strength of concrete, column height, column thickness, charge radius, and the ratio between the standoff distance and the charge radius. The findings revealed that the column thickness, charge radius, and the standoff distance-to-charge radius ratio had a significant impact on the response of the columns to blast loads.

They derived an empirical formula that enables the prediction of the damage index of the column based on the aforementioned parameters. Subsequent comparison between the results obtained from the formula and numerical simulations indicated deviations within an acceptable range of up to a maximum of 15%. This suggests that the empirical formula provides a reliable means of estimating the damage index of reinforced concrete columns subjected to blast loads. Overall, Magali et al. (2013) [16] provided valuable insights into the understanding of the factors influencing column damage. The developed empirical formula serves as a practical tool for preliminary assessments, enabling engineers to estimate the potential damage to reinforced concrete columns based on key parameters.

Yuan et al. (2017) [11] conducted a comprehensive numerical study using LS-DYNA to analyze the response of circular and square columns of a bridge when subjected to a contact explosion of 1 kg of TNT. The numerical simulations employed the ALE capability of LS-DYNA, which facilitated the modeling of the ambient atmosphere and explosive charge using a Eulerian mesh, while the concrete and reinforcements were represented by a Lagrangian mesh. To optimize computational efficiency, they implemented a denser mesh size of 8 mm in the region of the contact explosion at a height of 1 m, while a coarser mesh size of 20 mm was used for the remainder of the column. The erosion criterion of a principal strain of 0.5 was employed during the simulations. The numerical simulations effectively captured the damage patterns on the front sides of the column. However, differences in damage profiles were observed on the back side of the columns. Importantly, the study revealed that the cross-sectional shape of the columns played a significant role in determining the damage characteristics. The circular column experienced lower blast loads compared to the square column due to its curved surface. Moreover, the square column exhibited severe damage at the four corners due to stress concentration, which was not observed in the circular column.

In summary, the numerical study conducted by Yuan et al. (2017) [11] provided valuable insights into the behavior of circular and square columns when subjected to contact explosions. The findings highlighted the influence of cross-sectional shape on damage profiles, with the circular column exhibiting better performance compared to the square column. These results have significant implications for the design and assessment of blast-resistant columns in bridge structures.

Yang et al. (2019) [17] conducted a numerical investigation to examine the impact of cross-section shape on the anti-knock performance of RC columns exposed to air and underwater blast loads. They utilized ANSYS and employed the fully Coupled Lagrangian-Eulerian (CLE) numerical method. To validate the reliability of their model, they compared their results with those obtained from a field blast test previously conducted by Yuan et al. (2017) [11]. They investigated the damage characteristics and dynamic response of RC columns with different cross-section shapes when subjected to contact and close-in air explosions. Additionally, they examined the anti-knock performance of RC columns with various cross-section shapes under contact and close-in underwater explosions. They also compared the nonlinear dynamic response behavior and damage mechanisms of the RC columns exposed to contact and close-in explosions. Furthermore, they explored the effects of reinforcement ratio and ultra high-performance concrete on the blast resistance of underwater RC columns.

Their findings emphasized the significant influence of cross-section shape on the anti-knock performance of columns exposed to both air and underwater explosions. Specifically, employing a circular cross-section was found to effectively enhance the blast resistance of the column. In summary, Yang et al. (2019) [17] provided valuable insights into the relationship between cross-section shape and the anti-knock performance of RC columns subjected to air and underwater blast loads. Their findings highlighted the advantages of utilizing a circular cross-section in improving the blast resistance of the columns.

2.3 Underwater Explosion (UNDEX) Effects on Structures

The study of UNDEX and its impact on platforms originated during World War I when the use of explosive warheads in sea mines, torpedoes, and inaccurate shells detonating in water posed significant threats to ships at that time. After WWI and WWII, there was a significant increase in research efforts to enhance the effectiveness of weapons and improve ship survivability (Keil, 1961) [18]. A notable compilation of research work emerged after World War II, led by British and American research agencies, resulting in a three-volume compendium (USNRBD, 1950) [19]. This compendium delved into the fundamental aspects of the underwater explosion phenomenon, including the shock wave, the gas bubble, and the associated damage processes.

Cole (1948) [1] provided a comprehensive overview of the UNDEX event, incorporating the significant contributions from the aforementioned compendium. Cole's work integrated mathematical and physical principles, establishing itself as the definitive reference in the field. It is important to note that these seminal works were conducted over 60 years ago, utilizing measurement and analysis methods that predated the advent of computers and even general electronics in the field. During that era, mechanical measurements and ideal mathematical or empirical solutions were the primary sources of experimental data. Despite the current availability of sophisticated computers and measurement systems, much of this earlier research remains relevant today. This is because even with the advancements in technology, the extreme environment of the UNDEX event continues to pose challenges, limiting the applicability of more advanced methods (De Candia, 2018) [20] .

Fox (1992) conducted a study on UNDEX involving numerical analysis and experimental comparisons. The numerical analysis focused on near-field explosions, while the experimental comparison examined a far-field explosion on a cylindrical shell. The numerical results generally aligned with the experimental findings, accurately predicting compression, tension, and similar shapes. However, magnitude differences between the numerical and experimental data increased with distance from the explosion point. Areas closer to the explosion point and regions with lower strain values showed better agreement. The study aimed to investigate cylindrical shell responses to near-field and far-field side-on attacks using numerical analysis and sensitivity analyses. Proper mesh design in areas with large strain gradients was crucial to minimize differences, and high strain areas were sensitive to various factors. Fox (1992) [21] derived two main conclusions. First, the USA/DYNA3d connection successfully replicated the response of simple analytical models. Second, numerical modeling could predict the response of a simple cylinder to an underwater explosion. Near-field numerical predictions aligned with expected outcomes.

Liu et al. (2003) [22] conducted a study focusing on the application of the Smoothed Particle Hydrodynamics (SPH) method to simulate UNDEX problems. Their research probed into the numerical procedures involved in the SPH method, highlighting specific aspects such as the utilization of artificial viscosity, evolution of smoothing length, treatment of solid boundaries, consideration of material interfaces, and the implementation of the Leapfrog time integration scheme. The authors demonstrated the effectiveness of the SPH method through the analysis of three distinct case studies. Firstly, they examined the detonation of a one-dimensional TNT slab, providing detailed insights into the simulation results. Secondly, they explored the scenario of an underwater explosion occurring in free space, investigating various aspects and phenomena associated with the event. Lastly, they investigated an underwater explosion taking place within a confined chamber, providing valuable observations and analysis of the simulated outcomes.

Seunggyu et al. (2021) [23] conducted a study on near-field UNDEX using a combination of experiments and numerical simulations. The experiments involved using a ship-like model in a water tank and detonating one kilogram of TNT, a commonly used military explosive. The numerical simulations were performed using the LS-DYNA commercial software, replicating the experimental conditions. Measurements were taken at various locations to capture underwater pressures, accelerations, velocities, and strains caused by shock waves. Additionally, the study investigated the bubble pulsation period and whipping deformations of the ship-like model. The experimental results were presented and compared with results obtained from widely used empirical equations and numerical simulations.

Sanders et al. (2021) [24] noted that the effects of air blasts on RC columns are well-documented, while the effects of UNDEX are less studied. Yang et al. (2019) [17] investigated the response of RC columns to both air blasts and UNDEX. They employed a fully coupled three-dimensional Lagrangian and Eulerian numerical method (CLE) to simulate the effects of UNDEX on RC columns with different cross-sections. This numerical model was validated through physical experiments conducted on an RC column with a square cross-section by Yuan et al. (2017) [11] . The high-pressure shock wave and water-structure interaction effects result in substantial loads on submerged structures during UNDEX. This can cause structural deformation, rupture, and fragmentation. Additionally, the collapse of gas bubbles formed during the explosion can further impact the structure.

Yang et al. (2019) [17] validated their numerical CLE model by comparing damage profiles and dynamic responses with experimental methods. Using the verified model, they analyzed RC columns with different cross-section shapes. Circular cross-sections exhibited better anti-knock performance due to shock wave diffraction and stress wave compounding compared to square columns. They observed significant damage in both square and circular columns, with severe destruction of concrete around the TNT charge due to shock waves and detonation products. The damage and fracture area on the front surface of circular columns were comparatively smaller than those in square columns. The deflection profile of circular columns was also smaller than that of square columns, despite identical blasting scenarios. The maximum deformation of circular columns decreased by 37% compared to square columns. Furthermore, Yang et al. [17] also conducted a parametric study to assess anti-knock measures and their effectiveness. They examined varying concrete properties, reinforcement spacings, and reinforcement thickness. The use of ultra-performance concrete was found to be the most effective measure for damage control, followed by decreasing reinforcement spacing and introducing more reinforcements to the column.

Zhuang et al. (2020) [25] conducted physical experiments to study the dynamic response and damage model of RC columns subjected to UNDEX. They used a scaled-down RC circular column and a steel column for experimentation, focusing on load distribution and collecting data on pressure, acceleration, strain, and displacement. The explosive charges used varied in mass between 0.05 and 0.8 kg. The experimental data revealed that the round surface of the column refracts the shock wave loading, resulting in lower diffracted pressure compared to the shock pressure. This observation is influenced by factors such as explosive quantity, stand-off distance, and detonation depth. The proximity of the air-water surface hampers the bubble pulse, causing its energy to disperse upward into the air rather than into the column. Smaller explosive quantities generate smaller bubble pulses, while larger explosive quantities vent to the surface, preventing a fully realized bubble pulse.

Zhuang et al. (2020) [25] derived several relationships for predicting shock wave load based on the experimental data. These include neglecting free surface effects based on explosive quantity and detonation depth, an inverse relation between the diffraction coefficient and proportional stand-off distance using the least square method, and the calculation of net peak pressure through the reflected and diffracted shock wave peak pressures. Parametric studies were conducted to analyze the effects of explosive quantity, stand-off distance, detonation depth, and proportional stand-off distance on the damage profiles of the columns. Increasing stand-off distance led to a significant decrease in shock wave load. Larger detonation depths resulted in higher bubble pulse effects, with a critical value of the non-dimensional detonation depth (proportional stand-off distance) of 1.71, below which no bubble pulsation effects were observed.

Zhuang et al. (2020) [25] drew several conclusions. First, the shock wave pressure acts on the surface of the circular column, resulting in reflection and diffraction, with the peak pressure of the reflection shock wave higher than that of the diffraction shock wave. Secondly, bubble pulsation pressure was observed only for small explosive quantities and relatively large detonation depths, where the free surface had less influence on the explosion. Third, the shock wave load decreases exponentially with increasing stand-off distance. Fourth, the detonation depth has a significant effect on the time history characteristic of pressures, particularly on bubble pulsating pressure. Fifthly, for small explosive quantities, two pressure peaks were observed in the time curve, corresponding to the shock wave and the bubble pulsation. For large explosive quantities, the explosion was influenced more by the water surface boundary, and only the shock wave peak was observed. Finally, the damage modes of circular RC columns include bending failure, bending-shear failure, and punching failure, with the occurrence depending on factors such as explosive quantity, stand-off distance, and the proximity of the water surface. The experimental findings from Zhuang et al. (2020) [25] discussed earlier were employed to calibrate the numerical model for UNDEX in chapter 4.

2.4 Material Models for Concrete

To solve a problem related to the behavior of materials under dynamic conditions, it is crucial to utilize the fundamental principles of mass, momentum, and energy conservation, in addition to appropriate boundary and initial conditions. A complete solution also necessitates a material model that establishes a correlation between stress, deformation, and energy. In hydrocodes like AUTODYN and LS-DYNA, this is generally accomplished by dividing the total stress tensor into two components: a hydrostatic pressure that causes volume changes, and a deviatoric stress that causes changes in shape. The hydrostatic pressure remains uniform, with equivalent normal stresses in all directions and is calculated using the material's density (specific volume) and energy (or temperature) using an Equation of State (EOS).

Meanwhile, the deviatoric stress tensor describes the material's ability to resist shear deformation using a strength model. Therefore, the EOS and strength model provide a means to measure the changes in volume and shape that a loaded material undergoes, respectively (Hansson & Skoglund, 2002) [26]. Elasticity-driven constitutive relationships represent a category of mathematical models employed to describe the response of concrete materials when subjected to external forces. These relationships are based on the fundamental principles of elasticity, which state that a material will deform in proportion to the magnitude of the applied stress, up to a certain limit called the elastic limit.

Another elasticity-based constitutive relationship used for concrete is the nonlinear elastic model. This model considers the nonlinear relationship between stress and strain that occurs at higher loads, as well as the fact that the material may not completely return to its original shape and size after the load is removed. Although they possess certain limitations, elasticity-driven constitutive relationships are widely employed for concrete in both pre and post failure stages, as extensively noted by Chen in 2007 [27]. In 1993, Johnson and Holmquist [28] introduced a brittle damage model for concrete, as shown in Equation (2.1) Chen in 2007 [27]. The Johnson & Holmquist (JH) [28] concrete model is a nonlinear constitutive model utilized to characterize the behavior of concrete under high strain rates and large strains, such as those encountered during impact or blast loading. This model has gained widespread use in the fields of structural engineering and impact mechanics.

The JH material model assumes that concrete is a composite material comprising of aggregates, cement paste, and air voids. It divides the material into two constituents: a compressible matrix and an incompressible pore fluid. The matrix component is assumed to follow a plastic flow rule, while the pore fluid component is presumed to be incompressible and provides pressure support to the matrix.

Equation 2. 1

$$\sigma^* = [A(1-D) + BP^{*N}] \times (1 + \mathrm{C}\ln\ \varepsilon^*) \ \text{ for } \sigma^* \leq \mathrm{SMAX}$$

Equation 2. 2

$$\sigma^* = \mathrm{SMAX} \text{ for } \sigma^* > \mathrm{SMAX}$$

Equation 2. 3

$$\sigma^* = \frac{\sqrt{3J_2}}{\mathrm{f_c}\,'}$$

Where; P^* = P/$\mathrm{f_c}\,'$ is the normalized pressure, where P represents the actual pressure, and D indicates the damage ($0 \leq \mathrm{D} \leq 1.0$), where ε^* denotes the normalized equivalent plastic strain rate. The equivalent plastic strain is normalized with respect to a unit strain rate. $*$ denotes normalized quantities The equations use A, B, N, and C as constants and SMAX stands for the greatest strength that concrete may acquire. The symbol J_2 represents the second deviatoric stress invariant, while $f_c{}'$ denotes the uniaxial compressive strength of concrete.

The Riedel-Hiermaier-Thoma (RHT) [29] concrete model is another constitutive model used to describe the behavior of concrete under high strain rates and large strains, such as those experienced in impact or blast loading. In 1999, the RHT model was introduced by a team of researchers led by Wolfgang Riedel, Martin Hiermaier, and Matthias Thoma [29]. This model illustrates the strength characteristics using three stress limit surfaces: the initial elastic yield surface, the failure surface, and the residual friction surface. Within the RHT model, concrete demonstrates a fracture surface that operates independently, while its hydrostatic strength relies on the rate, as expressed in Equations (2.4) & (2.5) by Riedel et al. in 1999 [29]. The failure surface of the RHT model is specified based on the work conducted by Riedel et al. in 1999 [29].

Equation 2. 4

$$Y_{fail}\left(p^*, \theta, \dot{\varepsilon}\right) = Y_c(p^*) r_3(\theta) F_{rate}\left(\dot{\varepsilon}\right)$$

Equation 2. 5

$$Y_c(p^*) = f_c' \left[A\left(p^* - p^*_{spall} F_{rate}\left(\dot{\varepsilon}\right)\right)^N\right]$$

Where f_c' is the uniaxial compressive of concrete, and the constants *A* and *N* are the model parameters. The rate factor $F_{rate}\left(\dot{\varepsilon}\right)$ denotes the dynamic increase factor (DIF) of the tensile strength as a function of the strain rate (Riedel et al. 1999).

Figure 3.1 visually illustrates the lower cap pressure, P_u, which signifies the pressure at which the uniaxial compression path intersects the elastic limit surface.

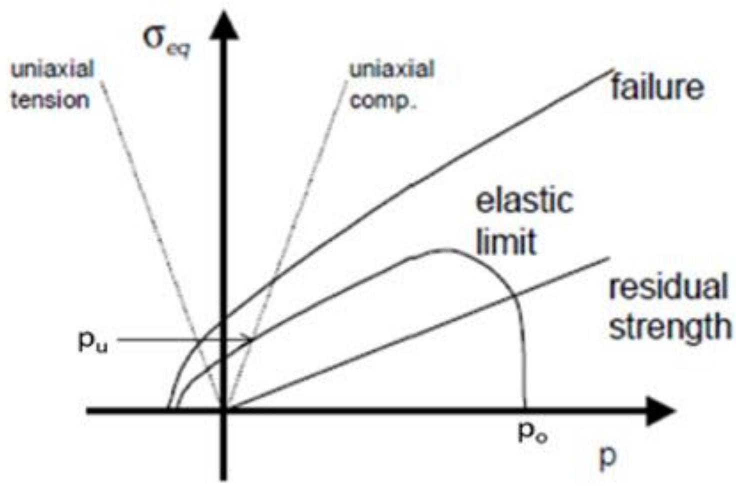

Figure 2. 1 Concept of three limit surface (Riedel et. al. 1999).

2.5 Material Models For Reinforcing Steel

Since the early 1940s, numerous scholars have contributed to the development of constitutive relationships for reinforcing steel. Ramberg and Osgood (1943) [30], Menegotto and Pinto (1973) [31], and Chang and Mander (1994) [32] have significantly contributed to this field. The Ramberg and Osgood (1943) [30] model particularly stands out as a non-linear elastic model tailored for monotonic loading, distinguished by its limited memory of stress-strain behavior. It employs a solitary nonlinear equation to describe the curved response observed in reinforcing steel under monotonic loading conditions. This model captures the nonlinearity of the material's behavior, providing a representation that aligns with the actual response observed in practice. Although the

Ramberg and Osgood model has provided reasonably accurate predictions for the behavior of one-dimensional steel, its reliance on stress as a primary parameter poses challenges when integrating it into conventional strain-driven finite element analysis programs. Moreover, this model fails to account for the presence of the yield plateau, which is a critical aspect that can greatly influence the dynamics of a system.

The Johnson-Cook model, formulated by Gordon R. Johnson and William H. Cook in 1985 [33], is a constitutive material model specifically designed to characterize the response of metals under extreme conditions of elevated temperatures and high strain rates. This model has gained widespread usage in engineering and computational simulations, particularly in the domain of impact and crash analysis. This model incorporates the effects of strain rate and temperature on the flow stress and plastic deformation of a material. It is based on the concept of the flow stress as a function of effective plastic strain, strain rate, and temperature. The model is often employed for materials subjected to dynamic loading conditions, such as in explosive detonations, ballistic impacts, or metal forming processes. To capture the strength properties, the Johnson-Cook (JC) model (Equation 2.6) utilizes the Von Mises tensile stress.

Equation 2. 6

$$\sigma = (C_1 + C_2\varepsilon^{\mathrm{n}})(1 + C_3\mathrm{In}\ \varepsilon^*)(1 - \mathrm{T}^{*\mathrm{m}})$$

Where ε is the equivalent plastic strain, ε* is a dimensionless plastic strain, and T* is the homologous temperature. C_1, C_2, C_3, n, and m are steel material constants. Moreover, Johnson and Cook also developed a fracture model (Equation 2.7) that incorporates the impact of strain rate, temperature, and pressure on the material (Johnson and Cook, 1985) [33].

Equation 2. 7

$$\varepsilon^{\mathrm{f}} = \left[D_1 + \mathrm{D}_2^{\mathrm{D}_2 \sigma^{\mathrm{m}}}\right] [1 + \mathrm{D}_4 \ln \varepsilon^*][1 + \mathrm{D}_5 \mathrm{T}^*] \text{ for } \sigma^* \leq 1.5$$

σ* is a dimensionless pressure-stress ratio, σm is average of the three normal stresses, σ is Von Misses equivalent stress, and D_1, D_2, D_3, D_4, D_5 are material constants. In the revised versions of the Johnson-Cook [33] models, the yield strength demonstrates a logarithmic variation in relation to the dimensionless strain. The precise expression for the strength model within these modified models is outlined in Equation (2.8).

Equation 2. 8

$$\sigma = [C_1 + C_2 \varepsilon^{\mathrm{n}}] \times \left[1 + C_3 \ln\ \varepsilon^* + C_4 \left(\frac{1}{C_5 - \ln\ \varepsilon^*} - \frac{1}{C_5}\right)\right] (1 - T^{*\mathrm{m}})$$

Where C_4 and C_5 are empirical coefficients. Strain rate sensitivity of the material is enhanced by the introduction of the expression $\frac{1}{C_5 - \ln\ \varepsilon^*}$. C_5 is the natural logarithm of the critical strain rate level.

2.6 ANSYS LS-DYNA

LS-DYNA, a software initially developed by the former Livermore Software Technology Corporation (LSTC) [34] and later acquired by ANSYS in 2019, is a versatile finite element code used for analyzing the response of structures to large deformation and dynamic forces. It can handle structures that interact with fluids as well. LS-DYNA predominantly utilizes explicit time integration as its core methodology. The software has its roots in DYNA3D, a publicly available program created in the mid-1970s at the Lawrence Livermore National Laboratory [34]. The initial version of DYNA3D was made accessible in 1976, and it primarily focused on stress analysis of structures subjected to various impact loads.

LS-DYNA offers a range of element types to accommodate different structural components and behaviors. These element types include solids, shells, thick shells, beams, springs-dampers, discrete mass-inertia elements, truss elements, and membrane elements. To accommodate diverse material behaviors, LS-DYNA offers an extensive selection of over 130 metallic and non-metallic constitutive material models. Many of these models incorporate failure criteria and ten equations-of-state. This range of options allows LS-DYNA to simulate a wide variety of material behaviors. LS-DYNA employs the central difference method to solve the transient dynamic equilibrium equation, allowing for accurate simulations of dynamic systems. LS-DYNA offers comprehensive solutions for a diverse array of challenges, including multi-physics, multi-processing, multiple Stages, and multi-scale problems.

In addition, LS-DYNA offers the LS-PrePost tool, a versatile solution that covers both pre-processing and post-processing functionalities. This powerful tool enables users to easily generate inputs and visually analyze numerical results, simplifying the tasks involved in simulation preparation and analysis (ANSYS-LS, 2020) [35]. The analysis capabilities of LS-DYNA encompass a broad spectrum, including but not limited to nonlinear dynamics, coupled rigid body dynamics, quasi-static simulations, linear and nonlinear statics, eigenvalue analysis, Eulerian capabilities, ALE, Fluid-Structure Interactions (FSI), USA (Underwater Shock Analysis) coupling, multi-physics coupling, SPH (Smooth Particle Hydrodynamics), EFG (Element Free Methods), and more (ANSYS-LS, 2020) [35].

CHAPTER THREE

3.1 Introduction

In this study, the calibration of an air blast numerical model is carried out using a field blast test conducted by Yuan et al. (2017) [11]. The test involved subjecting a circular Reinforced Concrete (RC) column to blast loads generated by a 1.0 kg contact TNT air explosion. By reproducing the dynamic responses of the RC column induced by the contact blast loads, the numerical model developed in this study is rigorously validated against the experimental findings.

This chapter presents finite element numerical modeling, and the verification and validation of RC columns subjected to Air Blast scenarios using LS-DYNA. The chapter explores a wide range of aspects, including but not limited to element formulation, hourglass control, equations of motion, geometry and meshing techniques, boundary conditions, material models, ALE coupling, erosion algorithms, simulation, and output controls. Furthermore, this chapter emphasizes the validation of numerical models through meticulous comparisons of damage profiles, acceleration, and displacement time histories against experimental data and numerical results documented in open-source literature.

3.2 Modeling of RC Column Subjected to Air Blast Using LS-DYNA

3.2.1 Advantages of LS-DYNA for UNDEX Problems

For this study, LS-DYNA was chosen as the finite element (FE) modelling package from the currently available options. LS-DYNA is particularly advantageous for modeling UNDEX problems for various reasons. Firstly, it excels in capturing the non-linear behavior of materials like water, air, and solids, ensuring more accurate and realistic results. Secondly, LS-DYNA provides advanced element formulations specifically designed for UNDEX, such as the acoustic pressure element, which accurately models pressure waves in fluids. Moreover, the software's advanced meshing capabilities, including automatic mesh refinement, enable more efficient and accurate modeling by capturing material behavior effectively. Notably, it provides explicit coupling algorithms, such as the widely used ALE method, which allows for the accurate modeling of fluid-structure interaction (FSI) problems. This method is particularly suitable for problems involving large deformations and fluid flow. These attributes collectively establish LS-DYNA as the preferred software suitable choice for this study.

3.2.2 Element Formulation

LS-DYNA encompasses a wide range of element types, including discrete mass-inertia elements, springs-dampers, solids, shells, thick shells, and beams. Some examples of solid elements are shown in Figure (3.1). To accurately perform finite element analysis, it is crucial to assign the appropriate section properties to each part, whether it is a beam, shell, solid, or other element type. This is accomplished through the definition of the 'SECTION' keyword. In this thesis, the focus will be on utilizing solid, shell, and beam elements exclusively. While solid elements are capable of accurately representing three-dimensional states of stress, their mesh refinement can be computationally expensive due to the high number of degrees of freedom required for three-dimensional bodies. Consequently, the utilization of solid elements often necessitates additional time and effort in tasks such as mesh preparation, CPU usage, and post-processing. Nevertheless, solid elements, particularly the *SECTION_SOLID element type, are highly suitable for modeling thick parts or continuum structures.

The default configuration of the 8-node hexahedral solid element (ELFORM = 1) employs a single point integration scheme with hourglass control and constant stress. This element exhibits a commendable balance between efficiency and accuracy, enabling it to withstand substantial nonlinear deformations. With each of its 8 nodes offering 3 degrees of freedom, the element possesses a total of 24 degrees of freedom. This study utilizes Lagrange solid elements with the *SECTION_SOLID option and ELFORM = 1. Lagrange solid elements are specifically designed for three-dimensional modeling of solid structures. They employ Lagrange interpolation polynomials to approximate the displacement field within each element (ANSYS-LS-DYNA, 2023) [36].

The *SECTION_BEAM element in LS-DYNA is a one-dimensional finite element specifically designed for modeling structures that resemble beams. It facilitates the definition of cross-sectional properties for various types of beam elements, including beam, truss, discrete beam, and cable elements. The *SECTION_BEAM element utilizes the Euler-Bernoulli beam theory, which assumes slender beams and maintains the perpendicularity of cross-sections to the neutral axis during deformation.

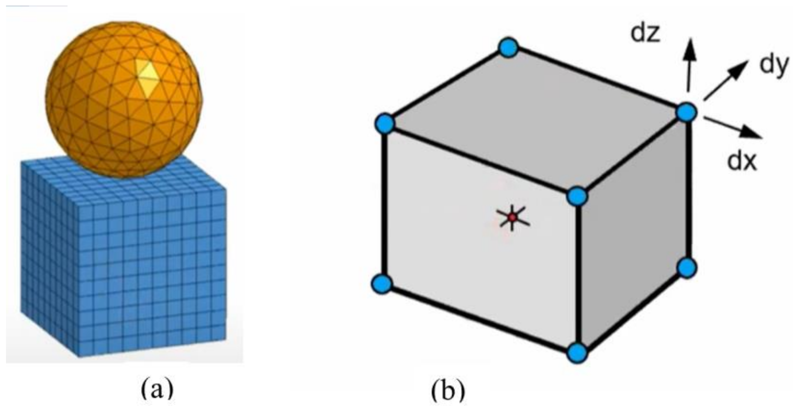

Figure 3. 1 (a) Examples of 3D Solid Elements (b) 8-node hexagonal solid element (Schmied, 2018) [42].

In this study, the *SECTION_BEAM component in LS-DYNA is utilized to simulate a structure with a beam-like shape. The ELFORM=1 option is selected to represent a Hughes-Liu beam element, which offers enhanced accuracy in modeling the cross section. To achieve more precise cross-sectional representation, the cross-sectional integration option is employed. In the case of a circular cross-section, the CST=1 option is utilized to specify a tubular cross section. This configuration includes a shear correction factor of 5/6, a diameter of 12.0 mm for longitudinal reinforcement and 6.0 mm for stirrups.

The *SECTION_SHELL element formulation in LS-DYNA enables the modeling of thin shell structures using a set of shell elements. Each shell element consists of four nodes and is characterized by parameters such as thickness, material properties, and orientation. This element formulation accounts for both membrane and bending behavior of the shell, facilitating accurate simulation of shell structures under different loading conditions. By employing *SECTION_SHELL, thin-walled structures such as plates, shells, and membranes can be effectively modeled using two-dimensional shell elements.

These shell elements feature a varying number of integration points throughout their thickness and can be regarded as plane stress elements with $\varepsilon_{zz} = 0$. In this study, the water tank is modeled using shell elements in the UNDEX model development process.

3.2.3 Hourglass Control

Hourglass (HG) modes are deformations characterized by zero energy and the absence of strain or stress (LS-DYNA Support) [37] . When these modes occur, the affected elements fail to accurately represent the true deformation behavior. Non-physical hourglass modes are commonly observed in solid, shell, and thick shell elements that employ a single integration point, indicating under-integration. To address the Hourglass effect, LS-DYNA provides several algorithms, with the default (type 1) algorithm being the most cost-effective but not necessarily the most effective solution in all cases. In this study, the Hourglass option IHQ.3, specifically the Flanagan-Belytschko viscous form with exact volume integration, is employed for the solid elements within the Lagrange Solid implementation. By incorporating the Flanagan-Belytschko viscous form, which is a type of artificial viscosity technique, and utilizing exact volume integration, this option effectively stabilizes the simulations and minimizes inaccuracies. By implementing this approach, the stability and accuracy of the Lagrange Solid element model are maintained, thereby reducing the occurrence of hourglass deformations that may lead to erroneous simulations.

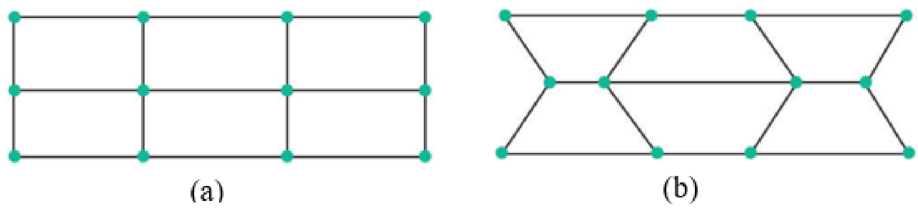

Figure 3. 2 Examples of hourglass effect (a) normal (b) with hourglass effect.

3.2.4 Time Integration

LS-DYNA adopts the central difference method for temporal integration of the model, which exhibits second-order accuracy and conditional stability. This method is implemented through explicit time integration, allowing the solution for the current time step to be directly derived from the solution of the previous time step, eliminating the need for solving simultaneous equations. As a result, the mass and damping matrices within the semi-discrete equation of motion are required to be diagonal (Equation 3.1). The calculation of acceleration at time n (Equation 3.2) involves the inversion of the mass matrix in the semi-discrete equation of motion, which is subsequently employed to determine the values of velocity and displacement. To ensure consistency, at each time step, the nodal positions are updated by incorporating the current nodal displacements with the nodal positions obtained from the preceding time step (Klenow, 2006) [38].

The equations of motion in semi-discrete form at time step n are given by Equation (3.1) (LSTC, 2019) [39]. In the given equation, **M** represents the diagonal mass matrix, $\mathbf{P}^n$ represents the contributions from external and body force loads, $\boldsymbol{F}^n$ represents the stress divergence vector (internal force), and $\mathbf{H}^n$ represents the hourglass resistance, and **a** as in

Eq. 3.2 represents nodal acceleration. To progress to the next time step, t^{n+1}(Equation 3.5) central difference time integration is employed.

Equation 3. 1

$$\mathbf{Ma} = \mathbf{P}^n - \mathbf{F}^n + \mathbf{H}^n$$

Equation 3. 1

$$\mathbf{a}^n = \mathbf{M}^{-1}(\mathbf{P}^n - \mathbf{F}^n + \mathbf{H}^n)$$

Equation 3. 2

$$\mathbf{v}^{\boldsymbol{n}+\mathbf{1}/\mathbf{2}} = \mathbf{v}^{\boldsymbol{n}-\mathbf{1}/\mathbf{2}} + \mathbf{a}^{\boldsymbol{n}}\boldsymbol{\Delta t}^{\boldsymbol{n}}$$

Equation 3. 3

$$\mathbf{u}^{\boldsymbol{n}+\mathbf{1}} = \mathbf{u}^{\boldsymbol{n}} + \mathbf{v}^{\boldsymbol{n}+\mathbf{1}/\mathbf{2}}\boldsymbol{\Delta t}^{\boldsymbol{n}+\mathbf{1}/\mathbf{2}}$$

Equation 3. 4

$$\text{Where; } \boldsymbol{\Delta t}^{\boldsymbol{n}+\mathbf{1}/\mathbf{2}} = \frac{(\boldsymbol{\Delta t}^{\boldsymbol{n}} + \boldsymbol{\Delta t}^{\boldsymbol{n}+\mathbf{1}})}{\mathbf{2}}$$

Where, the vectors $\mathbf{v}$ (Equation 3.3) and $\mathbf{u}$ (Equation 3.4) represent the global nodal velocity and displacement, respectively. To update the geometry, the displacement increments are added to the initial geometry. This process allows for the accurate representation of the structural deformations and subsequent changes in geometry throughout the analysis.

Equation 3. 5

$$\mathbf{x}^{n+1} = \mathbf{x}^0 + \mathbf{u}^{n+1}$$

Where $\mathbf{x}^0$ (Equation 3.6) is initial geometry in terms of modal coordinate referring to a representation of the system's state variables or degrees of freedom. The findings reveal that despite the increased storage requirements for storing the displacement vector, the results exhibit significantly reduced sensitivity to round-off errors. This observation, as reported by LSTC (2019) [39], highlights the trade-off between storage demands and the robustness of the results in the context of the analysis.

In the Explicit scheme for dynamic simulations, the system's response to an applied force on node N_2, as shown in Figure 3.3(a), is computed sequentially. The solver calculates the acceleration, velocity, and displacement of the node, considering mass and applied forces. Strain is evaluated based on material properties and displacement, providing information about material behavior. Using the calculated strain, the corresponding stress is determined using constitutive equations. The stress is then applied as a force on the subsequent node N_5 (Figure 3.3(a)), propagating forces and displacements through the interconnected nodes until the applied force is fully absorbed (Skill-Lync, 2022) [40]. To accurately determine stress and strain at the element level, the use of integration points is essential. These integration points allow for the evaluation of nodal results within elements. There are two types of integrated elements. Those are reduced and fully integrated elements. The reduced element, as shown in Figure 3.3(b), utilizes Gaussian Quadrature to integrate nodal results at a single integration point within the element.

This integration process enables the update of stresses and strains on the reduced element based on the nodal results obtained. On the other hand, the fully integrated element, illustrated in Figure 3.3(c), calculates nodal results at multiple integration points. By considering multiple integration points, the fully integrated element achieves a higher level of precision in the computed results at the element level. While the fully integrated element provides more accurate results, it incurs a higher computational cost due to solving multiple integration points. In contrast, the reduced integration element involves calculations at a single integration point, making it computationally less demanding.

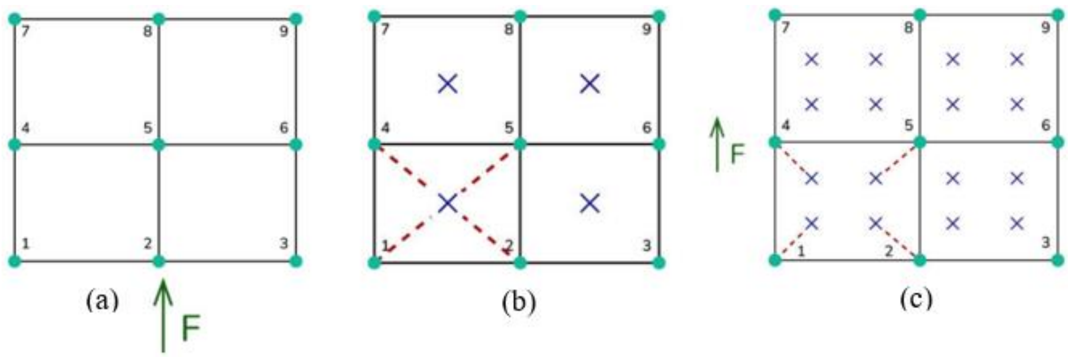

Figure 3. 3 Gaussian Integration points; (a) explicit (b) reduced, (c) fully integrated.

However, the reduced integration approach has two distinct disadvantages. First, it is associated with a potential decrease in accuracy compared to the fully integrated element, as the use of a single integration point may not capture all the necessary information accurately. Secondly, the reduced integration element is prone to hourglass deformation, as illustrated in Figure 3.2. Hourglass deformation occurs due to the reduced number of integration points, leading to distorted element behavior and inaccurate results. Thus, when selecting between reduced and fully integrated elements, the trade-off between computational efficiency, accuracy, and the potential for hourglass deformation should be carefully considered based on analysis requirements (Skill-Lync, 2022) [40].

3.2.5 Time Step Controls

The stability of the central difference method in the time step calculations for solid elements is determined by the size of the time step used in the analysis. To ensure stability, a maximum time step is established, which allows the model to remain stable for any time less than the maximum time step. LS-DYNA determines the critical time step for stability by computing the minimum critical time step across all the elements in the model. The critical time step size, $\Delta t_{\text{critical}}$, for solid elements is computed from (ANSYS-LS-DYNA, 2023) [36] as shown in Equation 3.8.

Equation 3. 6

$$L_c = \frac{V_{\text{element}}}{A_{\text{element}}}$$

Equation 3. 7

$$\Delta t_{\text{critical}} = \frac{L_c}{\sqrt{Q+(Q^2+c^2)}}$$

Where L_c in Equation 3.7 corresponds to the characteristic length of the smallest element in the mesh, V_{element} represents the element volume, A_{element} is the area of the largest side of the element, Q is a function of the bulk viscosity factors, and c is the speed of sound in the element.

For the Hughes-Liu beam and truss elements, the time step size is given by Equation 3.9 (ANSYS-LS-DYNA, 2023) [36].

Equation 3. 8

$$\Delta t_{critical} = \frac{L}{c}$$

Equation 3. 9

$$c = \sqrt{\frac{E}{\rho}}$$

where L is the length of the element, c in Equation 3.10 is the wave speed, E is Young's modulus, and ρ is the specific mass density.

The critical time step for shell elements can be determined using Equation 3.11, which involves the ratio of the characteristic element length to the speed of sound in the element. This calculation is used to control the minimum critical time step for the shell elements in the UNDEX model. For the shell elements, the time step size is given by (ANSYS-LS-DYNA, 2023) [36].

Equation 3. 10

$$\Delta t_{\text{critical}} = \frac{L_S}{c}$$

Equation 3. 11

$$c = \sqrt{\frac{E}{\rho(1-v^2)}}$$

Where L_s is the characteristic length and c is the sound speed (Equation 3.12).

3.2.6 Numerical Model Development for Air Blast Responses of RC Column

This section covers subtopics as meshing and experimental set up for model calibration, boundary conditions, material models, ALE coupling, erosion algorithm, simulation, and output controls.

3.2.6.1 Geometry, Meshing and Experimental Setup for Model Calibration

The successful validation of the numerical model of the research serves as a significant milestone, affirming its reliability and accuracy. This validated model, in conjunction with the forthcoming development and validation of the UNDEX model in the subsequent section, is used for conducting a comprehensive parametric study focusing on near-surface blast and UNDEX investigations.

This study aims to investigate the response of the RC column under various near-surface blasting and UNDEX scenarios. By systematically varying the parameters associated with the blasting scenarios, valuable insights into the structural behavior can be obtained. These insights contribute to a deeper understanding of the performance of RC columns in the face of explosive forces. Figures (3.5) and (3.6) provide comprehensive visual representations pertaining to the geometric characteristics, cross-sectional profile, and meshing arrangement employed in the LS-DYNA numerical model development process for the circular Reinforced Concrete (RC) column. The dimensions of the Ground

Surface were set to 2,000 mm x 2,000 mm x 500 mm, while the column foundation consisted of dimensions 1,000 mm x 1,000 mm x 500 mm, as illustrated in Figure (3.5). A fine mesh size of 8 mm was utilized for the concrete section in close proximity to the TNT charge, specifically within the range of 0 - 1,000 mm above the ground surface. A coarser mesh size of 20 mm in the Z direction was used for the remaining part of the column, as shown in Figure (3.6). The column foundation was modeled using a mesh size of 25 mm, while the ground surface was represented with a coarser mesh size of 50 mm.

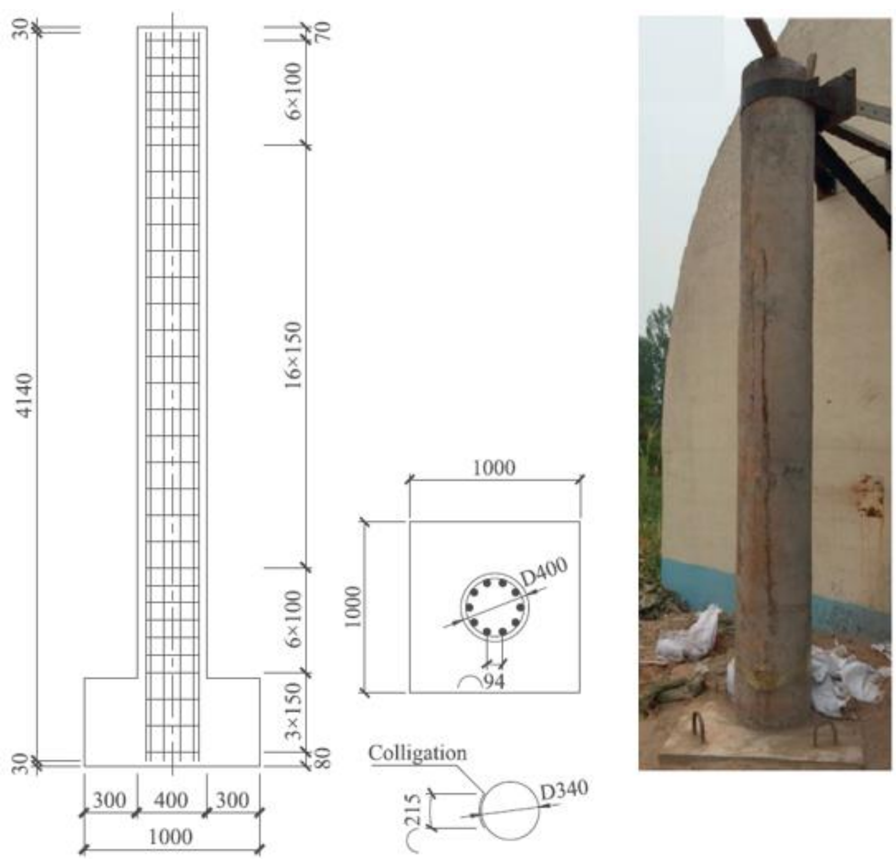

Figure 3. 4 Experimental Set up, units: mm (Yuan et. al, 2017) [21]

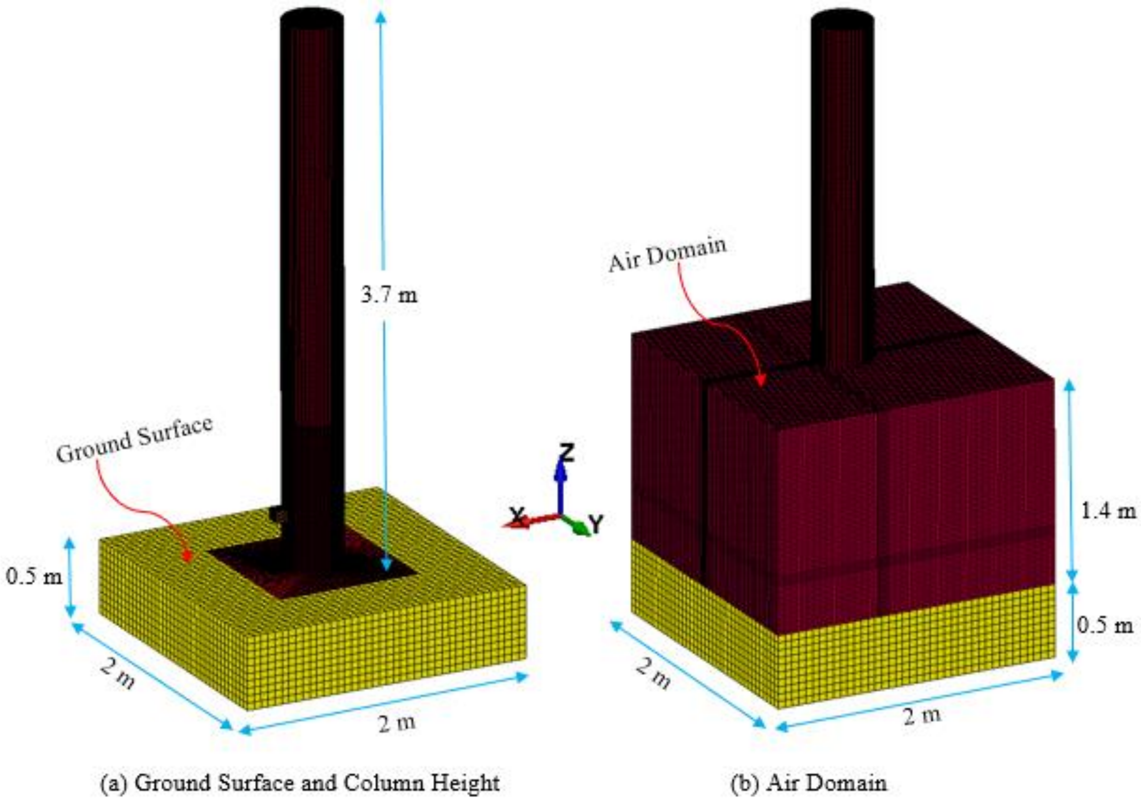

Figure 3. 5 Geometry and meshing details for the air blast model (a) ground surface; (b) air domain

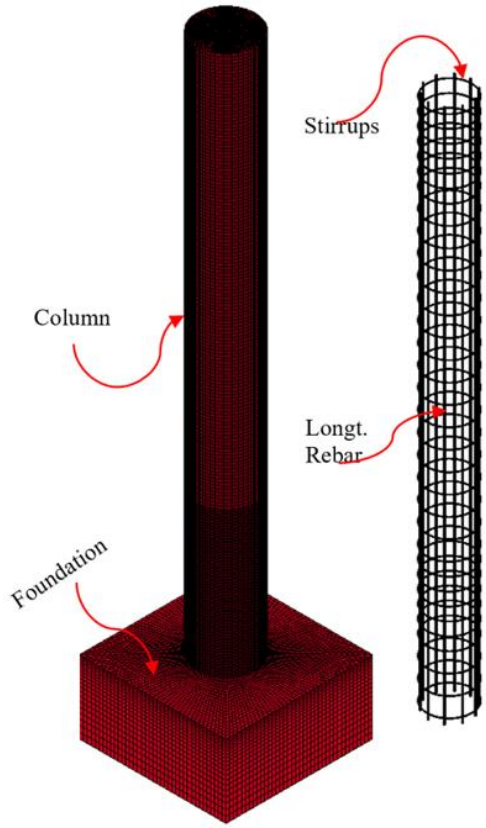

Figure 3. 6 Foundation, RC column, longitudinal, and lateral reinforcements

To maintain consistency with the experimental setup conducted by Yuan et al. (2017) [11] as shown in Figure (3.4), the top portion of the RC column was rigidly constrained using a steel hoop, while the column's foundation was securely embedded into the ground as shown in Figure (3.4). During the experimental test, a 1 kg TNT charge was positioned in close proximity to the front surface of the specimen. The center of the charge was maintained at a distance of 330 mm from the ground surface. The RC column specimen had a circular cross-section exhibited with a diameter of 400 mm, and a clear height of 3700 m. The reinforcement configuration employed in the specimen entailed the utilization of 12 mm diameter longitudinal rebar, 8 mm diameter stirrup rebar, and a concrete cover. The average cubic compressive strength of the concrete material was 38.5 MPa, while the longitudinal rebar, featuring ribbed steel bars, had a yield strength of 400 MPa. The stirrup has a yield strength of 300 MPa. All steel elements had an elastic modulus of 200 GPa. The experimental test set up conducted by Yuan et al. (2017) are also shown in Figure 3.4.

Three accelerometers were mounted on the rear surface of the RC column during the test at 330 mm, 1750 mm, and 3300 mm from the ground. To ensure accurate and efficient simulation results, the Concrete Column, its foundation pad, and the Ground Surface were modeled using Lagrange Solid elements with the *SECTION_SOLID option, employing the ELFORM = 1, which corresponds to the constant stress solid element.

The concrete column, including its foundation pad had a total of 884,640 Lagrange Solid elements, whereas the ground surface had a total of 12,000 Lagrange Solid elements. With the mesh configuration, a balance between accuracy and computational efficiency was achieved, enabling reliable simulations for the structural response of the analyzed components. The air and explosives were modeled in LS-DYNA, *SECTION_SOLID option, employing the ELFORM = 11, which corresponds to 1-point ALE multi-material element. The air domain had dimensions of 2 m x 2 m x 1.4 m, as shown in Figure 3.7. An ALE (Arbitrary Lagrangian-Eulerian) Solid approach utilizing a mesh size of 20 mm is employed. This results in having a total of 774,163 elements encompassing the air model.

Embedded within the air model is the TNT explosive, which has dimensions of 8.5 cm x 9 cm x 8 cm in the X, Y, and Z directions, respectively, as shown in Figure 3.7 (b). A uniform mesh size of 12 mm is employed for the explosive. This mesh configuration entails a total of 294 ALE Solid Explosive TNT elements. A total of 1,677,589 elements were utilized for the air blast modeling process. By incorporating these mesh sizes and element counts, the numerical model effectively captures the characteristics and behavior of both the air domain and the embedded TNT explosive, facilitating the analysis of the blast event.

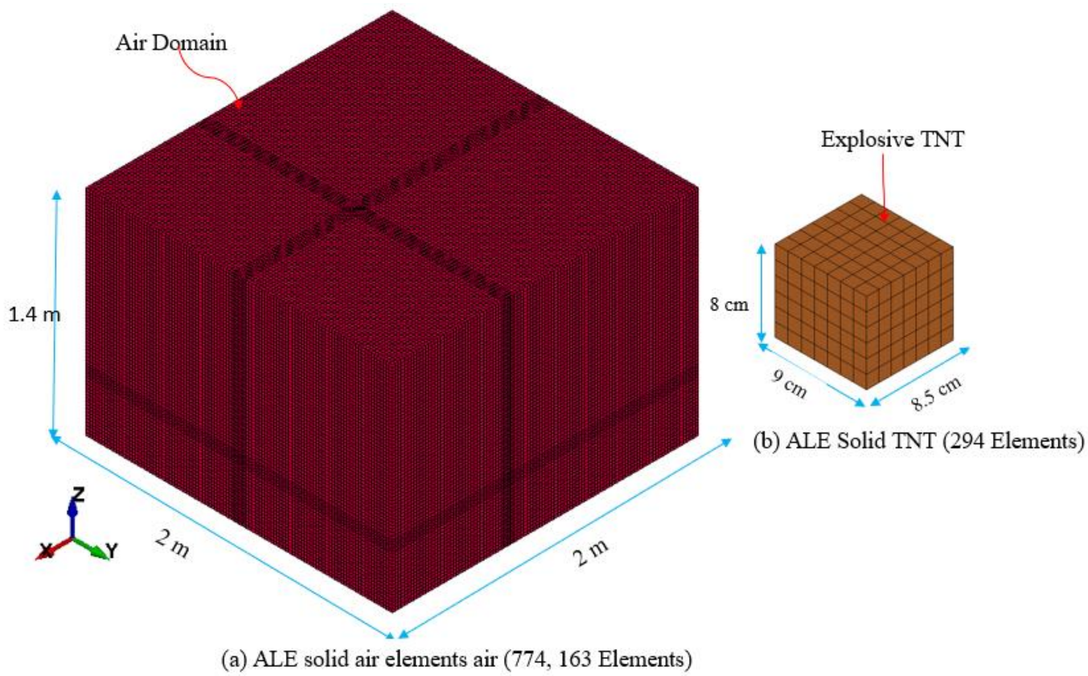

Figure 3. 7 ALE solid (a) air and (b) TNT elements

When it comes to beam elements used to model longitudinal and lateral reinforcements, such as rebar and stirrups embedded within concrete structures, meshing involves dividing the reinforcement into smaller sections along its length. This division allows for capturing the localized response and deformation of the reinforcement accurately. The option *SECTION_BEAM has been utilized in this study to represent the steel reinforcing bars embedded in the reinforced concrete (RC) column. It employs the Element Formulation parameter, ELFORM = 1, which corresponds to the Hughes-Liu formulation with cross-section integration. For the shear factor, a recommended value of SHRF = 5/6 has been adopted. This factor accounts for the reduction in shear capacity due to the presence of steel reinforcing bars. To integrate the behavior of the beams, a quadrature rule or rule number, QR/IRID = 2, has been employed. This rule corresponds to the 2x2 Gauss quadrature. The cross-section type used is CST = 1, which represents a tubular section. The thicknesses of the beams have been set to 8 mm and 12 mm for the stirrups and longitudinal rebars, respectively. A fine mesh with a size of 8 mm has been employed for steel bars in close proximity to the TNT charge. For the remaining sections of the rebars, a coarser mesh with a size of 20 mm has been used in the Z direction. Table 3.1 summarizes the geometry, element types and mesh sizes of the finite element model.

Table 3. 1 Details of FEM for air blast modeling

Material Type	Dimensions (mm)	Element Type	Mesh size (mm)	No of Elements
Column	H= 3700 mm; D= 400 mm	Lagrange Solid	Fine=8 mm; Coarse= 20 mm	884,640
Foundation	W=1000 mm; L=1000 mm; H=500 mm		25 mm	
Longitudinal Rebar	H=4140 mm; #'s10-D=20 mm	Beam	Fine=8 mm; Coarse= 20 mm	3,420
Stirrups	D=337mm; #'s32-D=8 mm			3,072
Ground Surface	W=2000 mm; L=2000 mm; H=500 mm	Lagrange Solid	50 mm	12,000
TNT	W=85 mm; L=90 mm; H=80 mm	ALE Solid	12 mm	294
Air	W=2000 mm; L=2000 mm; H=1400 mm		20 mm	774,163
			Total	**1,677,589**

3.2.6.2 Boundary Conditions

Boundary conditions play a critical role in accurately simulating the behavior of structures in LS-DYNA under different loading and environmental conditions. They define the interaction between the structure and its external surroundings, as well as the transmission of applied loads to the model. LS-DYNA offers various types of boundary conditions. One frequently used fixed boundary condition is fixed displacement. It restricts the specified degree of freedom (DOF) of a node, preventing any movement or deformation in that particular direction. By fixing a node's displacement in the X, Y, or Z direction, or a combination thereof, this condition is often applied to represent immovable supports or rigid connections within the model. For this study, the *BOUNDARY_SPC_SET keyword is utilized to define the fixed conditions. In this case, the bottom nodes and top of the reinforced concrete (RC) column are subjected to fixed boundary conditions. Following the experimental set up Yuan, et.al (2017) [11], the translational and rotational degrees of freedom in the local x, y, and z directions are constrained as shown in Figure 3.8.

The LS-DYNA keyword *BOUNDARY_NON_REFLECTING plays a significant role in numerical analyses aimed at simulating non-reflecting boundaries which are primarily employed to absorb or dampen outgoing waves and prevent their reflection back into the computational domain. These boundaries are particularly advantageous when addressing problems involving wave propagation, such as simulations of acoustic phenomena or fluid-structure interactions. The utilization of the *BOUNDARY_NON_REFLECTING keyword proves instrumental in minimizing undesirable reflections at the boundaries, which can adversely impact the accuracy of the results. By implementing non-reflecting boundaries, the simulation effectively absorbs and dissipates waves reaching the edges of the computational domain. Consequently, this approach enables a more precise representation of the system's behavior, reducing the presence of unwarranted wave reflections and associated artifacts that may distort the simulation results. In the present simulation, the ground surface has been specifically defined as non-reflective boundary surfaces through the implementation of the *BOUNDARY_NON_REFLECTING keyword.

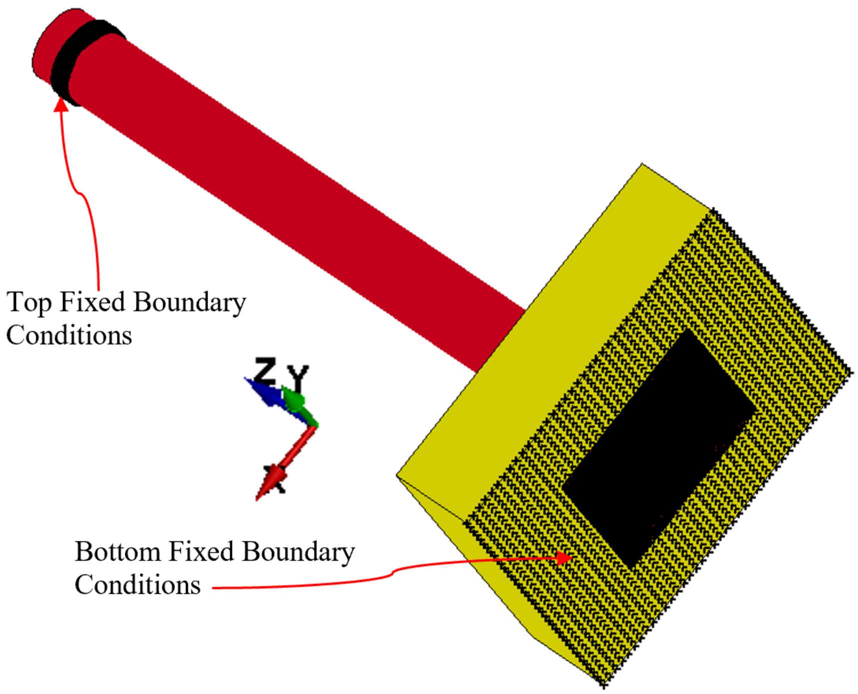

Figure 3. 8 Top and bottom fixed boundary conditions

3.2.6.3 Material Models Employed in LS-DYNA

In LSDYNA, there are several material models available for simulating the behavior of concrete materials. Among these models some of them are *MAT_BRITTLE_DAMAGE (MAT_96), *MAT_JOHNSON_HOLMQUIST_CONCRETE (MAT_111), *MAT_PSEUDO_TENSOR (MAT_16), *MAT_CSCM_CONCRETE (MAT_159), and *MAT_CONCRETE_DAMAGE_REL3 (MAT_72_REL3). The MAT_72_REL3 material model, known as Release III of the K&C Concrete Model, is specifically used in this study. It incorporates characteristics such as strain-rate effects, plasticity, and damage softening following failure ANSYS-LS-DYNA (2023) [36] .

The reliability and accuracy of K&C model have been verified in Yuan et al. (2017) [11] and Li et al. (2014) [41]. For this study, the average cubic compressive concrete strength is set at 38.5 MPa, a value consistent with the experimental study conducted by Yuan et al. (2017) [11]. Furthermore, a density of 2400 kg/m^3 is assigned. For reinforcing steel, the material model MAT_PIECEWISE_LINEAR_PLASTICITY (MAT_024) was employed to simulate the behavior of both longitudinal reinforcement bars and stirrups in the reinforced concrete (RC) elements. The model was selected because it accounts for the influence of strain rate effects needed for dynamic loading scenarios.

MAT_024 offers the capability to define an arbitrary stress versus strain curve and an arbitrary strain rate curve, allowing researchers to tailor the material properties to match the specific behavior of the reinforcement being modeled. The stress-strain relationship can be customized to accurately capture the response of the reinforcement bars and stirrups, considering variations in yield strength, ultimate strength, and strain hardening characteristics. Furthermore, the material model allows for the definition of failure criteria based on plastic strain or a minimum time step size. The plastic strain-based failure criteria enable the progressive damage modeling of the reinforcement, including yielding, strain softening, and fracture. On the other hand, the minimum time step size-based failure criteria ensure computational stability by preventing unrealistic deformations during extremely rapid events. Table 3.2 summarizes the input parameters selected for the concrete and reinforcement material models in this study.

Table 3. 2 Input parameters for the steel reinforcement material model

MAT_PIECEWISE_LINEAR_PLASTICITY (MAT_024) (Yuan et. al. 2017)	
Material Property	**Magnitude**
Mass density	7850 kg/m^3
Young's Modulus	2.00E+11Pa
Yield Stress for longitudianl rebars	400E+6 Pa
Yield Stress for stirrup rebars	300E+6 Pa
Tangent modulus	2.00E+9 Pa
Poisson's ratio	0.3

The Jones, Wilkins, and Lee (JWL) EOS implemented in LS-DYNA, specifically the *MAT_HIGH_EXPLOSIVE_BURN command, is commonly used to characterize the detonation properties of the high explosive material, for this study is TNT (Trinitrotoluene). Table 3.3 summaries the input parameters for the TNT model.

Table 3. 3 Input parameters for TNT material model.

*MAT_HIGH_EXPLOSIVE_BURN (MAT_008) (Yuan et. al. 2017)									
A (Gpa)	**B (GPA)**	**R_1**	**R_2**	**ω**	**V**	**E (MJm^{-3})**	**ρ (Kgm^{-3})**	**v (ms^{-1})**	**P (Gpa)**
3.74E+02	3.747	4.15	0.9	0.35	1	6.00E+03	1.63E+03	6.93E+03	2.10E+01

The utilization of the JWL EOS further elucidates the dynamic relationship between pressure (P) and the relative volume (V), in conjunction with the initial energy per initial volume (E). By encapsulating these essential parameters, the JWL EOS as shown in

Equation. 3.13 offers a comprehensive framework for describing the explosive's response during the simulation Yuan et al. (2017) [11] and Tabatabaei et al. (2012) [42].

Equation 3. 12

$$P = A\left(1 - \frac{\omega}{R_1 V}\right)\exp\left(-R_1 V\right) + B\left(1 - \frac{\omega}{R_2 \omega}\right)\exp\left(-R_2 V\right) + \frac{\omega}{V}E$$

Where P is the hydrostatic pressure exerted on the explosive material. V is the relative volume or the expansion of the explosive under investigation. E is the energy per initial unit volume of the explosive; and A, B, R_1, R_2, and ω are constants dependent on the type of the explosive. The material parameters utilized for the TNT explosive in this investigation shown in Table 3.3 and are obtained from Yuan et al. 2017 [11] and the study conducted by Wang et al. 2005 [43].

In this study, the air is characterized as an ideal gas. To represent its behavior, a *MAT_NULL material model was employed utilizing a linear polynomial Equation of State (EOS) based on internal energy per unit initial volume, denoted as E as shown in Equation (3.14). The chosen EOS provides a mathematical framework for describing the relationship between pressure and other thermodynamic properties of the air. The pressure term is mathematically expressed using Equation (3.14) (Tabatabaei, 2012) [42]:

Equation 3. 13

$$P = C_0 + C_1\mu + C_2\mu^2 + C_3\mu^3 + (C_4 + C_5\mu + C_6\mu^2)E$$

Where $C_0, C_1, C_2, C_3, C_4, C_5$, and C_6 are constants and $\mu = \frac{\rho}{\rho_0} - 1$ with

$\frac{\rho}{\rho_0}$ representing the ratio of current density to initial density.

Specifically, C_0, C_1, C_2, C_3, C_6 are set to zero, while C_4, C_5, and γ-1 are assigned a value of 0.4 the ideal gas behavior is shown in Equation (3.15).

Equation 3. 14

$$p = (\gamma - 1)\frac{\rho}{\rho_0}E$$

The parameter γ represents the ratio of specific heat in the system. In this study, an initial air density of 1.29 kg/m^3 is used. Moreover, the initial internal energy per unit volume of air is set at 0.25 MPa. These values provide the necessary parameters to accurately describe the properties of air.

3.2.6.4 ALE Coupling

In the study of fluid or fluid-like behavior, the utilization of a Lagrangian approach, where the deformation of the finite element mesh exactly mirrors the deformation of the material, is often unsuitable due to the substantial deformation experienced by the material. The distortion will result in progressively smaller explicit time steps and ultimately lead to instability (Nazem et al. 2009) [44]. In contrast, an alternative solution method known as ALE is more appropriate for modeling fluid or fluid-like behavior. In this approach, the materials flow or advect through a Eulerian/ALE mesh, which is either fixed in space (Eulerian) or capable of moving in accordance with user-defined instructions (ALE). This methodology offers improved suitability for accurately representing the behavior of fluids or fluid-like substances.

Within the LS-DYNA framework, it is possible to employ a combination of Lagrangian and Eulerian/Arbitrary Lagrangian Eulerian (ALE) solution methods in the same model to effectively handle fluid-structure interaction by means of a coupling algorithm. This capability enables the modeling of components that undergo a moderate amount of deformation, such as structural elements made of metals, RC structures using Lagrangian elements. On the other hand, fluids like air, water and TNT can be modeled more accurately using Eulerian/ALE elements. This integration of solution methods provides a comprehensive approach to simulate the interaction between fluids and structures within the LS-DYNA framework (Aerospace Working Group, 2021) [45].

Considering a 2D example depicted in Figure 3.9, a solid metal object being subjected to movement and subsequent deformation is qualitatively demonstrated. In this scenario, three distinct formulations are available for consideration: Lagrangian (Formulation 1), Eulerian (Formulation 2), and ALE (Formulation 3). In the Lagrangian approach (Formulation 1), the nodes constituting the mesh are affixed to the hypothetical material points. These nodes undergo movement and deformation aligned with the material they represent. The Lagrangian method enables tracking the motion and deformation of the material accurately. In contrast, the Eulerian approach (Formulation 2) involves the utilization of two overlapping meshes. One mesh, referred to as the background mesh, remains stationary in space. The second mesh is associated with the material itself, which "flows" through the fixed background mesh. The Eulerian approach allows for modeling scenarios where the material moves independently of the background mesh, providing flexibility in simulating fluid-like behaviors.

The ALE element formulation (Formulation 3) also involves two overlapping meshes, similar to the Eulerian approach. However, in ALE, the background mesh can move arbitrarily in space, enabling it to adapt to the motion of the material. The material "flows" through the moving background mesh, ensuring accurate representation of the fluid or fluid-like behavior. The ALE method offers a balance between the Lagrangian and

Eulerian approaches, providing the advantages of both while accommodating large deformations and complex material movements (LSTC, 2003) [46].

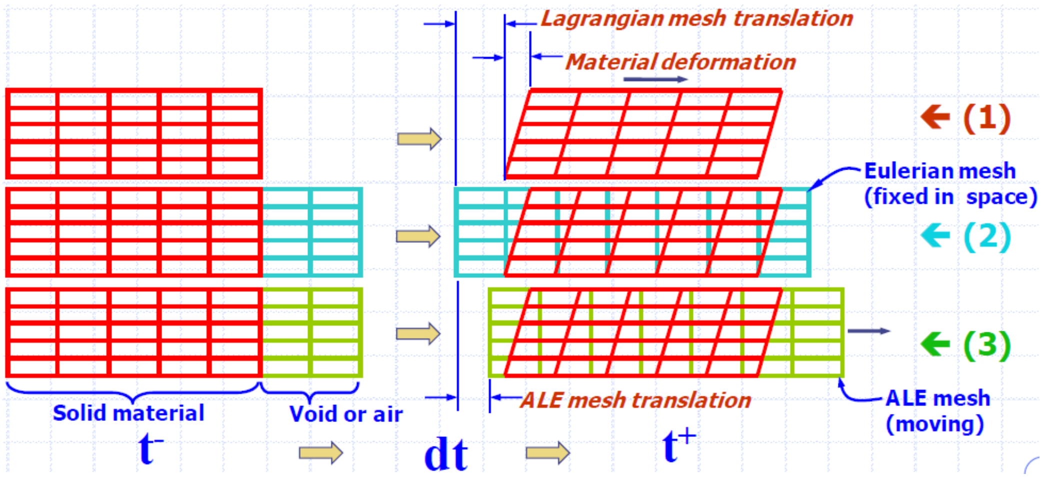

Figure 3. 9 Illustration of ALE Element Formulations (LTSC, 2003) [52].

The Arbitrary Lagrangian Eulerian (ALE) mesh in this study is directed to undergo specific prescribed movements as the solution progresses. In this regard, the Eulerian approach represents a special case of ALE wherein the prescribed velocity of the reference mesh is set to zero. Unlike the fully Lagrangian scenario, wherein the mesh and material move in exact correspondence, the ALE mesh and material exhibit differential movement. Consequently, material advection across element boundaries remains a necessity, but the extent of such advection during each time step is generally reduced compared to the Eulerian approach due to the movement of the mesh itself. It is commonly understood that minimizing material advection per time step enhances the accuracy of the simulation (Aerospace Working Group, 2021) [45]. In the LS-DYNA software, the multi-material

ALE element formulation is implemented through the utilization of the *SECTION_SOLID keyword option (ELFORM = 11). For ALE/Euler multi-material formulations, it is customary to employ a uniformly fine mesh, which helps achieve accurate representations of the system under investigation.

In cases where there is a need for interaction between Eulerian or Arbitrary Lagrangian Eulerian (ALE) components and Lagrangian components, it becomes essential to establish a coupling mechanism, commonly referred to as fluid-structure interaction, as shown in Figure (3.10). In the context of LS-DYNA simulations, Fluid-Structure Interaction problems predominantly involve the modeling of fluids using ALE hexahedrons and structures using Lagrangian solid elements. This approach allows for the accurate representation of the dynamic interaction between the fluid and solid components within the computational framework. In such a model, it is common for the Lagrangian mesh to have non-overlapping nodes with the ALE mesh. Instead, the interaction between the two meshes (Lagrangian and ALE) is achieved through a coupling algorithm implemented with the command *CONSTRAINED_LAGRANGE_IN_SOLID. This coupling mechanism generates forces that effectively prevent the ALE material from penetrating into the Lagrangian parts as illustrated in Figure (3.10). The coupling process is a crucial and at times intricate aspect of ALE modeling.

In LS-DYNA, different approaches are employed based on the type of contact occurring within the simulation. When a Lagrangian part comes into contact with another Lagrangian part, a CONTACT approach is utilized. On the other hand, when a Lagrangian part interacts with Eulerian or ALE components, a COUPLING approach is employed.

These distinct approaches enable accurate handling of the interactions between different types of elements within the simulation, ensuring reliable and realistic results (LSTC, 2003) [46].

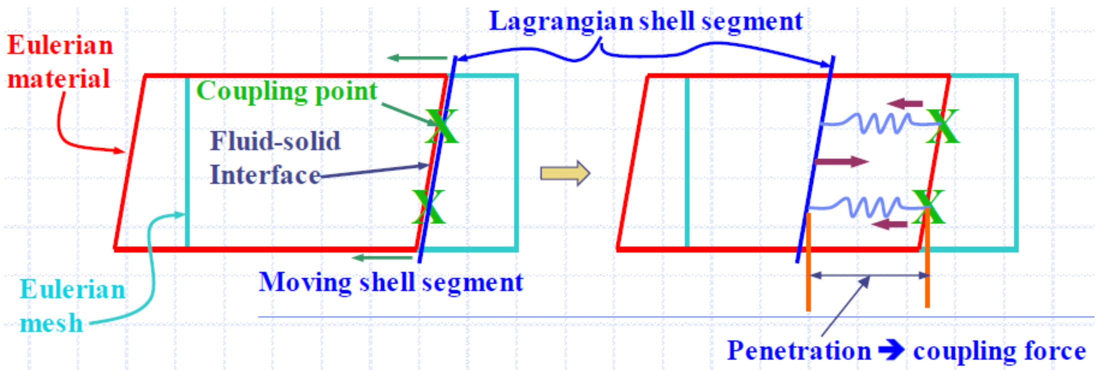

Figure 3. 10 Coupling Lagrangian Solid -ALE Elements (LTSC, 2003) [52]

By employing LS-DYNA's *CONSTRAINED_LAGRANGE_IN_SOLID command, the independent Lagrangian mesh, representing the slave part, is effectively coupled with the independent ALE mesh, representing the master part. This coupling is achieved through a "penalty-coupling" factor, which quantifies the relative displacement between a Lagrangian node and the corresponding location of the Eulerian fluid material. During the simulation, each slave node is examined to determine if it penetrates the surface of the master part (Figure 3.10). In the absence of any penetration, no further action is taken. However, if a slave node does penetrate the master surface, an interface force is computed and distributed to the Eulerian fluid nodes. This force facilitates the interaction and exchange of information between the Lagrangian and Eulerian components, ensuring the accurate representation of their coupling behavior within the simulation (Yuan et al., 2017 [11]; Trevino, 2000) [47].

The selection of an appropriate penalty coupling quadrature, denoted as NQUAD in the *CONSTRAINED_LAGRANGE_IN_SOLID command, relies on the relative sizes of the Lagrangian and Arbitrary Lagrangian Eulerian (ALE) elements. The default value of NQUAD=2 is generally suitable when the ALE and Lagrangian meshes possess similar element sizes. However, if the ALE elements are smaller than the Lagrangian elements, a larger value of NQUAD may be necessary to accurately capture the coupling behavior.

In the current study, the default value of NQUAD=2 has been utilized, along with the CTYPE parameter set to 5, representing the chosen coupling type. Additionally, the penalty coupling approach has been adopted, which allows for erosion in the Lagrangian entities (solid elements). This combination of settings and options ensures appropriate coupling and erosion behavior within the Lagrangian components considered in the analysis.

3.2.6.5 Erosion Algorithm

The erosion algorithm implemented in LS-DYNA serves as a robust and effective tool for simulating material removal or erosion phenomena within a computational simulation. This algorithm provides the capability to accurately model a wide range of erosion mechanisms, including spallation, fracture, fragmentation, and material loss caused by high strain rates, impact events, or other dynamic processes. By dynamically removing elements or parts of elements from the computational model, the erosion algorithm enables the realistic representation of material degradation and erosion processes during the simulation (Michaloudis et al. 2011) [48]. LS-DYNA incorporates multiple erosion modeling techniques to accommodate diverse material behaviors and erosion phenomena. These techniques encompass node-based erosion, element-based erosion, and coupled erosion. The selection of the appropriate erosion modeling technique depends on the specific characteristics of the material under consideration and the erosion mechanism to be simulated (Horta, et al., 2010) [49].

In node-based erosion modeling, erosion dynamics are evaluated based on the displacement or damage characteristics of individual nodes within the material mesh. Once predefined erosion criteria are satisfied, the elements connected to these nodes are selectively eliminated from the simulation. Node-based erosion is particularly well-suited for the simulation of erosion in ductile materials, wherein material removal predominantly arises from localized deformation or strain concentration phenomena. On the other hand, element-based erosion modeling involves the removal of entire elements within the material mesh based on predefined erosion criteria. This technique finds extensive application in the simulation of erosion phenomena in brittle materials, characterized by material loss resulting from fracture or fragmentation mechanisms.

It is important to note that the erosion algorithm employed in LS-DYNA lacks a solid physical foundation and should therefore be utilized with care and caution. The algorithm does not adhere to well-established physical principles and theories. It is imperative to exercise discretion in applying the erosion algorithm to simulations. Setting large erosion criteria can result in excessive distortion of elements, leading to computational overflow and numerical instability. Conversely, using small erosion criteria may lead to premature and excessive deletion of elements, which violates the principles of mass and momentum conservation. Therefore, a careful balance must be struck in selecting appropriate erosion criteria to ensure accurate and reliable simulation results. These concerns have been highlighted in studies conducted by Yuan et al. (2017) [11] and Li et al. (2014) [41]. In consideration of the strain rate's influence on concrete tensile strength, Xu and Lu (2006) [50] introduced an erosion criterion based on the principal strain. This erosion criterion has demonstrated the capability to effectively simulate spall damage in concrete materials.

In the present study, a series of extensive simulations were conducted using various conservative erosion criteria. It was observed that employing a principal strain threshold of 0.5 as the erosion criterion yielded reliable predictions of the response of RC columns and was used throughout this study. This is consistent with Codina et al.'s (2016) findings on suitability of using a principal strain threshold of 0.5 for erosion criterion in LS-DYNA. The erosion criterion based on the maximum principal strain can be invoked by utilizing the MXEPS option.

3.2.6.6 Simulation and Output Controls

In this study, an important simulation control utilized is the termination time, which is a crucial aspect of air blast simulations in LS-DYNA. The termination time denotes the duration of the simulation, signifying the point at which the simulation is considered complete. It is at this specific time when the solver ceases the advancement of the simulation and generates the final results. In the context of air blast simulations, the termination time is typically chosen to allow for the complete propagation and dissipation of the blast wave, as well as the associated effects, ensuring a comprehensive representation of the simulation's behavior (Glance, 2019) [51]. The termination time should be carefully determined to strike a balance between capturing the desired phenomena with sufficient duration and avoiding excessive computational costs and runtime.

In the present study, a termination time of 10 milliseconds was chosen based on the understanding that the most significant structural responses and damages resulting from contact blast loads typically occur within several milliseconds. This duration was deemed sufficient to capture the critical effects of the blast and the subsequent structural behavior. In LS-DYNA, the time step size, controlled by the keyword *CONTROL_TIMESTEP, is another significant simulation control parameter that governs the temporal resolution of the simulation. The time step size directly influences the precision and accuracy of the simulation results. A smaller time step size allows for a more detailed and accurate representation of the system's response to dynamic forces and events. However, decreasing the time step size increases the computational burden and prolongs the simulation runtime.

Conversely, a larger time step size can expedite the simulation process and reduce computational costs. However, using an excessively large time step size can lead to inaccurate results and numerical instability, as it may fail to capture rapid changes and high-frequency oscillations within the system. To strike a balance between computational efficiency and result accuracy, the time step size needs to be carefully chosen. It should be small enough to adequately capture the relevant dynamic phenomena, while still being large enough to ensure computational feasibility (Skill-Lync, 2022) [40].

In this study, some specific LS-DYNA simulation output control keywords were utilized to efficiently handle and extract valuable data from the simulations conducted. These are, *DATABASE_OPTION_ASCII_Option, *DATABASE_BINARY_D3PLOT, and *DATABASE_HISTORY_NODE_ID. Each of these simulation outputs played a crucial role in managing the information generated during the simulations. The LS-DYNA keyword *DATABASE_OPTION_ASCII_Option facilitated the specification of the desired format for storing the simulation results. By utilizing this keyword, the option to choose between ASCII and binary formats for data storage was made possible.

In the context of *DATABASE_OPTION_ASCII_Option, assigning a value of 1 indicated the selection of the ASCII format for saving the simulation results. ASCII files store data in a human-readable text format, enhancing interpretability and facilitating analysis using external post-processing tools or software. This format proved particularly advantageous for post-processing tasks and data manipulation since it provided direct access to the simulation data in a readable format, enabling efficient examination and interpretation of the results (ANSYS-LS-DYNA, 2023) [36]

In this simulation, an additional output control was implemented using the LS-DYNA keyword *DATABASE_BINARY_D3PLOT to manage the output format for the D3PLOT file. The D3PLOT file format, which is a binary format, efficiently stores various simulation results, including nodal and elemental data. By incorporating this keyword, the generation of D3PLOT files during the simulation was enabled, providing comprehensive information regarding the model geometry, element connectivity, nodal displacements, stresses, strains, and other pertinent data at specific output intervals. In addition, the LS-

DYNA keyword *DATABASE_HISTORY_NODE_ID served as an important output control mechanism, specifically designed for recording nodal history data. By employing this keyword, it is possible to define the specific nodes for which historical data will be captured during the simulation.

In the context of contact air blast simulations on reinforced concrete columns, *DATABASE_HISTORY_NODE_ID can be effectively employed as sensors to monitor and document the behavior of these elements throughout the simulation process. This facilitates a comprehensive understanding of the response and performance of RC columns under contact blast loading conditions. During the simulation, LS-DYNA records nodal history data for the designated nodes, encompassing essential information such as displacements, velocities, accelerations, forces, or any other desired variables. This data can be outputted to an ASCII file or other compatible formats, facilitating subsequent analysis and post-processing. (ANSYS-LS-DYNA, 2023) [36].

3.2.7 Validation of Numerical Model for Air Blast Responses of RC Column

Numerical modeling plays a crucial role in understanding and predicting the behavior of complex dynamic events, such as air blasts and UNDEX resulting from explosions. In recent years, LS-DYNA has emerged as a powerful simulation tool extensively employed to replicate diverse blast scenarios. However, the precision and dependability of these numerical models are heavily contingent upon their validation against experimental data. Numerical model validation involves comparing the results obtained from the simulation with the corresponding experimental measurements to assess the model's capability to accurately replicate real-world blast phenomena. This process not only ensures the credibility of the numerical model but also provides insights into the underlying physics of the blast event. This section of the thesis presents the comprehensive validation of the numerical model pertaining to the air blast phenomenon. This model was carefully developed using a rigorous framework involving established procedures, scientific methods, and advanced material models within the LS-DYNA simulation software, as detailed in the preceding section (3.2.6).

The calibration of the finite element model in this study involved utilizing openly available experimental data, which was previously described in detail in section (3.2.6.1). The verification process and subsequent validation of the air blast model included comparing and evaluating the proposed numerical model with results reported in Yuan et al. (2017) [11], and Yang et al. (2019) [17]. Damage profiles, peak accelerations and mid-point deflection were compared.

3.2.7.1 Comparisons of Damage Profiles

A damage profile is a representation of the extent of damage in a material. In numerical models, it is used to predict the failure of materials under different loading conditions. The damage profile is usually defined as a scalar or tensor field that varies with the location in the material and the loading conditions (Huynh. et. al., 2020) [52]. In the context of contact detonation, it is observed that the response of the column is characterized by strong localization and high-frequency behavior. This complex behavior necessitates the use of a significantly refined discretization with a reduced element size in order to accurately capture the associated damage and local acceleration phenomena Yuan et. al. 2017) [11]. This approach ensures that the finite element model employed in this study possesses the necessary resolution to capture the intricate details and accurately predict the localized response.

To align with the experimental test setup proposed by Yuan et al. (2017) [11] for accelerometers, the numerical model integrated three distinct nodes. These nodes were strategically defined within the model by employing the LS-DYNA keyword *DATABASE_HISTORY_NODE_ID. The purpose of these nodes was to serve as numerical sensors, specifically designated as Sensor 1, Sensor 2, and Sensor 3 throughout the numerical modeling and simulation process, as depicted in Figure 3.11 (a & b). By incorporating this configuration of numerical sensors, valuable data, such as accelerations and deflections, was acquired concerning the structural behavior and response to the explosive detonation of the 1 kg TNT.

The experimental findings presented by Yuan et al. (2017) [11]regarding circular column specimens subjected to a 1 kg contact explosion are shown in Figure 3.12. Analyzing these results reveals a noteworthy observation: the circular columns exhibited substantial compressive failure concentrated primarily on the surface of the column. Furthermore, the damage zone was approximately 60 cm across the specimens. This consistent damage zone height signifies the extent of structural deterioration experienced by the circular columns under the influence of the explosive blast. Such observations provide valuable insights into the response of circular columns to contact explosions.

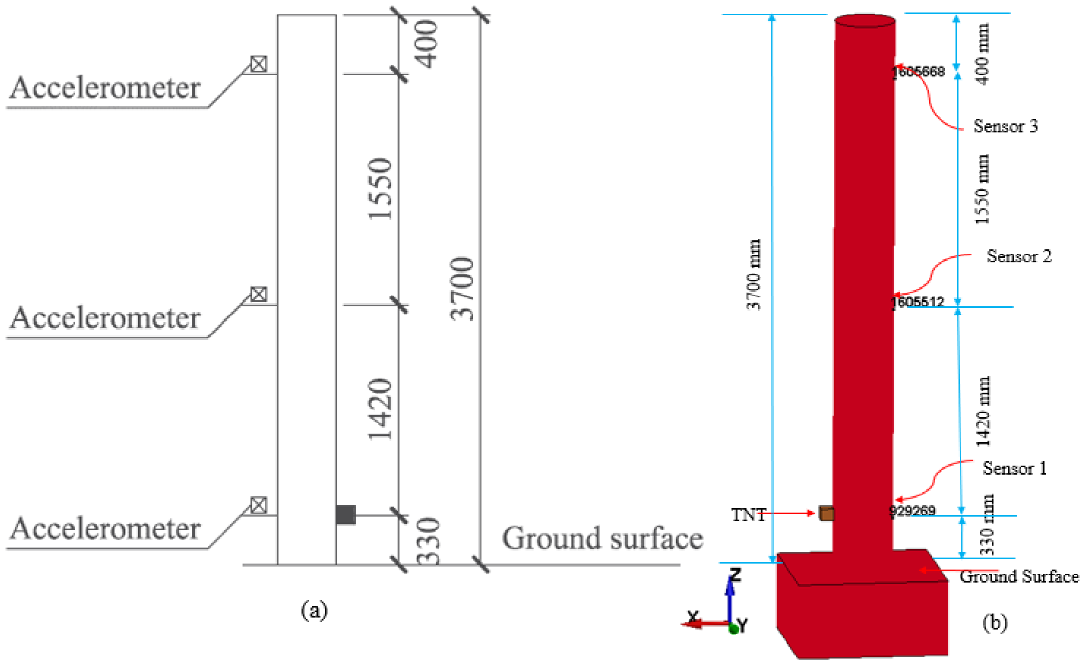

Figure 3. 11 Accelerometer layouts (Yuan, et. al., 2017) and (this study)

In Yuan et al.'s experiments, the cover concrete layer on the front surface of the specimens suffered complete destruction, primarily due to the application of extraordinarily high compressive blast loads. Additionally, the column's side surfaces exhibited severe damage to the concrete, as visually depicted in Figure 3.12 (a), (b), and (c). Conversely, a lesser degree of damage was observed on the column's back surface, as indicated in Figure 3.12 (d).

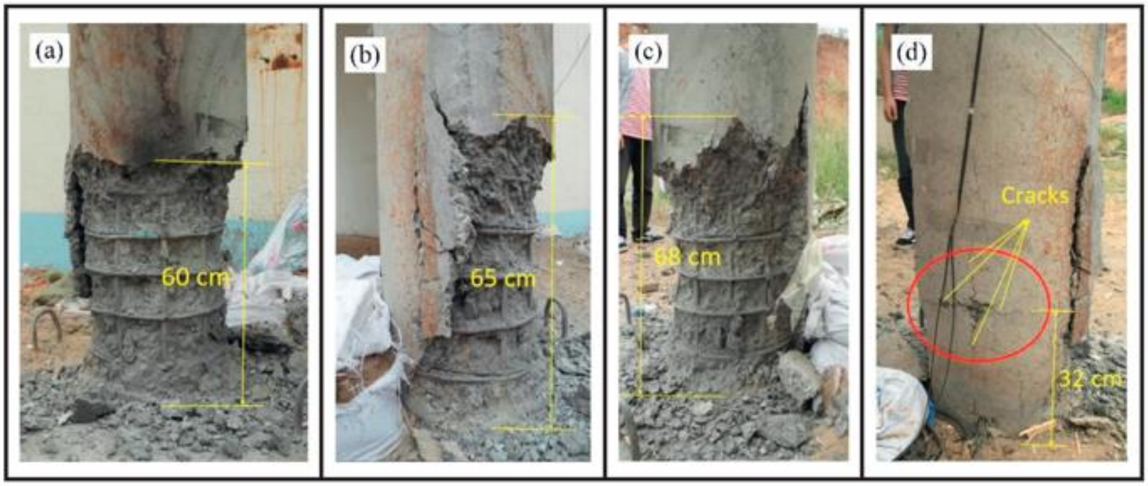

Figure 3. 12 Circular column after test (Yuan et al. 2017)

This observation suggests that the impact of the blast predominantly affected the exposed surfaces of the column, leading to more pronounced concrete damage on the front and side surfaces. The varying levels of damage on different surfaces provide valuable insights into the response of concrete structures under extreme compressive blast loads, allowing for a comprehensive understanding of the failure mechanisms and vulnerabilities associated with different regions of the column.

Figure 3.13 depicts the numerical simulation outcomes of the circular column specimen subjected to a contact explosion with a 1kg TNT charge from Yuan et al. in 2017 [11] using ALE method.

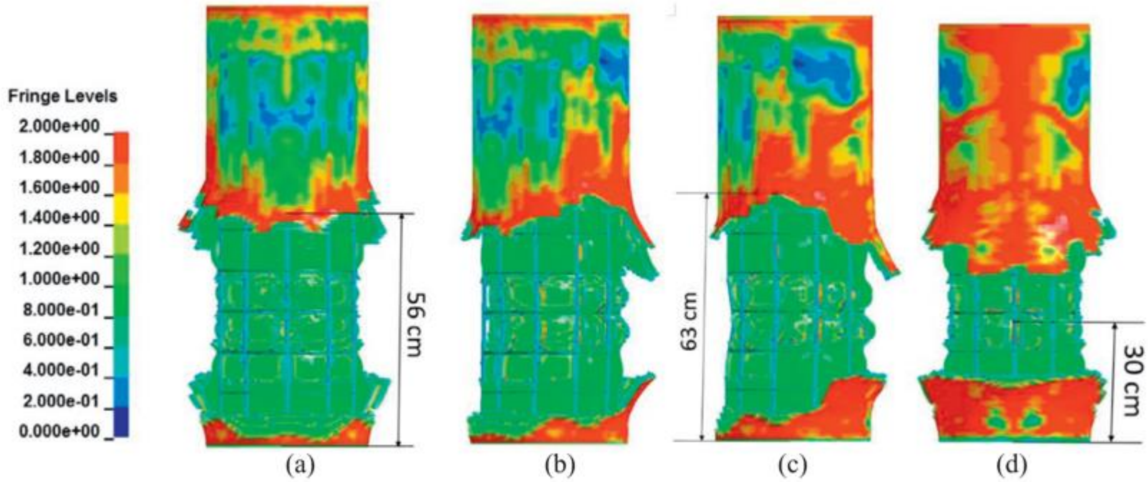

Figure 3. 13 Simulation results (Yuan et. al. 2017)

In Figure 3.13 (a), the vertical extent of damage on the front surface of the specimen is quantified, revealing a measured value of 56 cm. This finding denotes the region where substantial structural deformation and material failure occurred due to the explosive force. Notably, a slight deviation is observed when comparing these simulation results with the corresponding experimental observations presented in Figure 3.12 (a). The experimental investigation yielded a front surface damage height of 60 cm, indicating a minor disparity between the simulated and experimental outcomes. The destructive effects of the explosion are evident in the observed damage patterns on the circular column specimen. As shown in Figure 3.13 (b) & (c), below a height of 63 cm, all of the side cover concrete has been completely destroyed, indicating a significant loss of structural integrity in this region, which signifies the severe impact and propagation of the explosion forces. Furthermore, the damage height on the two side surfaces appears to be slightly greater than that on the front surface. These findings align with the experimental results obtained by Yuan et. al. 2017 [11].

Figure 3.14 presents the results obtained from the numerical model simulation developed in this study. In Figure 3.14 (a), two significant failure zones can be observed on the front face of the specimen, spanning along the height of the column. The measured damage heights in these zones are 64 cm and 58 cm, respectively. By taking the average of these measurements, an overall damage height of 61 cm is determined.

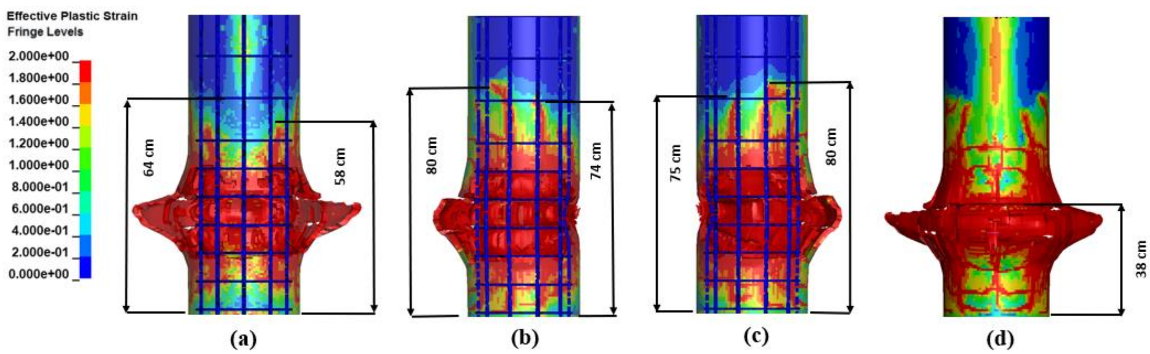

Figure 3. 14 Numerical results (this study)

It is worth noting that this overall damage height is slightly larger than the numerical simulation results that yielded a value of 56 cm. The presence of extensive failure zones along the column height indicates the severity of the structural damage caused by the contact explosion. The high-intensity forces generated by the TNT charge have led to localized material failure. Figure 3.14 (b) and (c), reveal an average damage height of 77 cm on both the left and right side surfaces of the column specimen. In the Yuan et al. in 2017 [11] study, their experimental results reported a measured damage height of 68 cm, while their numerical simulation yielded a value of 63 cm for the right side view of the column. When comparing these three datasets, it becomes evident that the numerical model results obtained in this study predicted a slightly larger damage, which is conservative. The simulation in Figure 3.14 (b) and (c) shows and captures the occurrence of core concrete loss and concrete cover spalling on both side faces of the column. Overall, the simulation results from this study demonstrate a reasonable level of agreement with both the experimental and numerical findings reported by Yuan et al. in 2017 [11], pertaining to both the front and side faces of the column.

However, the study conducted by Yuan et al. in 2017 [11] revealed some inconsistencies between the simulation results and experimental observations, particularly regarding the back face of the column specimen. As depicted in Figure 3.13 (d), the simulation results exhibited concrete cover spalling on the back surface, whereas the experimental test showcased only minor concrete spalling accompanied by some cracks, as depicted in Figure 3.12 (d). The disparity between the simulation and experimental results on the back face of the column specimen highlights the limitations or discrepancies in the Yuan’s et. al 2017 [11] numerical model's ability to accurately capture the observed phenomena on the back face of the column. In contrast, the numerical model developed in this study exhibits better agreement with the experimental results reported by Yuan et al. in 2017 [11]. The ability of the numerical model developed in this study to better replicate the observed behavior on the back face of the column is a notable advancement of this study.

Figure 3.15 illustrates the numerical results obtained for a square column specimen, as developed by Yang et al. in 2019 [17] , utilizing the same experimental data from Yuan et al.'s 2017 study but employing the Coupled Lagrangian Eulerian (CLE) method. These simulation results, as shown in Figure 3.15 (a), (b), (c), and (d), are presented here to provide an overview and a qualitative comparison between the studies conducted by Yuan et al. in 2017 [11] and the numerical models presented in this thesis. While Yang et al. (2019) originally replicated Yuan et al.'s experimental models, it's important to note that Yang et al.'s model was introduced in this context not for a direct comparison, but rather as a cross-check reference. The contact detonation initiated a profound three-dimensional (3D) wave propagation phenomenon within the column. Upon the destruction of the concrete on the front surface, the residual blast energy persisted as compressive pressure waves, propagating through the structural medium. When these waves encountered the side concrete surface, they traveled only a minimal distance and exhibited almost negligible wave divergence. Figure 3.16 shows the pressure (Pa.) wave propagation distribution fringe plot captured at 10 milliseconds. The incident compressive wave experienced a transition into a tensile wave upon reflection and subsequently interacted with the compressive wave. As a consequence, the resulting tensile stress surpassed the dynamic tensile strength of the concrete.

Consequently, severe tensile failure of the concrete material was observed on the side concrete surface. The damages on the front and side surface led to a significant dissipation of the blast energy. The rear surface, which corresponds to the longest travel distance for the blast wave, experienced comparatively lower levels of tensile failure. The phenomenon of wave interaction and subsequent tensile stress generation offers important insights into the failure mechanisms of concrete structures subjected to explosive loading.

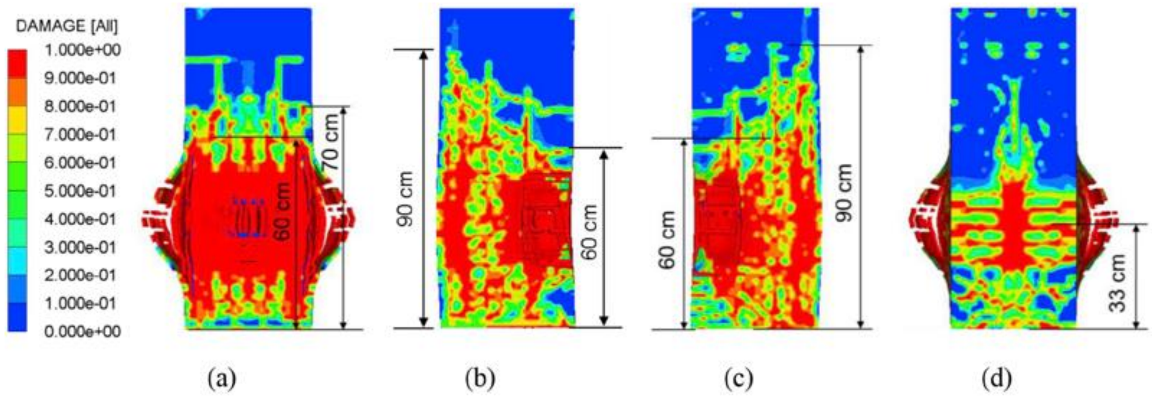

Figure 3. 15 Numerical results for square column based on CLE method (Yang et. al. 2020) [22] (a) front view (b) left side view (c) right side view (d) back view.

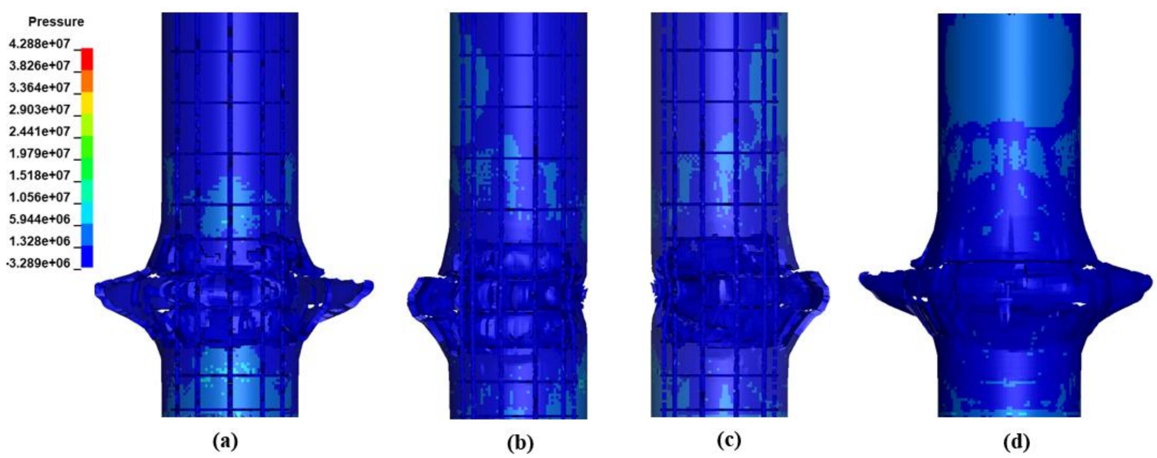

Figure 3. 16 Numerical results of pressure wave propagations at t = 0.01s based on ALE method (this study) (a) front view (b) left side view (c) right side view (d) back view

The following description refers to the verification efforts of the current study against the experimental results of Yuan et al. (2017) [17]. It is important to note that despite the absence of evident cover concrete spalling or detachment, close inspection revealed the presence of extensive cracks on the rear surfaces of the two columns. Unlike the compressive failure observed on the front surface, these cracks are the result of tensile fracture. During the propagation of the blast wave within the column, when the compressive wave interacts with the free surface, it undergoes reflection and transforms into a tensile wave. This phenomenon leads to the development of tensile stresses on the rear surface, contributing to the formation of cracks. Although the visual appearance of the rear surfaces does not exhibit apparent signs of concrete spalling or detachment, the presence of these cracks indicates the occurrence of tensile failure. Figure 3.17 shows the cross-sectional deformation propagations taken at time instants of 2, 6, 8, and 10 milliseconds.

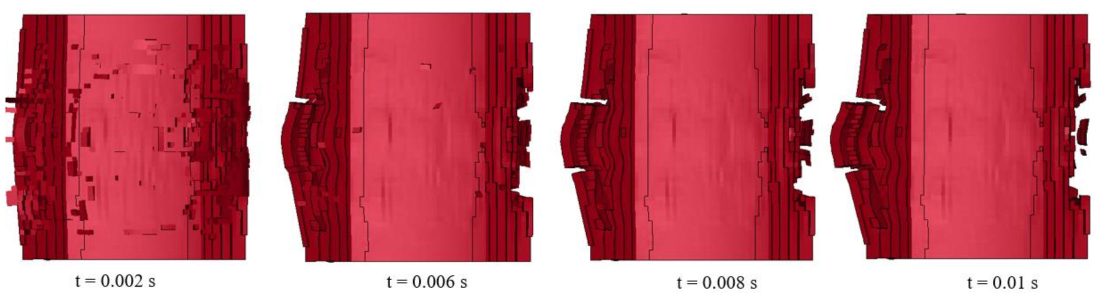

Figure 3. 17 Cross-sectional deformation propagation in time, t (this study).

It is important to consider that concrete spalling occurs when the net tensile stress surpasses the dynamic tensile strength of the material. Analysis of the test results by Yuan et. al. 2017 [11] revealed that the tensile stress resulting from the reflection of stress waves at the rear surface was below the concrete's tensile strength. As a result, no concrete-spalling was observed on the rear surface. Instead, the cracks observed on the rear surface were generated as a consequence of the subsequent flexural response of the column. The dynamic loading induced by the blast wave caused the column to undergo flexural deformation, leading to the development of cracks. These cracks were a result of the tensile stresses experienced by the concrete due to the bending moments induced during the dynamic response.

Figure 3.18 shows numerical results of effective plastic strain wave propagations. When conducting a numerical simulation in LS-DYNA, the effective plastic strain values are typically outputted at discrete time intervals or at specific locations within the model. These values provide information about the extent of plastic deformation that has occurred at those particular points in the material. The unit representation of effective plastic strain in LS-DYNA is dimensionless, as it represents a ratio of the change in shape or deformation to the original dimensions of the material. The effective plastic strain values are often presented as scalar quantities and can range from 0 to higher values depending on the severity of the plastic deformation. A value of 0 indicates no plastic deformation, while higher values indicate increasing levels of plastic strain. For example, the highest value in this study was found to be 2.0 (200%) as shown in Figure 3.18.

Based on the comprehensive comparisons conducted above, significant agreements have been observed between the damage profiles obtained from Yuan et al.'s (2017) [11] experimental data, their numerical simulation results, and the numerical simulation results produced by the model developed in this study. This correspondence between the damage profiles serves as the first validation method, providing strong evidence supporting the accuracy and reliability of the numerical model in this study.

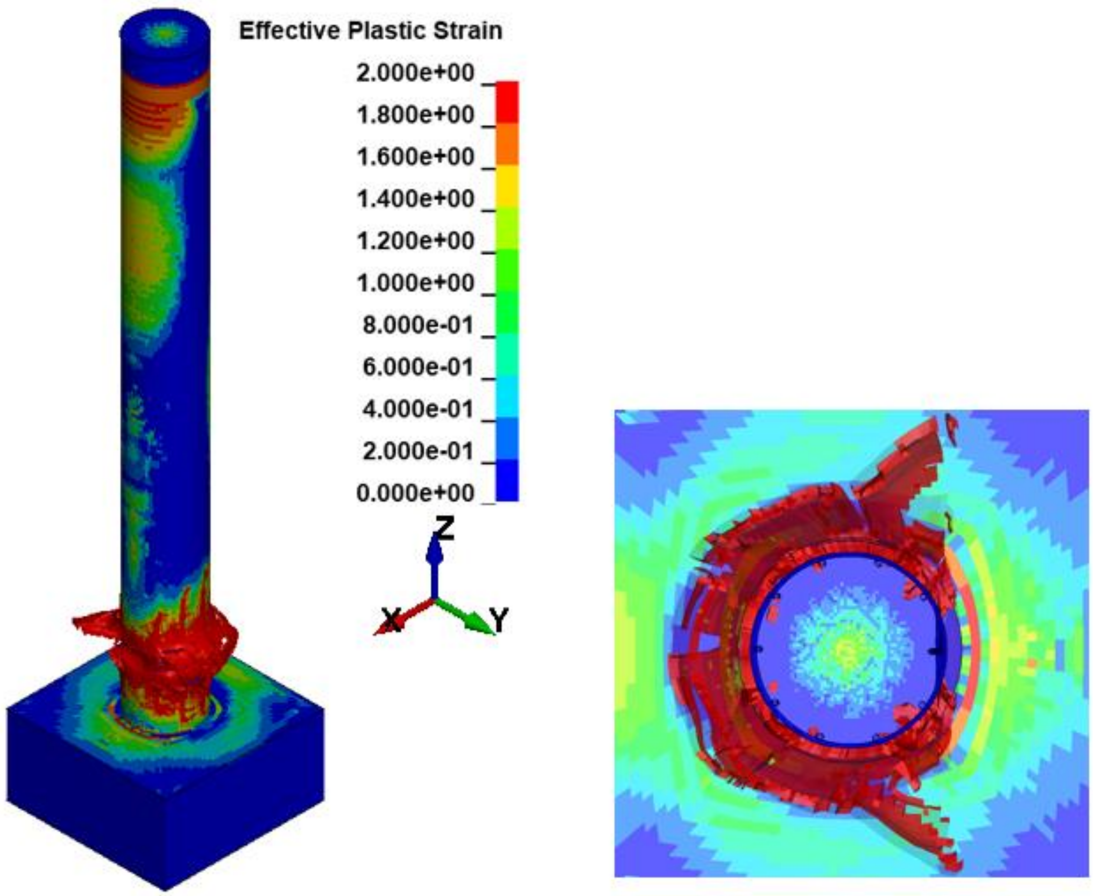

(a) (b)

Figure 3. 18 Numerical results of effective plastic strain wave propagations (a) Isometric view (b) Top view (this study)

3.2.7.2 Comparisons of Acceleration - Time Histories

The time history of lateral accelerations serves as another source of information for understanding the characteristics of the lateral forces exerted on the column and provides valuable insights into their intensity and duration. By analyzing the time history, it is possible to observe the complete temporal evolution of the structural response, encompassing the distinct phases of initiation, peak, and decay of the lateral accelerations.

This comprehensive understanding of the temporal behavior of lateral accelerations enables a detailed assessment of the dynamic response of the column. The initiation phase represents the immediate response of the structure to the contact explosion, indicating the moment when the lateral forces first impact the column. Subsequently, the peak phase highlights the maximum magnitude attained by the lateral accelerations, providing crucial data for assessing the structural integrity and potential damage. Finally, the decay phase illustrates the gradual decrease in the lateral accelerations over time, reflecting the dissipation of the impulsive forces and the subsequent damping of the structural vibrations. This information is vital for designing blast-resistant structures, as it provides insights into the duration and magnitude of the lateral forces acting on the column, thus facilitating the development of appropriate mitigation strategies to enhance structural robustness and ensure the safety of the surrounding environment.

In their experimental setup, Yuan et al. (2017) [11] employed a precise methodology by strategically placing three accelerometers at specific locations along the height of the column specimens. These accelerometer locations were selected at distances of 330 mm, 1750 mm, and 3300 mm from the base of the column to capture the localized response of the specimens as shown in Figure 3.11. The purpose of these accelerometers was to measure the lateral acceleration time history at these locations, thereby providing valuable data for the validation of their numerical models. In alignment with the experimental arrangement, the current study also incorporated the same sensor placement strategy within the numerical model of the column. These positions were replicated as numerical sensors, designated as sensor 1 (at 330 mm), sensor 2 (at 1750 mm), and sensor

3 (at 3300 mm), as depicted in Figure 16 (a) and (b). The localized data obtained from the numerical sensors serves as a reliable metric to evaluate the accuracy and fidelity of the numerical model in capturing the dynamic behavior and response of the column under the contact explosion scenario.

Figures 3.19 present a comparative analysis between the experimental and numerical results of the acceleration time history for the circular column, as investigated by Yuan et al. (2017) [11]. They found some discrepancies between their experimental and numerical results. Figure 3.20 presents the numerical simulation results obtained from the current study, allowing for a direct comparison with the experimental measurements conducted by Yuan et al. (2017) [11]. Examining Figures (3.19) and (3.20), it is evident that there is a good agreement between the peak values and the global variation trend of the acceleration data derived from the experimental measurements and the current numerical model. This comparison serves as a second validation confirming the reliability of the numerical model in this thesis.

For example, Yuan et al. reported a peak acceleration value of 12,769 m/s^2 based on their experimental findings, while their numerical simulation yielded a peak positive acceleration of 13,788 m/s^2, as shown in Figure 3.19. In this study, the numerical model from Sensor 3 produced a peak acceleration of 12, 203 m/s^2. The minor variations in peak acceleration values reported above can be attributed to several factors, such as differences in experimental conditions, material properties, and modeling assumptions. Overall, the acceleration history from the current study is in good agreement with Yuan et al.'s experimental data.

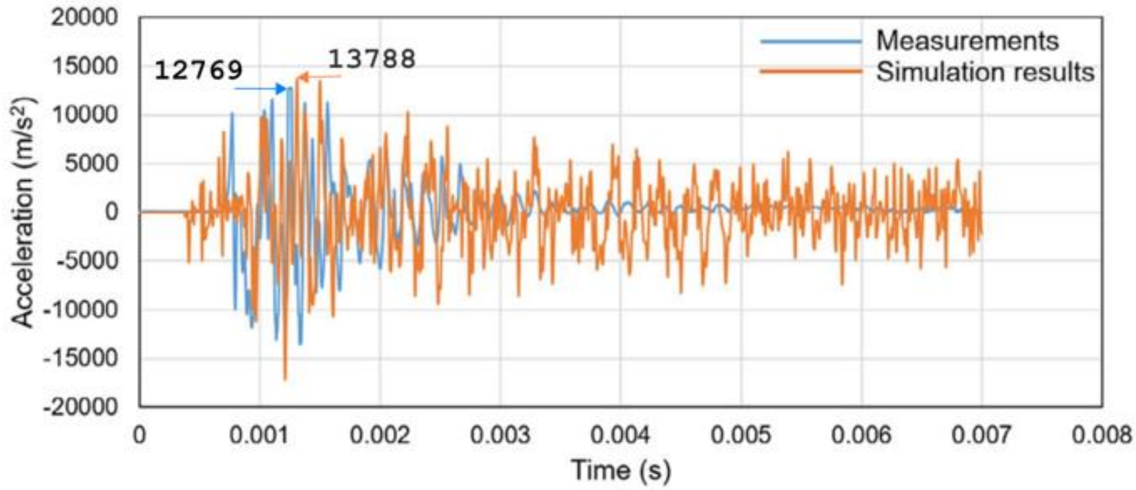

Figure 3. 19 Acceleration-time history (Yuan et. al. 2017)

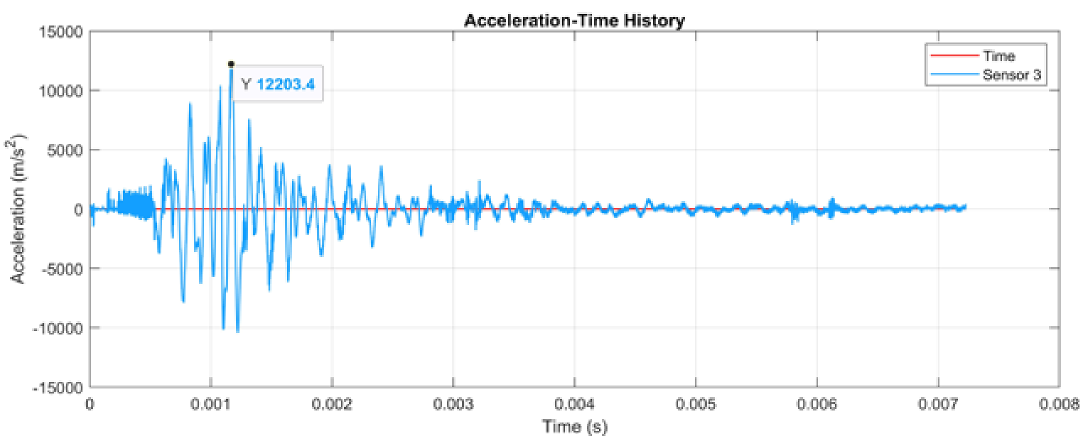

Figure 3. 20 Numerical results (this study)

These findings highlight the successful implementation of the numerical model, which effectively reproduces the peak acceleration values and captures the global variation trend observed in the experimental measurements. This agreement between the numerical and experimental results lends confidence to the predictive capability of the numerical model, reinforcing its utility in simulating and analyzing the dynamic response of structures subjected to contact explosions. This observation signifies the enhanced capability of the numerical model developed in this study to accurately capture the experimental responses. It suggests that the numerical model demonstrates better results in terms of reproducing the acceleration time history when compared to the numerical models employed by Yuan et al. 2017 [11]

In conclusion, the observed agreement between the numerical simulation results and Yuan et al.'s experimental data, with only a minor discrepancy, demonstrates the accuracy and robustness of the numerical model developed in this study. This section serves as a second strong validation of the numerical model, solidifying its capacity to provide reliable predictions and insights into the dynamic behavior of structures subjected to contact explosion events.

3.2.7.3 Comparisons of Displacement - Time Histories

The displacement-time history of a circular column during a contact explosion provides crucial information about its dynamic response. It reveals the temporal evolution of lateral displacement, offering insights into the structural behavior during different phases of the explosion.

By analyzing the displacement-time history, it is possible to determine the maximum lateral displacement and its corresponding time, aiding in the assessment of structural integrity and blast-resistant design effectiveness. The displacement time - history also highlights trends, oscillations, and vibrations, providing further understanding of the column's dynamic characteristics. The study conducted by Yuan et al. in 2017 [11] did not include the presentation of a displacement-time history. In contrast, Yang et al. in 2019

[17] undertook the task of calibrating and constructing a numerical model based on the field blast test data provided by Yuan et al. 2017 and employing the CLE (Coupled Lagrangian Eulerian) method. This numerical model specifically focused on a square reinforced concrete (RC) column. The objective of Yang et al.'s [17]work was to replicate the dynamic response and damage patterns exhibited by the RC column when subjected to contact blast loads.

In order to accomplish this, Yang et al. 2019 [17] extensively compared and validated their numerical model against the experimental results documented by Yuan et al. in 2017. The intention behind this comparison and verification was to assess the accuracy and reliability of the numerical model by evaluating its correspondence with the actual recorded outcomes from the experiments conducted by Yuan et al. 2017 [11]. The lack of displacement-time history in the study conducted by Yuan et al. in 2017 posed a challenge for the verification and validation processes of the present study. In spite of notable differences between Yang et al.'s model in 2019 and the current study, including variations in numerical methods employed (ALE vs CLE), and the location from which nodal data was obtained (Sensor 2 vs Target 1) Figure (3.21), a comparison of x-displacement-time histories was still made.

The two displacement-time histories exhibited good agreement, as shown in Figures (3.21) and (3.22). This comparison offered an additional means of verifying the numerical model employed in the current study.

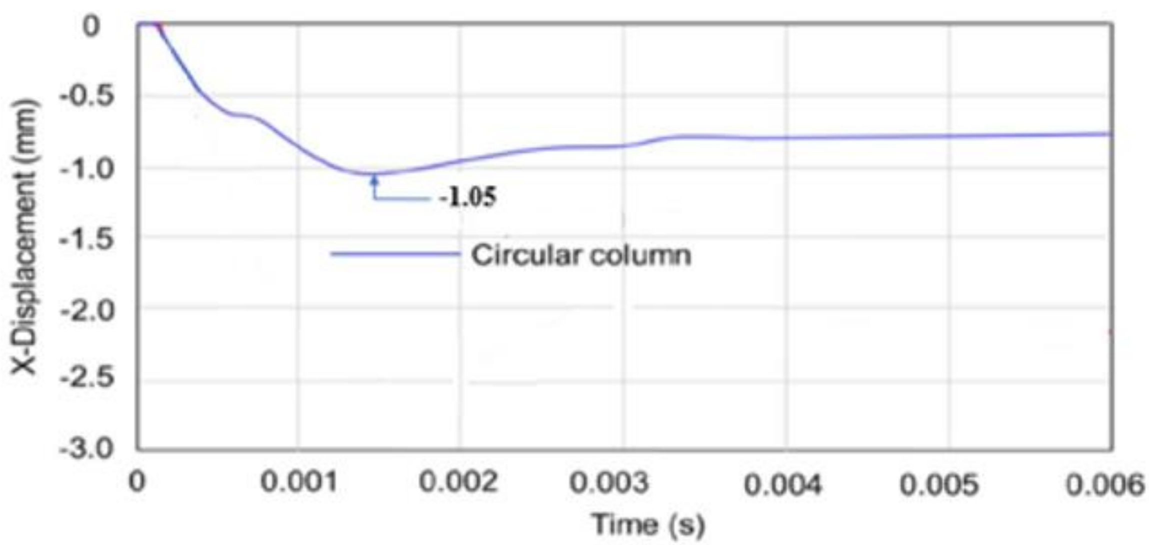

Figure 3. 21 Displacement time history (Yang et. al. 2019)

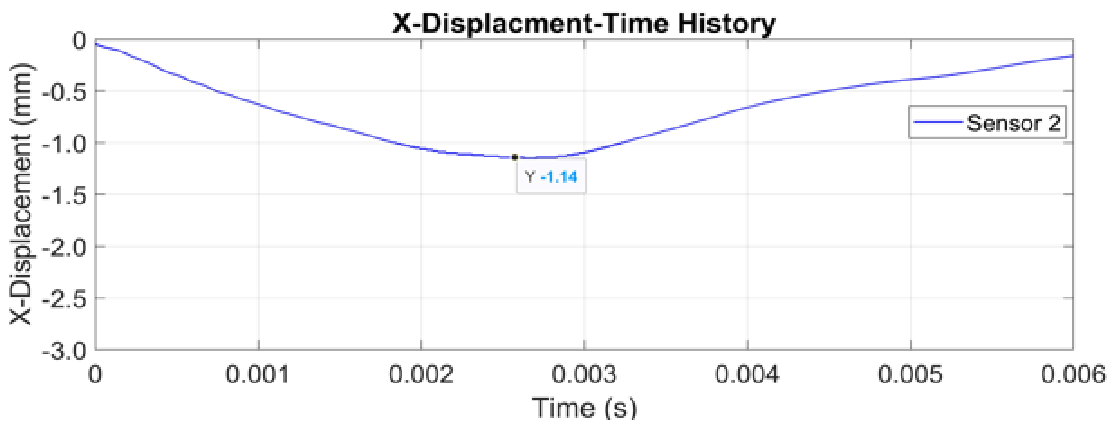

Figure 3. 22 Displacement time history (this study)

3.2.7.4 Energy Dissipation in Shock Waves

As the shock wave undergoes expansion, the prevailing pressures experience a rapid decline proportional to the cube of the distance. This decrease is attributable to geometric divergence, wherein the wavefront expands and spreads out. Additionally, the dissipation of energy through the process of heating the surrounding air contributes to the reduction in pressures. Furthermore, the pressures exhibit an exponential decay over time, signifying their diminishing nature. The lifespan of these pressures is exceedingly brief, typically measured in milliseconds or even thousandths of a second (FEMA, 1989) [53] .

The energy carried by the shock wave at a specific distance from its source serves as a quantitative measure of the potential effectiveness or destructive capability that the shock wave can impart. Cole 1948 [1] stated that the total of energy radiated by the source during the initial stages of an explosion exerts control over the extent to which the reserve of chemical energy persists, facilitating subsequent movement of the gas products and surrounding elements. Ultimately, the entire energy content radiated within the shock wave undergoes dissipation through dissipative processes as the wave propagates outward, resulting in its conversion into heat energy. The energy behind a shock front may manifest in a variety of ways, not only the work done on a surface stationary in the fluid. The rate of energy flow over the surface of a given area, or energy flex density, is another measurement that may sometimes be helpful.

According to Sadwin et al. (2017) [54], in the context of an air blast explosion, the energy flux, denoted as E, can be quantified using the following basic equation (Equation 3.16). This equation serves as the basis for determining the rate at which energy is transferred through a given region:

Equation 3. 15

$$E=\int(\rho U)^{-1}P_s^2dt$$

Where ρ = local air density [Kg/m^3], U = local wave velocity [m/s], Ps = overpressure shock wave [Kg/m^2], t = time [s]. The energy flux, E, has units of (Kg-m/m^2).

Figure 3.23 shows the graphical representation of the numerical results of kinetic, internal, and total energy of this model. In the graph, the blue curve shows the kinetic energy wave propagation, representing the energy associated with the movement and velocity of the structural elements in the column. This curve showcases the time history variations in the kinetic energy levels as the blast wave travels through the column, indicating the distribution of energy across different spatial locations. Similarly, the green curve shows the internal energy wave propagation. This curve illustrates the changes in internal energy levels within the column as the blast wave propagates. It provides insights into the thermal and elastic effects induced by the explosion and shows the distribution of internal energy throughout the column.

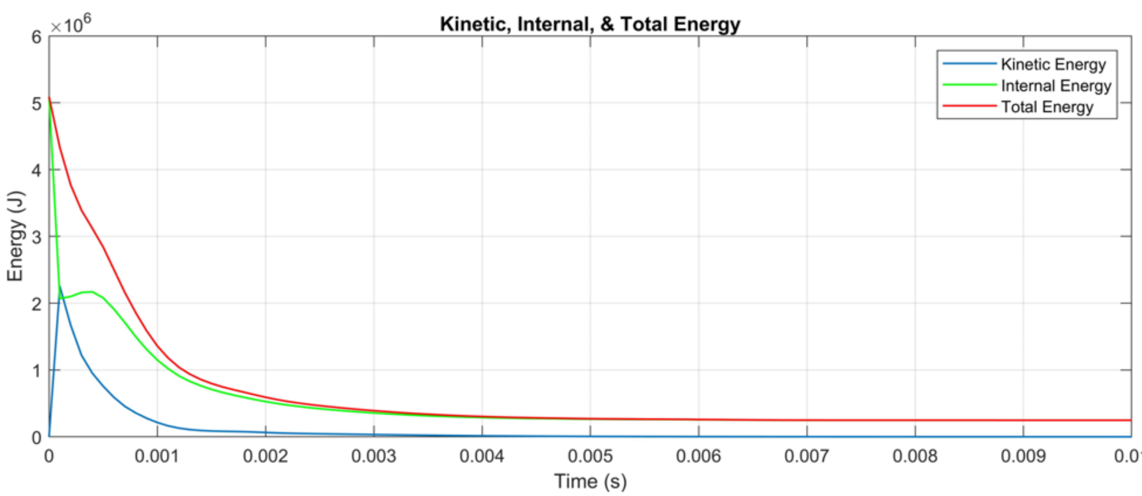

Figure 3. 23 Numerical results (this study)

The red curve shows total energy wave propagation. This curve represents the sum of the kinetic and internal energies at each point in the column. It offers a holistic view of the overall energy distribution and transfer within the structure during the blast event.

By analyzing the variations in the total energy curve, it is possible to identify critical regions of energy concentration and evaluate the potential for structural damage or failure. Moreover, the graph presented in Figure 3.23 demonstrates a remarkable agreement between the simulation results and the theoretical concepts proposed by Cole in 1948 [1]. As predicted by Cole, the shock waves propagate outward, leading to a rapid decrease in the energy carried by the waves. Consequently, there is a significant reduction in energy density in close proximity to the explosive charge. This phenomenon is accurately captured by the simulation results, as depicted in Figure 3.23, where three distinct curves representing kinetic, internal, and total energies exhibit an exponential decay in time from the source charge.

Specifically, the graphical representations of the kinetic and total energy curves in Figure 3.28 exhibit a qualitative resemblance to a typical pressure-time history. This correspondence arises from the fact that the dissipation of energy in a shock wave can be derived through direct integration of the pressure-time history (equation 3.16), which typically follows an exponential decay pattern.

These findings align with the theoretical explanations outlined in Cole's book from 1948 [1]. Notably, the congruence between the simulation results and the theoretical concepts serves as another additional validation source, affirming the reliability of the numerical model developed in this study.

CHAPTER FOUR

4.1 Introduction

This chapter presents modeling and validation of underwater explosion responses of RC columns. In this study, the process of calibrating the numerical model simulation of UNDEX is conducted by employing experimental tests conducted by Zhuang et al. (2020) [25]. The experiment was conducted within a cylindrical water tank which possessed a diameter of 10.0 m, and a water depth of 2.25 m. A buffer sand cushion, measuring 0.5 m in thickness, was uniformly distributed across the bottom of the tank. The experimental setup employed a similarity ratio scale of 1:8 in relation to the actual geometry of the RC column (Zhuang et al. 2020) [25] .

4.2 Numerical Modeling of RC Column subjected to UNDEX Using LS-DYNA

This section addresses various aspects such as meshing and experimental setup for model calibration, boundary conditions, material models, ALE coupling, erosion algorithm, simulation procedures, and output controls.

4.2.1 Geometry, Meshing and Experimental Setup for Model Calibration

Zhuang et al. (2020) [25] presented a diagrammatic representation of the experimental model utilized for investigating the response of a single RC (Reinforced Concrete) column subjected to UNDEX, as shown in Figure (4.1). The authors proposed two distinct experimental models: the circular RC column (referred to as Model-1) shown in Figure 4.30 (a), and the steel pile (termed as Model-2) shown in Figure 4.30 (b).

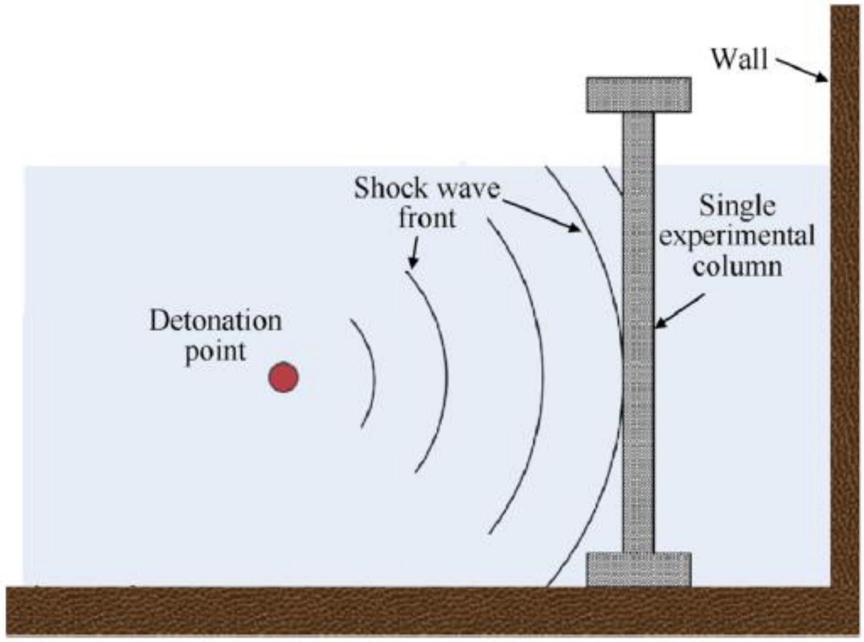

Figure 4. 1 The scaled-down experiment model of RC column, Zhuang et. al. (2020)

It was anticipated that the circular RC column would undergo plastic deformation in response to the explosive loading, whereas the steel pile was designed to remain employed to the pressure magnitude using sensors installed on the surface of the steel pile. The height of the RC column was 2.70 m, while the diameter was 0.1 m. The two ends of the column had a thickness of 0.1 m and a larger diameter of 0.3 m. For longitudinal reinforcement, a total of 8 HRB335 ribbed bars, each with a diameter of 6.0 mm, were included, as shown in Figure (4.2). The RC concrete utilized in the experiment underwent testing after 28 days with a compressive strength of approximately 52.0 MPa (Zhuang et al., 2020) [25].

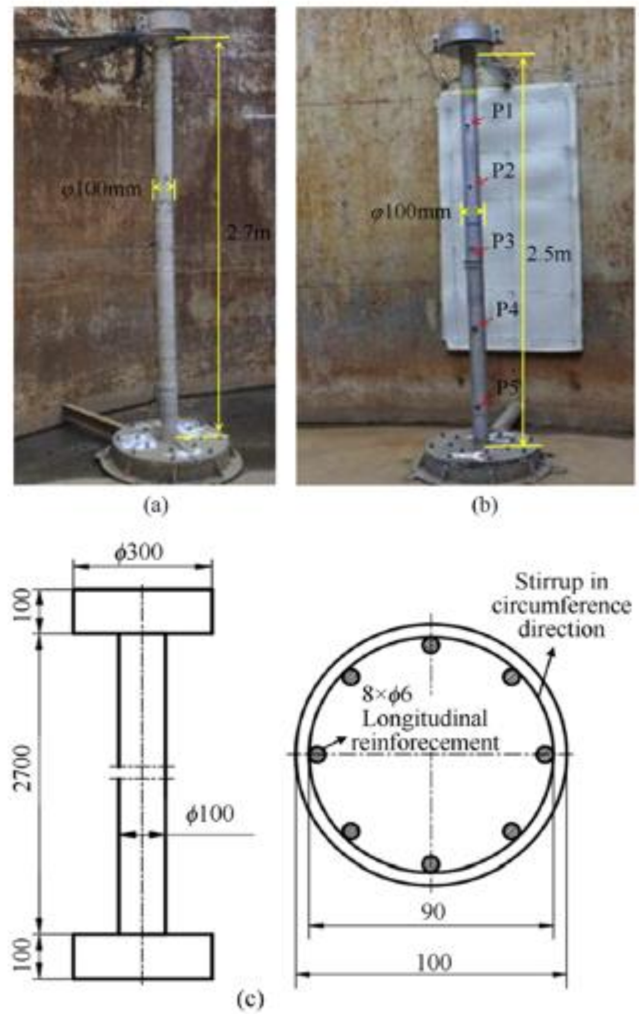

Figure 4. 2 Geometry and details used in experimental set up (Zhuang et. al. 2020).

A comprehensive assessment of various experimental conditions was conducted through the utilization of specialized sensors, including pressure sensors, strain sensors, displacement sensors, and acceleration sensors. Specifically, ten pressure sensors were strategically positioned on each steel pipe model. These sensors were arranged such that five sensors (labeled as P1-P5) were placed on the windward side, while the remaining five sensors (labeled as P6-P10) were located on the leeward side. The pressure sensors were carefully situated within the interior of the steel pipe, ensuring that their surfaces were precisely aligned with the external surface of the steel pipe. A visual representation of the sensor configuration can be observed in Figure (4.3). In addition to the pressure sensors, Zhuang et al. (2020) incorporated displacement and acceleration sensors on the outer surface of the RC column. This arrangement enabled the measurement of the dynamic response and deformation characteristics exhibited by the RC column during the experimental procedure.

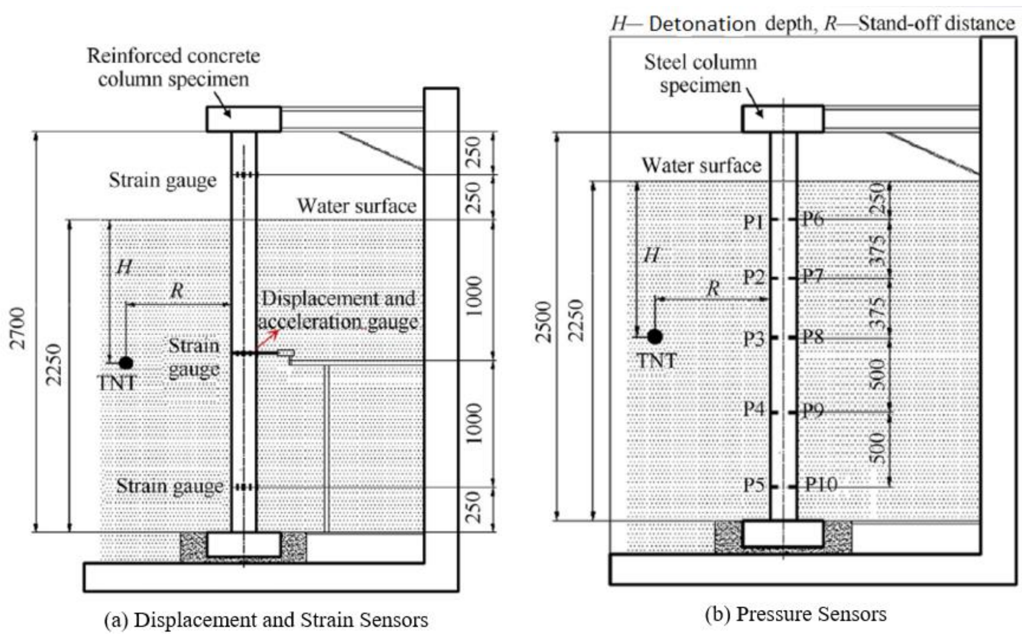

Figure 4. 3 Configuration of sensors in experimental set up, units: mm. (Zhuang et. al. 2020)

The explosive charge was TNT, and it was positioned at a specific depth below the water level. This precise placement was achieved using a suspension device designed for this purpose (Zhuang et al. 2020) [25]. In the experimental setup conducted by Zhuang et al. (2020), as shown in Figure (4.3), a range of diverse experimental conditions were examined to investigate the effects of various factors. These factors encompassed the explosive quantity (W), the stand-off distance (R), and the detonation depth (H). By systematically varying these parameters, the study aimed to explore and comprehend the distinct influences and impacts associated with each factor on the overall experimental outcomes.

In this study, an UNDEX model was created utilizing the LS-DYNA ALE method. The geometry and meshing of various components were generated in a similar manner as the air blast study and are summarized in Table 4.1 for reference.

Table 4. 1 Details of dimensions and meshing's employed for UNDEX modeling.

Material Type	Dimensions (mm)	Element Type	Mesh size (mm)	No of Elements
Column	H= 2700 mm; D= 100 mm	Lagrange Solid	Fine=8 mm and 25 mm; Coarse = 62.5 mm	22,320
Foundation	W=300 mm; L=300 mm; H=100 mm		Uniform = 25 mm	
Longitudinal Rebar	H=2840 mm; 8-D6	Beam	Uniform = 15 mm	1,456
Stirrups	D=90 mm; 12-D8			288
Water	D=10,000 mm; H=2350 mm	ALE Solid	Fine =12.5 mm & 25 mm; Coarse = 100 mm	1,112,532
Air	D=10,000 mm; H=750 mm	ALE Solid	Uniform = 100 mm	244,164
			Total	**1,380,760**

Figure 4.4 (a) and (b) show the geometry and meshing for concrete column solid and long. rebars & stirrups. Whereas Figure 4.5(a) shows water model geometry and RC column seen above the free water surface. In the simulation model, Figure 4.5(b) illustrates the meshing employed for the ALE water and air domains. To offer a cross-sectional view

and emphasize the respective dimensions of the column, water, and air, Figure 4.6 (b) is provided. This figure provides a comprehensive understanding of the geometric configuration of the three components. The TNT was modeled in LS-DYNA using keyword *INITIAL_VOLUME_FRACTION_GEOMETRY. This specific keyword plays a pivotal role in accurately defining the placement and distribution of TNT material within the water mesh. To establish the initial distribution of water and TNT ALE materials, the *INITIAL_VOLUME_FRACTION_GEOMETRY card employs the ALE_MULTI_MATERIAL_GROUP (AMMG) parameter.

This parameter allows for the prescription of volume fractions for the initially mixed cells. It ensures that only materials belonging to the same material group (AMMG) can join or mix together within the simulation, maintaining a consistent and physically realistic representation of the system. The water mesh is established using the FMSID option, which designates a background ALE (fluid) mesh SID for initialization and filling with various ALE Multi-Material Groups (AMMGs). The BAMMG parameter specifies the background fluid group ID or ALE Multi-Material group ID (AMMGID) that initially occupies the ALE mesh region defined by FMSID, representing the water mesh region.

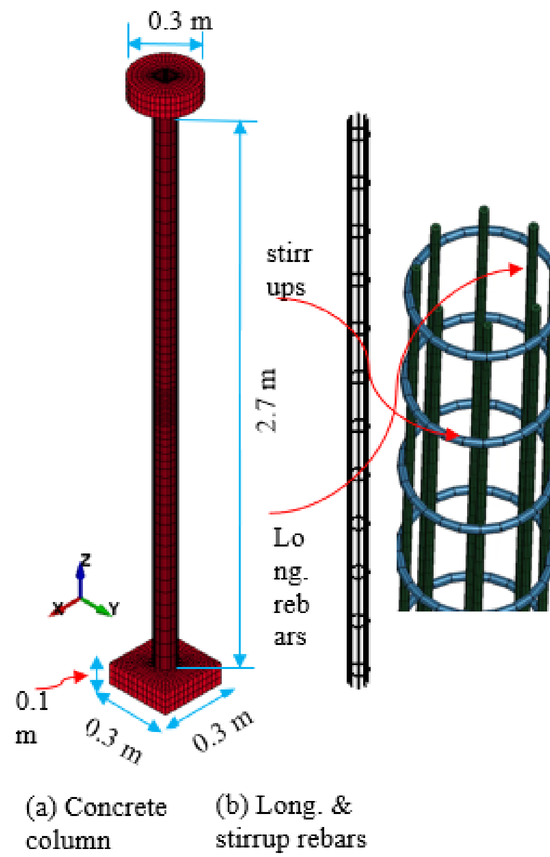

Figure 4. 4 Geometry & meshing (a) concrete column (b) long. rebars and stirrups.

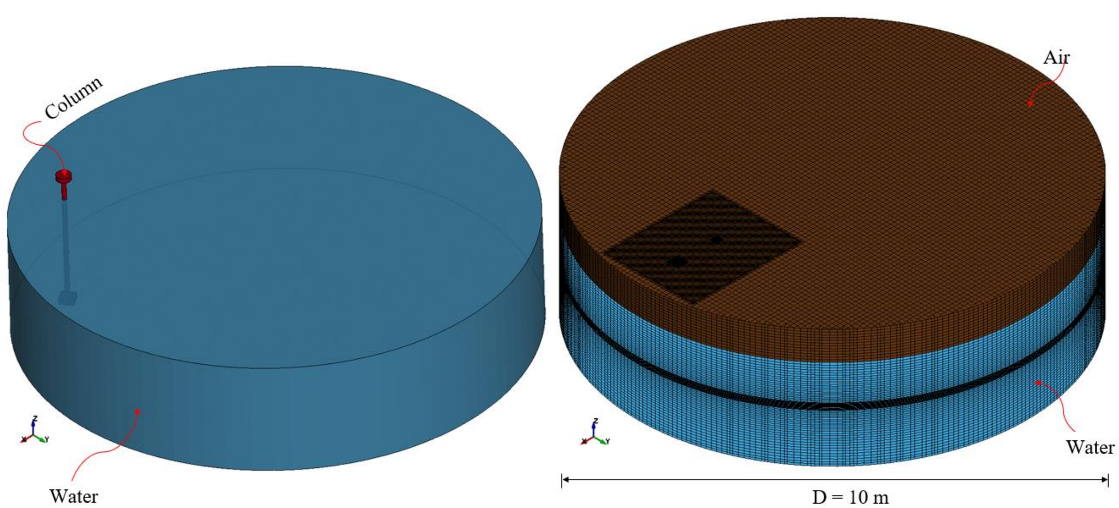

Figure 4. 5 (a) Column and Water; (b) ALE solid water and Air meshing

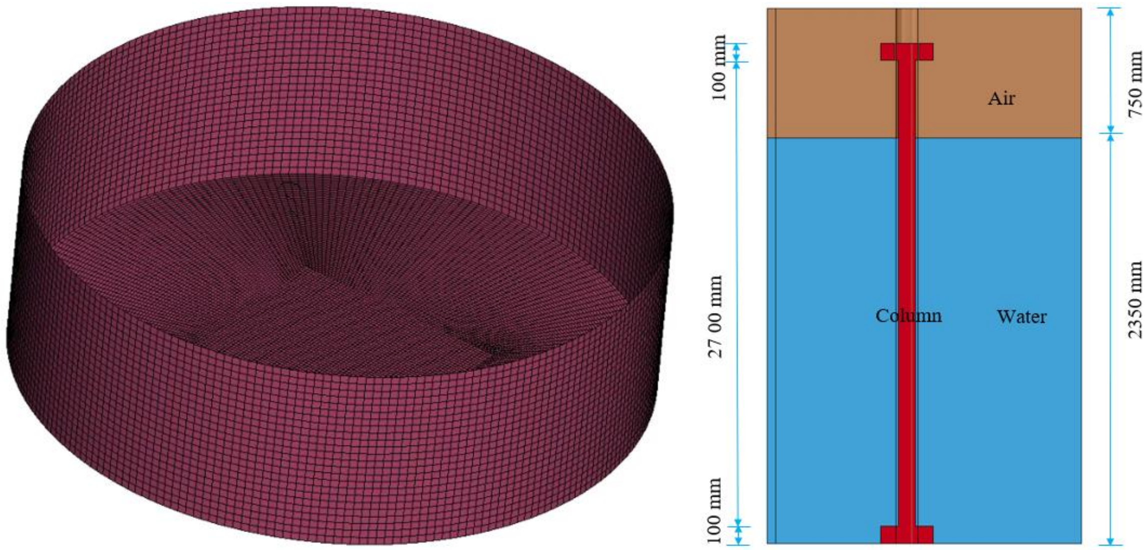

Figure 4. 6 (a) Water tank (b) Cross sectional view of column, water, & air.

To define the “container” geometry within which the AMMG will fill up, the CONTTYP option is employed. This option determines the container geometry type, which represents the Lagrangian surface boundary or shell structure. In this study, the EQ.6 option is chosen, indicating that the container geometry is defined by a sphere with a center point and a specified radius. The input data for the TNT includes a sphere radius of 0.0489333 m, and a density of 1630 kg/m^3, and with coordinates of x = 1.0 m & z =1.25 m (from bottom of the column, or 1.0 m from water surface) which is also a corresponding location of P3 in the Zhuang et. al. experiment, as illustrated in Figures (4.7) & (4.3(b)). The FAMMG parameter is utilized to designate the fluid group ID or ALE Multi-Material group ID (AMMGID) responsible for filling the interior or exterior space defined by the container. The order of AMMGIDs is determined by their listing under the *ALE_MULTI-

MATERIAL_GROUP card. In this numerical model development process, the MULTI-MATERIAL_GROUP ID = 3 is assigned to represent the TNT material.

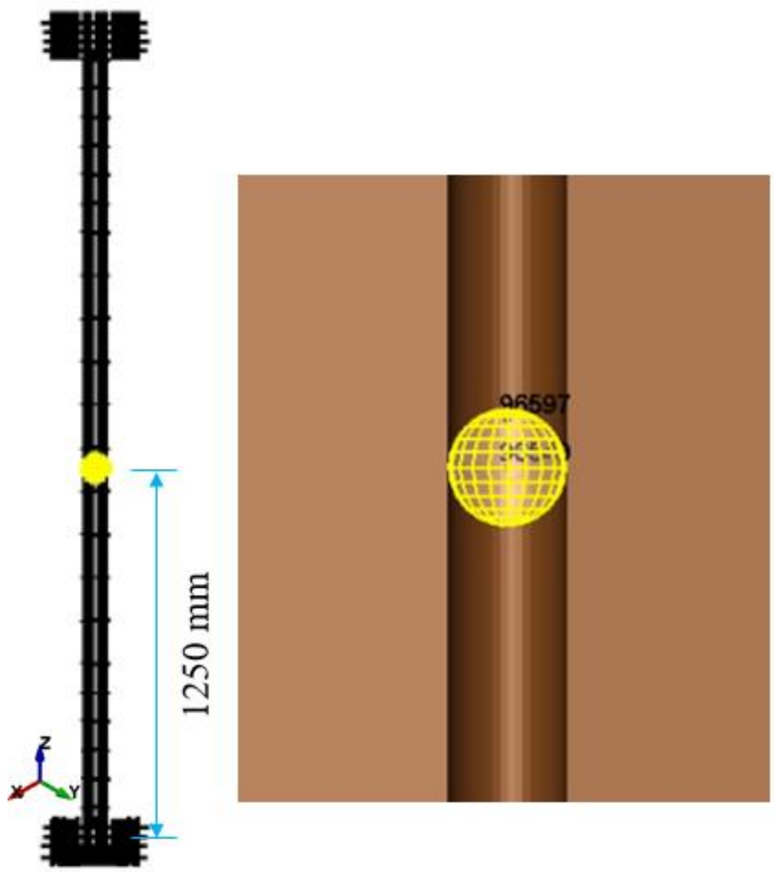

Figure 4.7 TNT location in column and water, x = 1.0 m, z =1.25 m.

4.2.2 Boundary Conditions

The column was fixed to the top and bottom using *BOUNDARY_SPC_SET keyword. Specifically, for the tank bottom, constraints have been imposed to restrict translation along the local x, y, and z axes, while no rotational constraints have been defined around the local x, y, and z axes. Concerning the tank wall, the boundary conditions dictate that there should be no translation in the local x and y directions, and the wall is allowed to freely rotate in all directions, as shown in Figure (4.8).

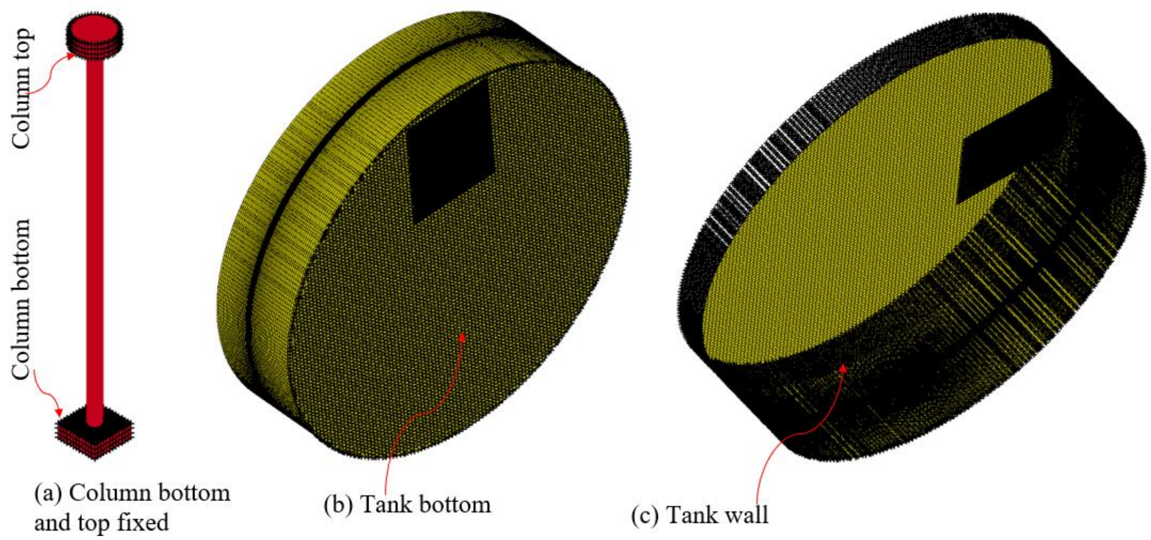

Figure 4. 8 Boundary conditions in UNDEX modeling.

4.2.3 Material Models Employed in LS-DYNA

Similar to the air blast model of section 3.2, the UNDEX simulation in this study also employs the MAT_72_REL3 material model. The average cubic compressive concrete strength is set to 52 MPa, a uniaxial tensile strength of 4.68 MPa, a density of 2300 kg/m^3, and a Poisson's ratio of 0.2 based on Zhuang et al.'s experiments. To simulate the behavior of longitudinal reinforcement bars and stirrups in reinforced concrete (RC) elements, the MAT_PIECEWISE_LINEAR_PLASTICITY material model (MAT_024) is employed in this study. It was chosen for its precision and its ability to account for strain rate effects, which play a critical role in dynamic loading scenarios. Moreover, the MAT_024 model has also been demonstrated to effectively reproduce peak acceleration values and damage profiles in the validated numerical model developed in the preceding sections (3.2.6 & 3.2.7) of this thesis. Table 4.2 shows the materials test derived from the experiments.

The material model *MAT_NULL (MAT_009) is employed to accurately represent both water and air in the simulation. The *MAT_NULL material model utilizes a linear polynomial Equation of State (EOS) and is commonly used to model gases and liquids. Within this material model, the deviatoric stresses are purely viscous, and the viscosity is assumed to be constant. It is important to note that this material model requires an equation of state to define the pressure behavior.

Table 4. 2 Input parameters for the steel reinforcement model, (Zhuang et. al. 2020)

Material Property	Magnitude
Mass density	7850 kg/m^3
Young's Modulus	2.00E+11 Pa
Yield Stress for rebars	350E+6 Pa
Tangent modulus	1.8E+9 Pa
Poisson's ratio	0.3

Equation of State EOS_GRUNEISEN material model, which is specifically designed to simulate materials subjected to high-energy dynamic loading conditions, is used to model EOS for water in the current study. This model employs a Gruneisen equation of state to describe the water's behavior under compression. This equation relates the pressure, volume, and internal energy of water. The Gruneisen coefficient, a material-specific parameter, plays a vital role in determining the response of the material to shock waves. It captures the relationship between pressure and volume changes induced by dynamic loading. A mass density of 1000 kg/m³ and a viscosity coefficient (MU) of 8.900e-04 are assigned to the water material. For air, a mass density of 1.293 kg/m³ is utilized. In both cases, the cutoff pressure is set to the dilatation pressure limits less or equal to zero, which ensures that the pressure values do not exceed the specified limits.

The TNT charge was simulated using the *MAT_HIGH_EXPLOSIVE_BURN material model. To capture the intricate behavior of TNT, the JWL EOS was specifically employed. The JWL EOS is tailored to model TNT and provides a comprehensive understanding of the dynamic relationship between pressure and relative volume considering the initial energy per initial volume. The specific input parameters include 0.80 kg TNT, a mass density (R0) of 1630 kg/m³, a detonation velocity (D) of 6930 m/s, and a Chapman-Jouguet pressure (PCJ) of 21 GPa.

4.2.4 ALE Coupling

In LS-DYNA, the fluid-structure interaction (FSI) problem, such as the one considered in this study, requires the establishment of interaction between the Lagrangian and Arbitrary Lagrangian-Eulerian (ALE) meshes. This interaction is accomplished through the utilization of a coupling algorithm using the *CONSTRAINED_LAGRANGE_IN_SOLID keyword. To facilitate the tracking of interfaces among multiple fluid materials, the *ALE_MULTI_MATERIAL_GROUP

(AMMG) card is employed. This defines the appropriate material grouping for the treatment of multi-material elements and interface tracking. It ensures that the interactions between different fluid materials are accurately accounted for in the simulation.

In the ALE coupling approach, two methods are commonly utilized: the constrained-based method and the penalty-based method. In the constrained-based method, the velocities of ALE materials at the coupling point of the Lagrangian mesh are enforced to be the same. On the other hand, the penalty-based method penalizes any violation of this constraint by applying a penalty force. The magnitude of the penalty force is proportional to the degree of violation, such as the depth of penetration. In this study, both methods have been employed. The coupling between ALE and Lagrangian meshes is implemented using the penalty method. On the other hand, the coupling between rebars and concrete is defined using the constrained-based method, ensuring that the velocities of the two materials at the coupling point remain equal.

For this simulation study, the ALE solid elements/materials include water, air, and TNT, while concrete and rebars are formulated as Lagrangian beam elements/materials.
Additionally, the water tank is modeled using shell elements. The coupling between the ALE and Lagrange meshes has been successfully achieved using the *CONSTRAINED_LAGRANGE_IN_SOLID keyword, employing the following option definitions: -For the ALE and Lagrange coupling (Couple ID 1), the Slave Part ID is set to Concrete, indicating that the concrete material is the slave in the coupling process. The MASTER is defined as the ALE Part Set, representing the ALE mesh. The coupling points are distributed over each coupled Lagrangian surface segment, with a total of three

coupling points specified by NQUAD = 3. The coupling type is denoted by CTYPE = 5, which signifies a penalty coupling approach that permits erosion in the Lagrangian entities. The Penalty factor, PFAC, is set to 0.1, determining the strength of the penalty force applied in case of violation. Lastly, ILEAK is set to 0, indicating that no leakage control is implemented in this coupling scheme.

Similarly, the coupling between the rebars and concrete is implemented using the following option definitions for Couple ID 2. The Slave Part ID is specified as rebar, designating the rebars as the slave component. The MASTER is set to the Part ID representing the concrete material. The number of coupling points, NQUAD, is set to 0, allowing it to default to a value of 2. The coupling type, CTYPE, is defined as 2, representing a constrained acceleration and velocity approach, which is the default behavior. The Penalty factor, PFAC, is set to 0.1, determining the strength of the penalty force applied in case of violation. Lastly, ILEAK is set to 0, indicating that no leakage control is applied in this particular coupling configuration.

Other LS-DYNA modeling options and keywords, including hourglass, simulation controls, and output/database controls, were utilized by following similar steps and procedure used in the air blast simulation.

4.3 Validation of Numerical Model for UNDEX Responses of RC Column

Following the same approach used in the air blast model, the verification and validation of the UNDEX model was compared to experimental results presented by Zhuang et al. in 2020 [25].

4.3.1 Comparisons of Displacement Time Histories

Zhuang et al. (2020) [25] conducted 24 tests varying explosive quantity (W), stand-off distance (R), and detonation depth (H). For the experiments, the explosive used was TNT, with quantities (W) ranging from 0.25 kg to 0.8 kg. The stand-off distance (R) varied from 0.0 m to 7.0 m, representing the distance between the explosive source and the target structure. The detonation depth (H) was considered in the range of 0.25 m to 2.0 m. To evaluate the responses under various explosion loads, four quantities were measured for each of the 24 conditions: surface pressure, strain, displacement, and acceleration. These measurements were crucial in assessing the structural behavior and dynamic responses of the target RC column under different UNDEX scenarios. To ensure data reproducibility and reliability, each test was repeated three times by Zhuang et al. (2020) [25].

For the UNDEX modeling in this study, the scenario consisting of explosive quantity (W) of 0.80 kg, stand-off distance (R) of 1.0 m, and detonation depth (H) of 1.0 m was selected. In order to validate the UNDEX model, a thorough comparison was made between the peak values of the displacement-time histories obtained from the experimental results and the simulation results. This comparison served as the primary metric and criterion for assessing the agreement between the two datasets. Figure (4.9) illustrates the comparison between the peak values of displacement-time histories obtained from the experimental and simulation results. Zhuang et al. recorded a maximum x-displacement of 52.92 mm for the explosive quantity W = 0.80 kg in their experiments, as shown in Figure (4.9).

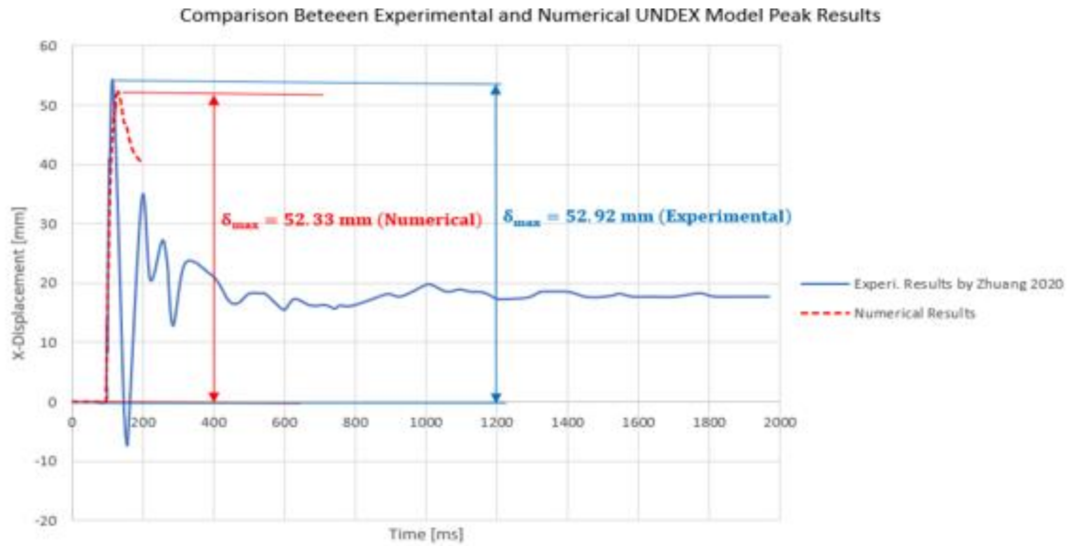

Figure 4. 9 Displacement time histories (Zhuang et. al. 2020) [26] and (this study)

In the current study, the numerical model yielded a maximum x-displacement of 52.33 mm for the same explosive quantity. The resulting discrepancy between the experimental and numerical results was excellent with only 1.11% deviation.

It is worth noting that the termination time for this UNDEX simulation study was set up at 100 milliseconds (0.1 seconds), while Zhuang et al.'s displacement sensors recorded the actual explosion for 2,000 milliseconds (2 seconds) as shown in Figure (4.9). The decision to employ a shorter run time in this study was due to the extensive computational time required to complete a single model run using a standalone personal computer. Despite the aforementioned limitation regarding the termination time discrepancy, a notable observation is made regarding the numerical model's ability to predict the maximum displacement obtained from Zhuang et al.'s experimental result for the test consisting of explosive quantity (W) of 0.80 kg, stand-off distance (R) of 3.0 m, and detonation depth (H) of 1.0 m.

4.3.2 Damage Profiles

This paragraph describes the findings of Zhuang et al. (2020) regarding the overall deformation and damage profiles of RC column under different explosive quantities, but with constant stand -off distance, R = 1 0 m and depth of detonation, H = 1.0 m Figure 4.10 illustrates the deformation patterns based on their experimental results. When the explosive quantity (W) was 0.20 kg with its Proportional stand-off distance $\bar{R}$ = 1.71, the column exhibited slight deformation, with a maximum residual displacement of 2.0 mm and no noticeable damage. However, with W = 0.40 kg ($\bar{R}$ = 1.36), the bending deformation increased, resulting in a maximum residual displacement of 13.56 m. Transverse tensile failure cracks were observed on the back surface, but they did not propagate into the upwind surface. Figure 4.10(c) demonstrates the case of W = 1.60 kg ($\bar{R}$ = 0.85), where the column body experienced significant bending and deformation. The maximum residual displacement at the midpoint was measured as 37.72 mm. Additionally, multiple circumferential cracks were observed near the midpoint of the column, and shear failure cracks were present near the column foot. These findings provide insights into the varying degrees of deformation and damage caused by different explosive quantities on the RC column (Zhuang et al. 2020).

Unfortunately, Zhuang et al. (2020) did not provide experimental damage profiles for the explosive quantity of W = 0.80 kg, which hinders a comprehensive comparison effort. As previously mentioned in Sections (4.2.1) and (4.3.1), the numerical model in this study was calibrated based on one scenario from Zhuang et al.'s (2020) experimental study, specifically W = 0.80 kg, R = 1.0 m, and H = 1.0 m. Originally, the intention was to further validate the model by calibrating and verifying it using a second scenario involving W = 0.40 kg, R = 1.0 m, and H = 1.0 m, in order to strengthen the overall validation of the model. However, this plan could not be executed due to the extensive computational time required to complete a single model run using a standard personal computer, as also discussed in Section (4.3.1).

Although there is a lack of recorded experimental data for the damage profile corresponding to W = 0.80 kg in Zhuang et al.'s publication (2020), efforts were made to cross-check the numerical results with available damage profiles discussed earlier in this section. Consequently, the numerical results in this study for W = 0.80 kg, R = 1.0 m ($\bar{R}$ = 1.08), and H = 1.0 m are expected to lie between the two cases depicted in Figure 4.11(b) and (c). The stand-off distance and detonation depth are consistent between the experimental and numerical cases. Based on the test results, the residual displacements for the three scenarios are as follows: for W = 0.40 kg, $\delta_{(Res\_0.40)}$ = 13.56 mm; for W = 0.80 kg, $\delta_{(Res\_0.80)}$ = 18.31 mm; and for W = 1.60 kg, $\delta_{(Res\_1.60)}$ = 37.72 mm.

Figure 4. 10 Deformation of experiment models (Zhuang et al. 2020).

Considering the similar parameters involved, it is reasonable to assume that the damage profiles obtained from the numerical model in this study for W = 0.80 kg can be interpolated and compared with Zhuang et al.'s experimental damage profiles shown in Figure 4.10. Based on these assumptions, the damage profiles from the current study were cross-checked. The observations indicate reasonable agreement with the descriptions provided in the first paragraph of this section and the findings shown in Figure 4.10. For example, it was previously reported that significant bending and deformation occurred in the RC column for the case of W = 1.60 kg ($\bar{R}$ = 0.85). Similarly, the damage profile obtained from the numerical model for W = 0.80 kg ($\bar{R}$ = 1.08), as shown in Figure 4.11, exhibits significant bending and cracks near the midpoint of the RC column. Additionally, Figure 4.12 shows the presence of shear failure cracks near the column footing, which also aligns with the findings reported for W = 1.60 kg in Zhuang et al.'s test results discussed earlier in this section. Consequently, these cross-checks can be considered as an additional means of validating the numerical model in this study.

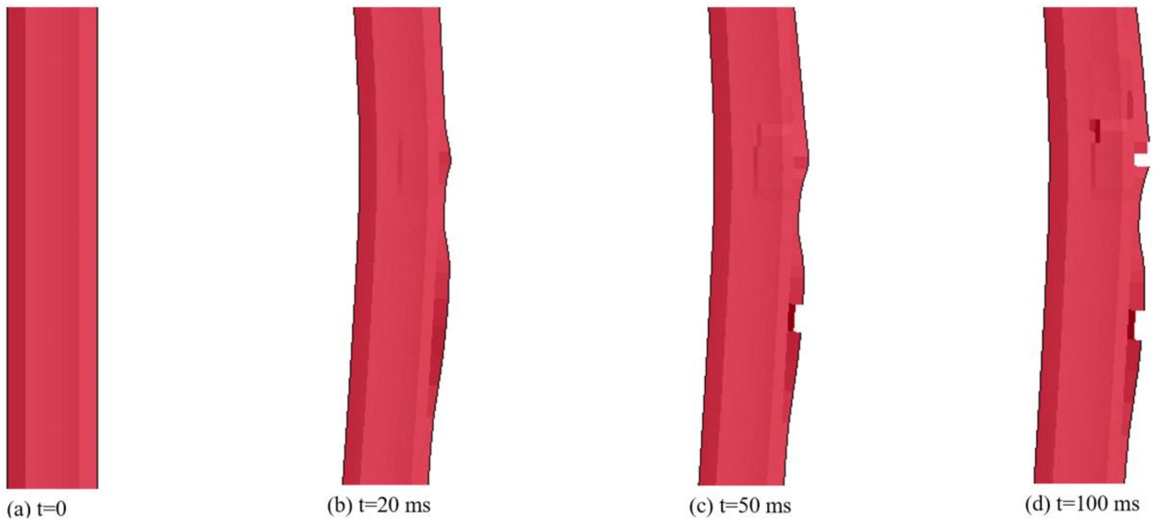

Figure 4. 11 Damage profile near the center of RC column (this study)

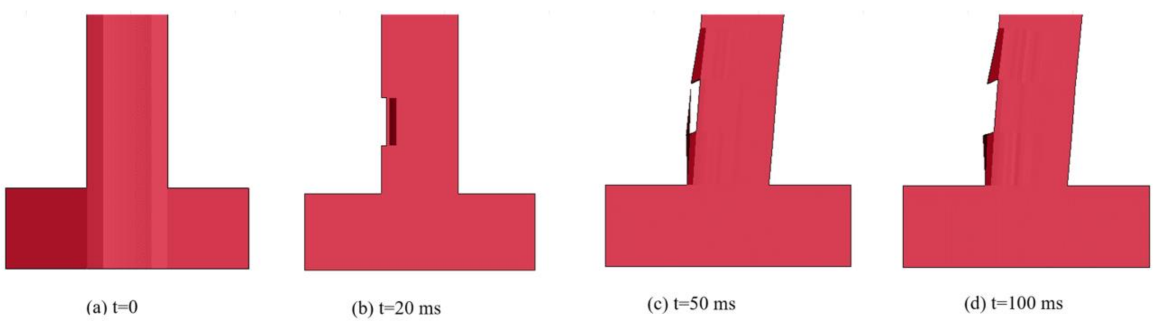

Figure 4. 12 Damage profile near the footing of RC column (this study)

The numerical model, as shown in Figures 4.11 and 4.12, exhibits a slightly higher level of damage compared to the experimental results presented in Figure 4.10. Several potential explanations for the observed discrepancies in the numerical results are discussed herein. When TNT explosive detonates, it generates a strong shock wave that propagates faster in water than in the air medium towards the RC column. This disparity can be attributed to the significant difference in density between water and air. Due to the closer proximity of water molecules compared to air molecules, there are more particles available to transmit and carry the energy of the shock wave. Consequently, shock waves in water encounter a greater number of particles to interact with, facilitating a more efficient transfer of energy and allowing for faster propagation. Additionally, the speed of sound, which denotes the velocity at which pressure disturbances, including shock waves, travel through a medium, generally tends to be higher in denser materials. Considering that water has a higher density than air, the speed of sound in water surpasses that in air.

Upon interaction with the column, the shock wave transfers a substantial amount of energy to the surface of the concrete. This sudden and intense energy transfer results in the generation of high-stress waves that propagate through the material of the column. In the case of the UNDEX TNT explosion, the shock waves propagate radially outward from the detonation point and impact the RC column, as illustrated in Figure 4.13. While moving through the water, these waves form a distinct wavefront characterized by rapid oscillations between high and low pressures, creating a high-pressure zone. This wavefront travels through the water medium, exhibiting an alternating pressure pattern.

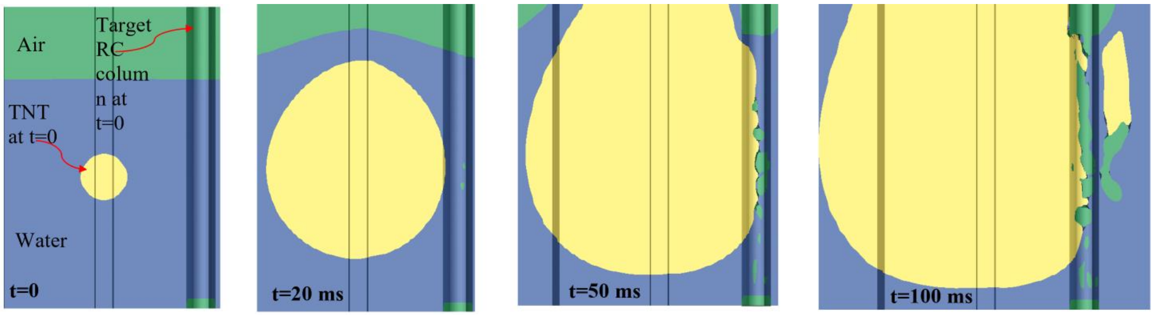

Figure 4. 13 Propagation of shock waves in UNDEX model (this study).

As the shock wave advances through the column, it generates a tensile stress wave that surpasses the tensile strength of the concrete on the opposite side. This occurs due to the reflection of the compressive wave at the surface. The presence of this tensile stress wave further facilitates the growth and propagation of cracks within the concrete material. As these cracks continue to spread, spallation of the concrete takes place. Spallation refers to the fracturing and separation of the concrete from the underlying reinforcement. The extent of concrete damage shown in the numerical model, as in Figures 4.11 and 4.12, can be attributed to those possible explanations discussed above. Moreover, several other factors may also be accounted for the observed slightly higher level of damage in the current numerical model. These factors include but are not limited to the strength and quality of the concrete and steel reinforcing material models, the details of reinforcement arrangement, the meshing details and several other parameters and assumptions employed during the numerical modeling and running stages. These observations, presented in Figures 4.11 and 4.12, provide additional supportive evidence for the validation of the UNDEX numerical model developed in this chapter.

CHAPTER FIVE

5.1 Introduction

This parametric study examines the effects of blast loads from TNT explosive charges on RC columns. Using a validated UNDEX model from chapter 4, various parametric studies were conducted to analyze the effects of stand-off distance, charge weight, and water depth. using LS-DYNA. The parametric study considered different charge weights (0.40, 0.80, and 1.20 kg equivalent weight of TNT), stand-off distances (0, 0.50 , 1.0, and 1.5 m), and different water depths (2.25, 1.75, 1.24, 0.75, and 0.25 m). A total of 60 cases were studied in this investigation.

To improve computational efficiency, the full-scale water tank used for UNDEX validation in chapter 4 (10 m diameter and 3.1 m height) was reduced to a smaller volume of 3 m x 3 m x 3 m x 3 m, as shown in Figure 5.1. The input data for this parametric study are provided in Table 5.1. Figure 5.2 illustrates a sample variation of the stand-off distance while maintaining a constant water depth (Z = 2.25 m), column height (H = 1.25 m), and charge weight (W = 0.40 kg). It is important to note that the depth of detonation was kept constant from top of the column footing to the midpoint of the RC column as H = 1.25 m, which is equivalent to 1.0 m from the water's free surface at its maximum height (Z = 2.25 m).

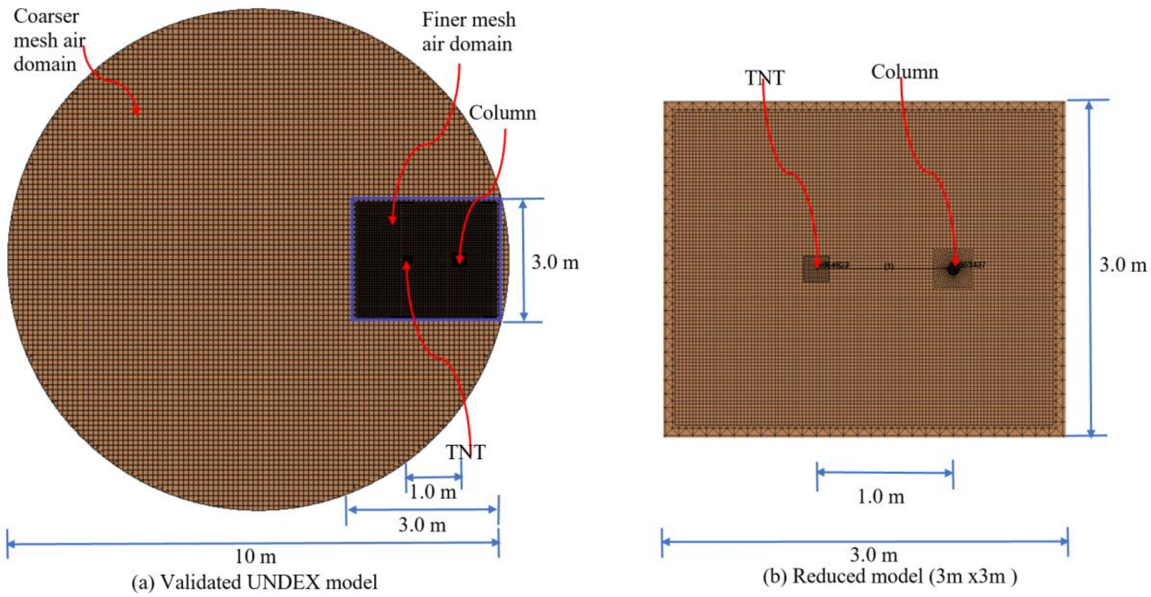

Figure 5. 1 Validated and reduced models for parametric study

Three numerical ‘sensors’ (*HISTROY_NODE_ID) were defined at the midpoint of the RC column: front side, column center, and back side. These conditions were uniform across all 60 cases. Figure 5.3 displays a sample variation in the depth of the water surface while keeping the radius (R) at 1.0 m, column height (H) at 1.25 m, and charge weight (W) at 0.40 kg constant. In case 07, with Z = 1.25 m, the water level coincides precisely with the midpoint of the RC column. The TNT equivalent explosive is partially submerged, meaning it is halfway in the air and halfway in the water. This presents a unique scenario where the LS-DYNA keyword *INITIAL_VOLUME_FRACTION cannot be used-

Table 5. 1 Input data employed in the parametric study.

Parametric Study Model Pameters											
Case No	Z	R	W	Case No	Z	R	W	Case No	Z	R	W
1	2.25	0.50	0.40	21	2.25	0.50	0.80	41	2.25	0.50	1.20
2	1.75	0.50	0.40	22	1.75	0.50	0.80	42	1.75	0.50	1.20
3	1.25	0.50	0.40	23	1.25	0.50	0.80	43	1.25	0.50	1.20
4	0.75	0.50	0.40	24	0.75	0.50	0.80	44	0.75	0.50	1.20
5	0.25	0.50	0.40	25	0.25	0.50	0.80	45	0.25	0.50	1.20
6	2.25	1.00	0.40	26	2.25	1.00	0.80	46	2.25	1.00	1.20
7	1.75	1.00	0.40	27	1.75	1.00	0.80	47	1.75	1.00	1.20
8	1.25	1.00	0.40	28	1.25	1.00	0.80	48	1.25	1.00	1.20
9	0.75	1.00	0.40	29	0.75	1.00	0.80	49	0.75	1.00	1.20
10	0.25	1.00	0.40	30	0.25	1.00	0.80	50	0.25	1.00	1.20
11	2.25	1.50	0.40	31	2.25	1.50	0.80	51	2.25	1.50	1.20
12	1.75	1.50	0.40	32	1.75	1.50	0.80	52	1.75	1.50	1.20
13	1.25	1.50	0.40	33	1.25	1.50	0.80	53	1.25	1.50	1.20
14	0.75	1.50	0.40	34	0.75	1.50	0.80	54	0.75	1.50	1.20
15	0.25	1.50	0.40	35	0.25	1.50	0.80	55	0.25	1.50	1.20
16	2.25	0.00	0.40	36	2.25	0.00	0.80	56	2.25	0.00	1.20
17	1.75	0.00	0.40	37	1.75	0.00	0.80	57	1.75	0.00	1.20
18	1.25	0.00	0.40	38	1.25	0.00	0.80	58	1.25	0.00	1.20
19	0.75	0.00	0.40	39	0.75	0.00	0.80	59	0.75	0.00	1.20
20	0.25	0.00	0.40	40	0.25	0.00	0.80	60	0.25	0.00	1.20

to define a sphere representing the TNT for the entire volume of either water or air. Therefore, for this special partially submerged explosion, such as in case 08, the entire domain was considered as air to define the sphere for the TNT, and a *SET_SEGMENT keyword was utilized to model the water. In all other cases, the TNT is either fully submerged in water or entirely above the water in the air. This condition results in three types of explosions in this parametric study: UNDEX, partially submerged, and air explosions. Both contact and non-contact explosions were considered for these three cases in the study. The subsequent sections present selected simulation results using discussion, graphs, and figures.

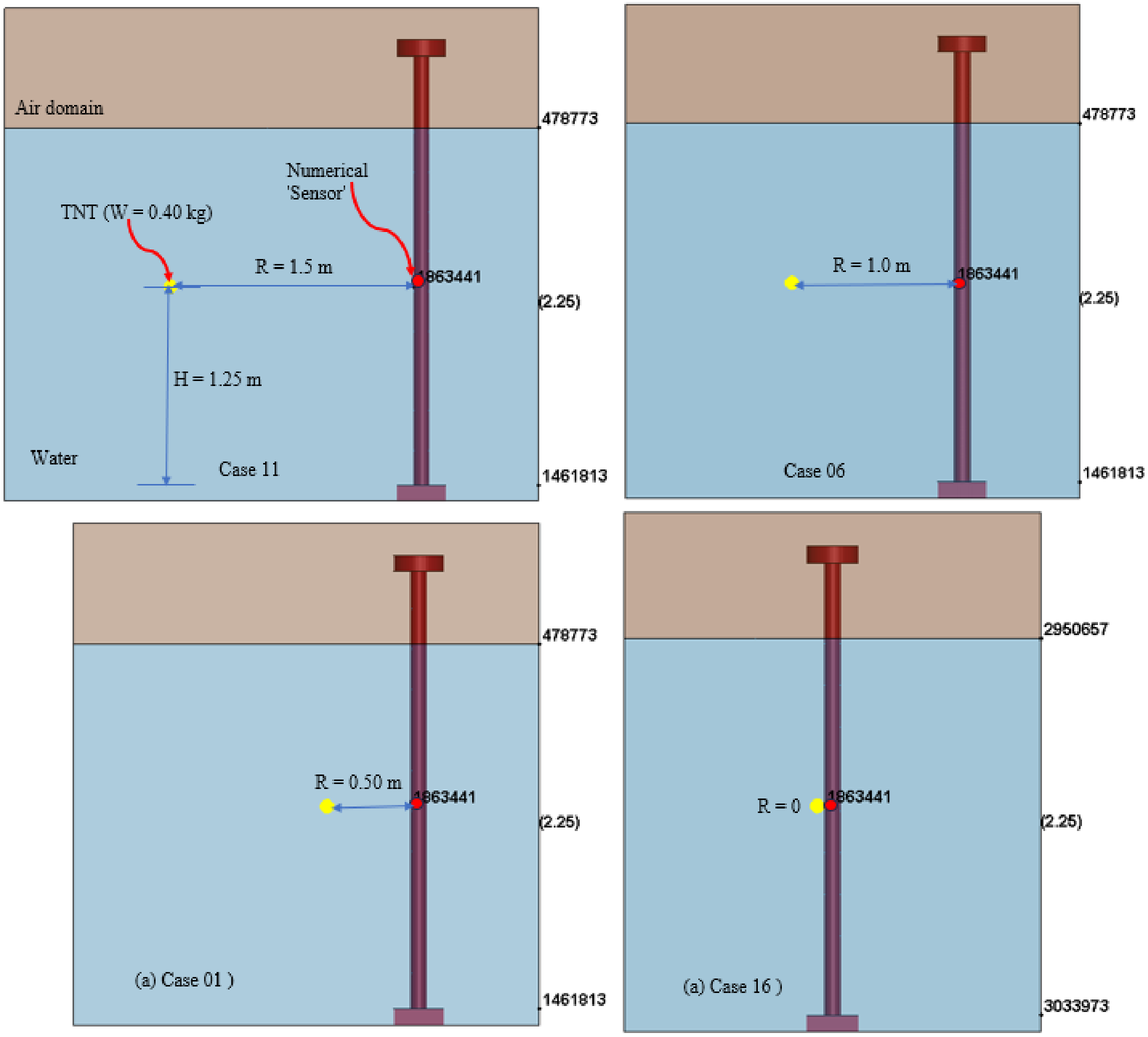

Figure 5. 2 Variation of stand-off distance taken at constant Z = 2.25 m, H =1.25m, & W =0.40 kg

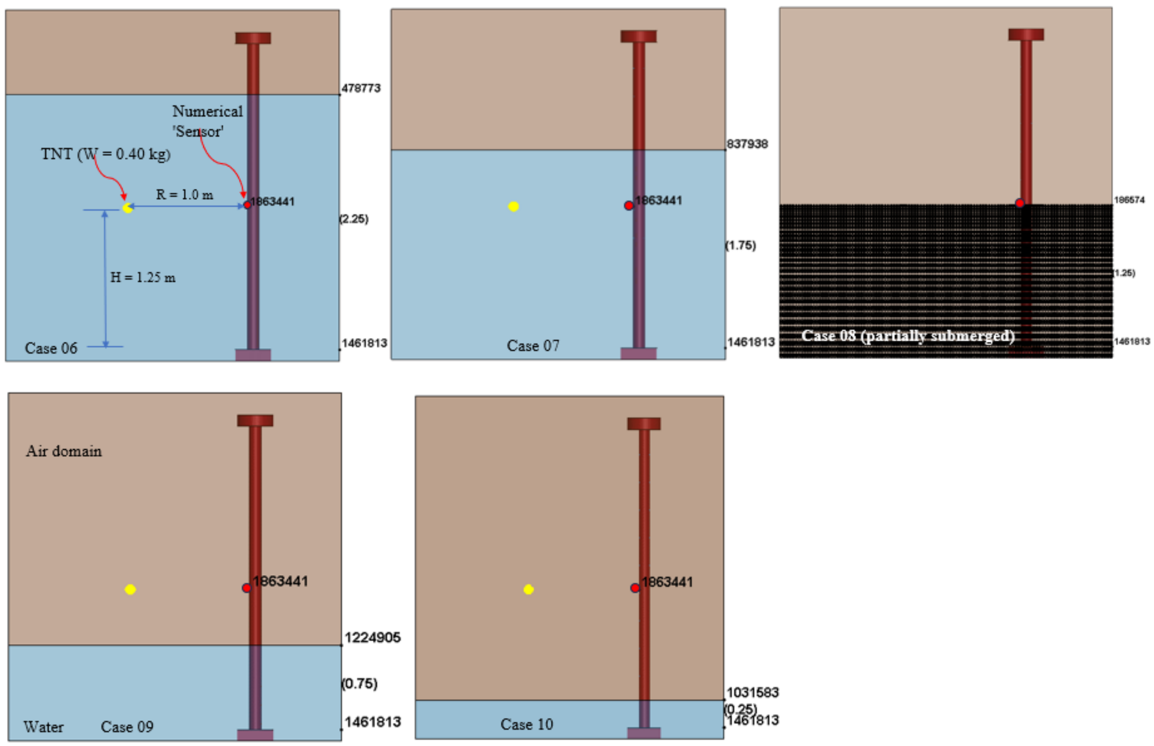

Figure 5. 3 Variation of depth of water surface at constant, R = 1.0 m, H =1.25m and W =0.40 kg

5.2 Effects of Explosive Weights

Figure 5.4 illustrates the relationship between displacement and explosive quantity. By considering three different weights of TNT (0.40 kg, 0.80 kg, and 1.20 kg), while maintaining constant stand-off distances within each subgroup and a depth of water (Z = 2.25m) (refer to case 06 in Figure 5.2) and burst height (H = 1.25 m), a noticeable trend emerges regarding the maximum displacements experienced by the midpoint of the RC columns. The figure demonstrates that as the weight of the TNT charge increases, there is a corresponding increase in the maximum displacements experienced by the midpoint of the RC columns. This pattern aligns with expectations, as greater TNT weights generate higher blast energy, resulting in more substantial destructive effects on the columns. For instance, Figure 5.4 displays a peak displacement value of 175 mm from a contact explosion with a weight of W = 1.20 kg. Additionally, the data points in Figure 5.4 conform well to the projected exponential trendline.

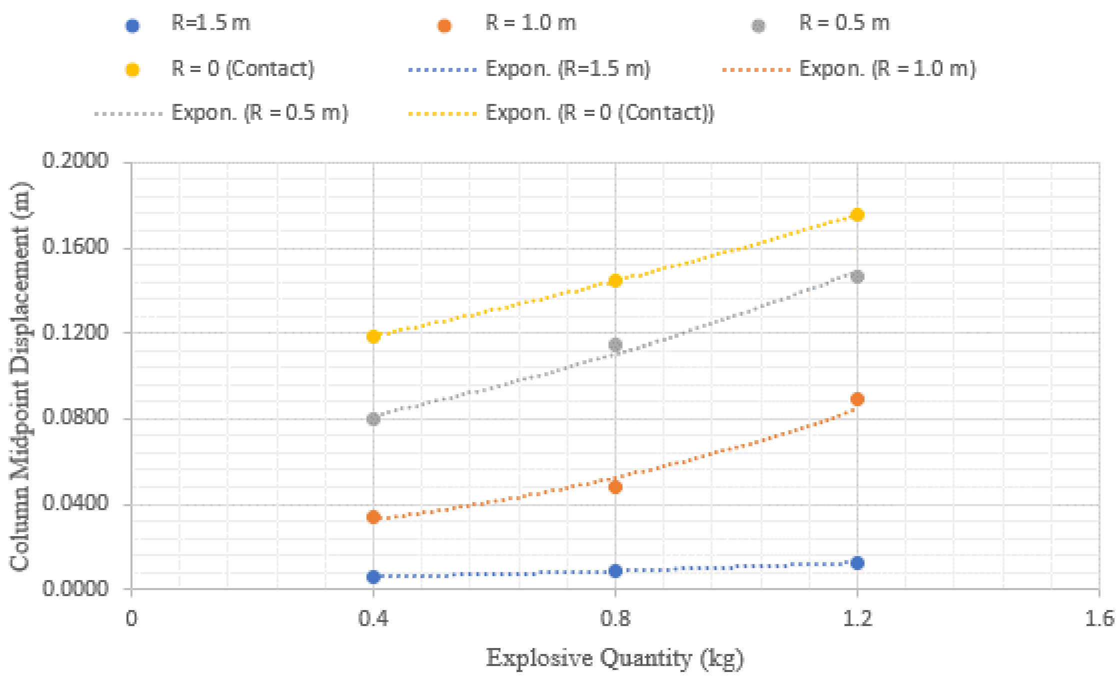

Figure 5. 4 Relationship between maximum displacement and explosive quantity

5.3 Effects of Stand-Off Distance

Figure 5.5 shows simulation results of the RC column with varying stand-off distances ranging from 0 m to 1.5 m. The explosive quantity is kept constant at W = 0.80 kg, with a depth of burst of H = 1.25 m, and water depths ranging from 2.25 m to 0.25 m. This simulation includes both contact and non-contact explosions, with contact explosions at a stand-off distance of R = 0 exhibiting larger displacements. For instance, at a water depth of Z = 1.75 m, a maximum midpoint displacement of approximately 165 mm is observed. It is noteworthy that, in Figure 5.4, between stand-off distances of 0 and 0.5 m, the relatively shallower water depth of Z = 1.75 m generates larger displacements compared to the deeper water level of Z = 2.25 m, which appears unusual.

Furthermore, as shown in the graph, increasing the stand-off distance leads to a significant reduction in displacements. Similarly, Figure 5.6 illustrates the effects of stand-off distance on the column midpoint for W = 1.20 kg. In this case, for a depth of water Z = 1.25 m and partially submerged explosion, there is an exponential relationship between stand-off distance and midpoint displacement. The data points align perfectly with the exponential trendline, indicating an exponential increase in peak lateral displacement of the RC column as the stand-off distance decreases, specifically for partially submerged explosion cases shown in Figure 5.6. From Figure 5.5, it becomes evident that reproducing the well-established facts showing a correlation between column damage and decreased stand-off distance, leading to increased displacement at the midpoint. Additionally, it can be inferred that in the partially submerged case (Z = 1.25 m), the peak displacement at the column's midpoint experienced a maximum reduction (approximately 80%) at a stand-off distance of R = 0.5 m compared to deeper water explosions. Further discussions on this topic will be presented in section 5.4.

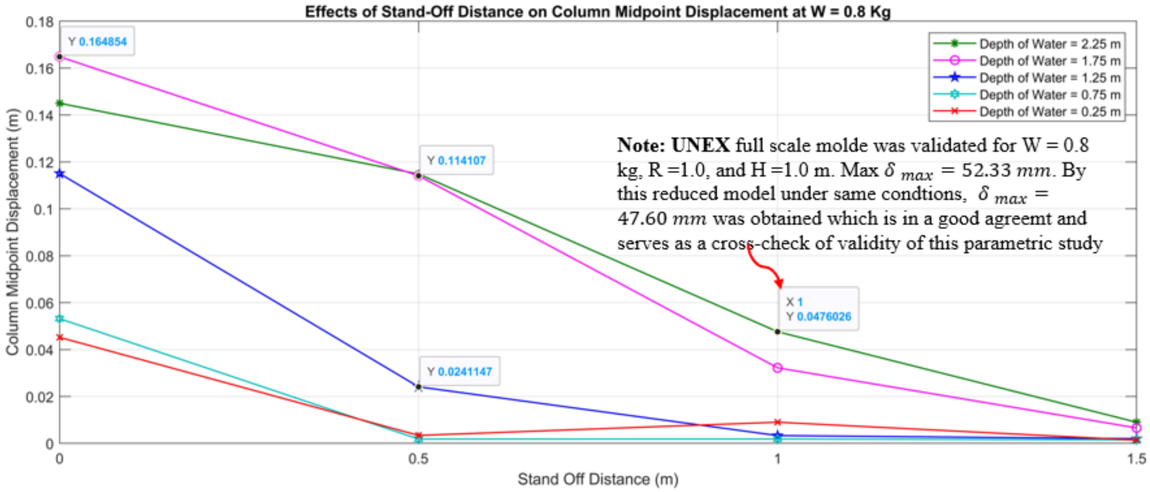

Figure 5. 5 Effects of stand-off distance

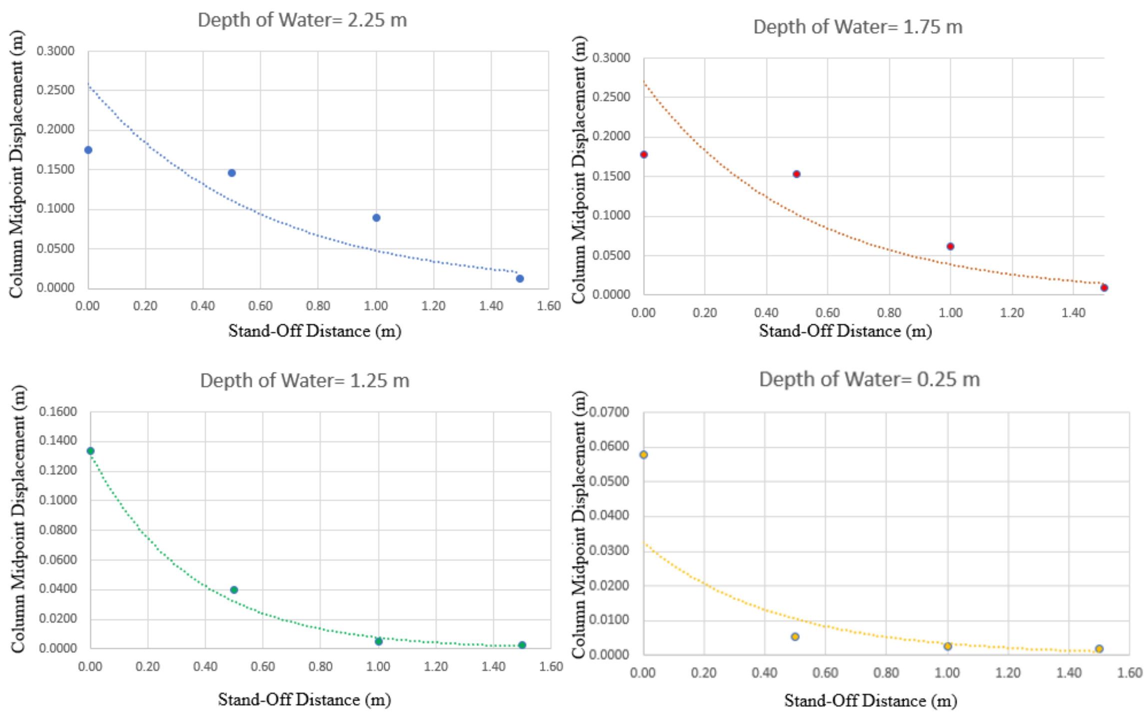

Figure 5. 6 Trends in effects of stand-off distance on column midpoint at W = 1.20 Kg

5.4 Effects of Depth of Water

To examine the impact of water depth, multiple simulations were conducted with varying levels from 2.25 m to 0.25 m while keeping the charge depth constant. Figure 5.5 illustrates the results, showing a significant reduction in peak displacement at the column midpoint. Contact explosions at R = 0 experienced a 30% reduction, while explosions at a stand-off distance of R = 0.5 m showed an approximately 80% reduction. These reduction trends were observed in simulations of partially submerged charges at a water depth of 1.25 m as half immersed, in comparison to deeper explosions at depths of 1.75 m and 2.25 m, for fully immersed conditions. Additionally, Figure 5.5 demonstrates that for a fixed shallow explosion depth, larger decreases in displacement are observed as the distance from the source increases.

The observed results of the partially submerged explosion phenomenon can be partly explained by the following theoretical background. When an explosion occurs partially in air and partially in water, it initiates a complex interaction between the explosive force and the surrounding medium. As the shockwave reaches the water-air interface, various phenomena take place. The shockwave partially reflects back into the air and partially transmits into the water, as depicted in Figures 5.7(b) and 5.9(b).

In the case of a surface explosion, the gas bubble generated by the charge rapidly dissipates into the atmosphere, resulting in the absence of subsequent bubble oscillation pressure pulses. As a result, the shock wave becomes the primary mechanism for transmitting energy through the water, and the reflection of the shock wave from the free surface is not a significant concern, as indicated in Figures 5.7(b) and 5.9(b). Additionally, there is a considerable decrease in both pressure and positive impulse compared to an explosion that is entirely surrounded by water. However, it is important to note that there is limited available data for surface explosions compared to fully submerged bursts (Sulfredge et al., 2005) [55].

Both the surface-reflected wave and the bottom-reflected wave play a crucial role and can have an impact comparable to or even greater than that of the direct wave. The surface-reflected wave, characterized as a rarefaction or tension wave, has the ability to significantly reduce the direct shockwave through a cutoff effect, which this can be attributed to the observed peak displacement reduction in the partially submerged explosion case.. It is noteworthy that the reflected wave travels faster than the direct wave in the vicinity of the water-air interface, and both waves travel faster than the speed of sound in water (Eneva et al., 1999) [56]. Figure 5.8 illustrates the propagation of the pressure shockwave and the complex interactions between ALE materials, TNT, water, and air in the UNDEX simulation results (case 06). For clarity purposes, only the ALE water material and the driving shockwave are shown in the all other simulation results, while the interaction among TNT, water, and air ALE materials is displayed separately in Figure 5.8.

Figures 5.7 to 5.11 show the effects of water depth on the displacement of the column midpoint for non-contact (R = 1.0 m) and contact (R = 0) explosions. In both cases, it is evident that as the water depth increases, the peak displacement also increases, aligning with expectations. This is attributed to a combination of hydrodynamic effects and other factors. In deep water explosions, hydrodynamic effects play a significant role in intensifying the blast. The density and incompressibility of water facilitate efficient energy transmission, while the greater water volume above the explosion in deeper depths enables enhanced energy transfer.

Figure 5.11 specifically shows that for non-contact explosions, the effects of water depth are not significant within the range of 0.25 m through the partially submerged case at Z = 1.25 m. However, for depths beyond the partially submerged level, the effects become increasingly pronounced, especially with higher explosive weights. On the other hand, for contact explosions, the effects of varying water depth begin with gentle slope to show even from Z = 0.25 m and continue to increase with higher water depths. The simulation results in Figure 5.11 provides further insight.

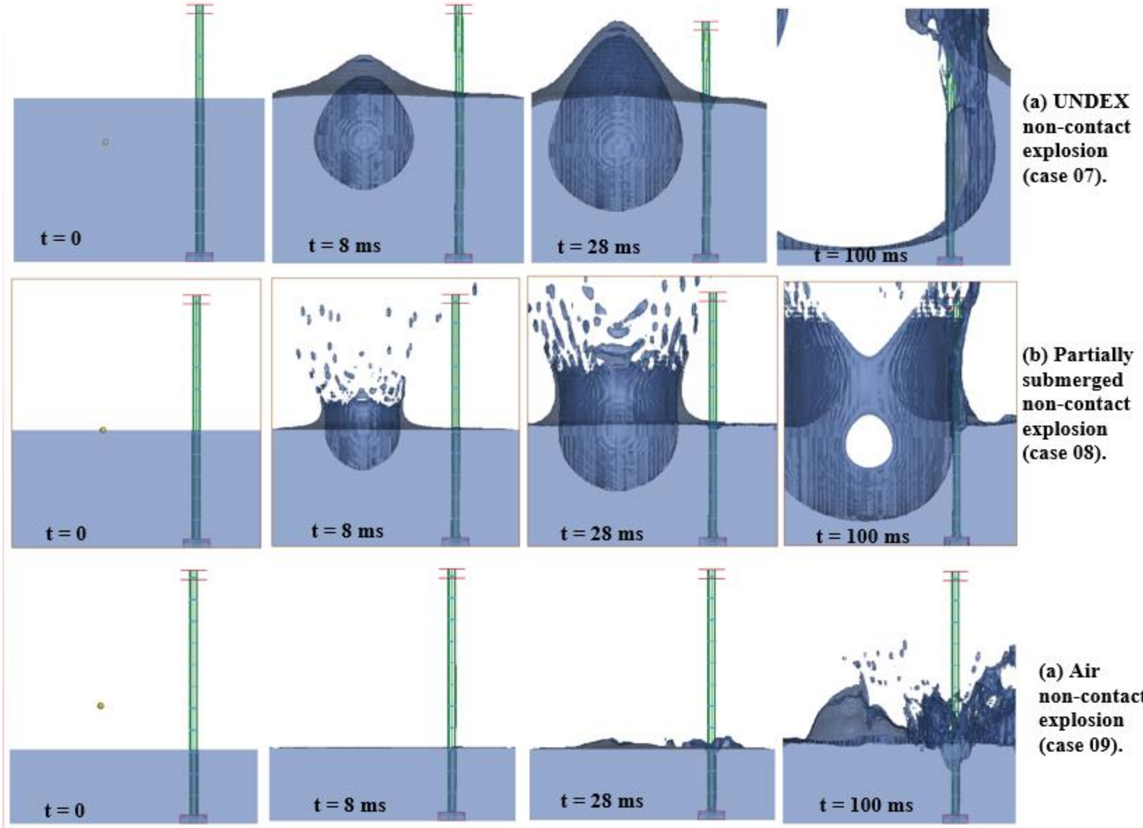

Figure 5. 7 Non-contact explosions simulation results for (a) UNDEX, (b) Partially submerged, (c) Air.

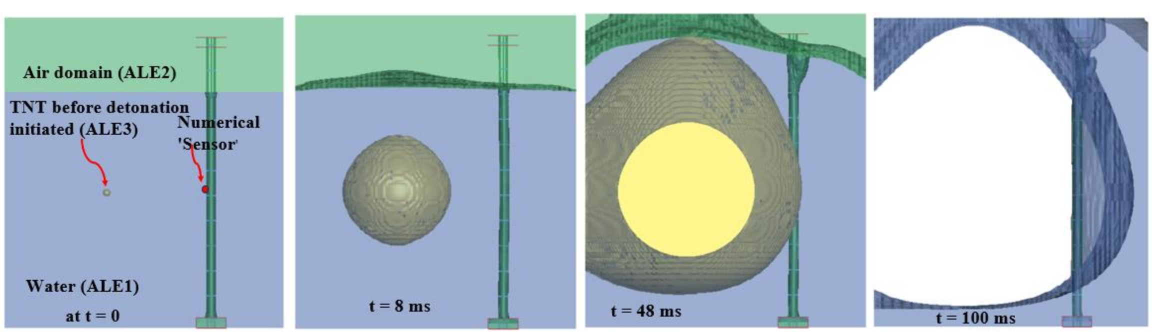

Figure 5. 8 Propagations of pressure shockwave and interactions of ALE materials, TNT, water, & air UNDEX simulation results (case 06)

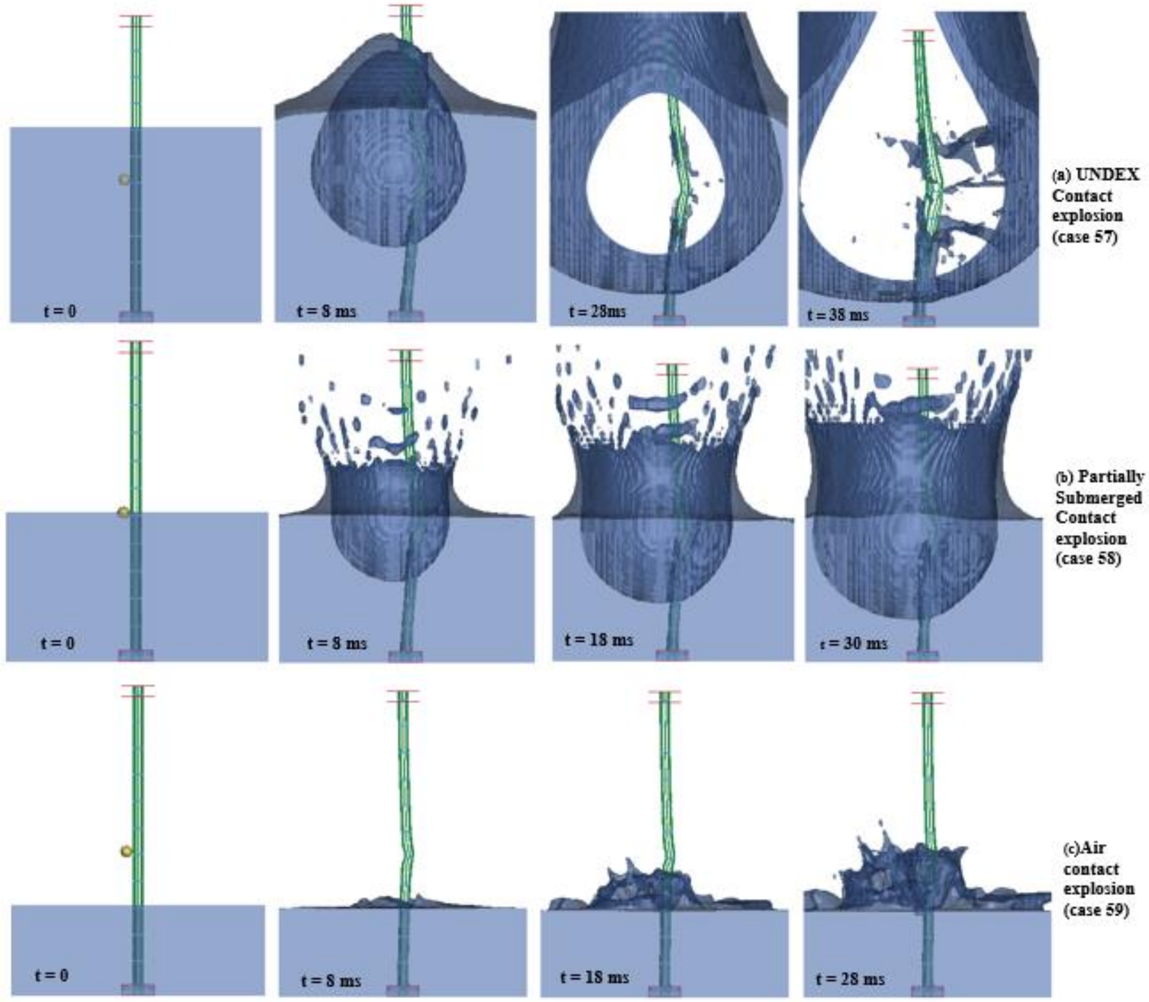

Figure 5. 9 Contact explosions simulation results for (a) UNDEX, (b) Partially submerged, (c) Air.

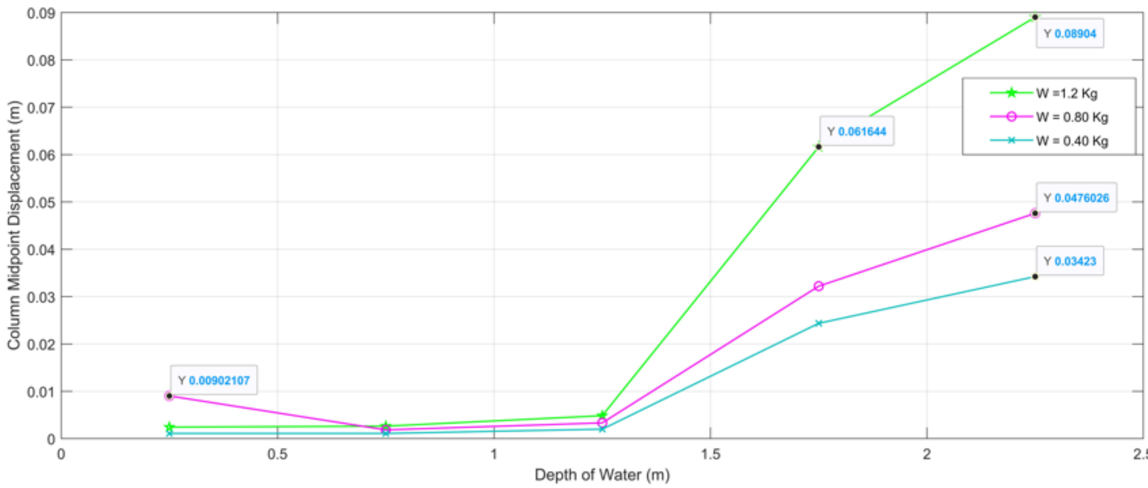

Figure 5. 10 Effects of depth of water on column midpoint displacement at R = 1.0 m (Non-contact explosion)

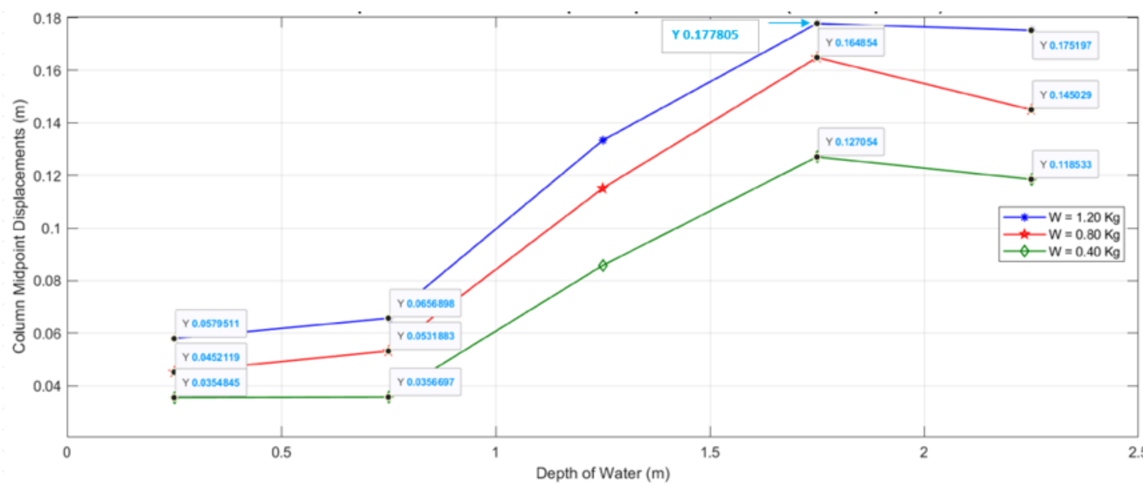

Figure 5. 11 Effects of depth of water on column midpoint displacement at R = 0 m (Contact explosion)

In summary, the findings of this parametric study highlight that the effects of air blast and underwater explosion loads resulting from TNT charges on RC columns increase with greater weight of equivalent explosives, deeper water levels, and shorter stand-off distances from the detonation source. Furthermore, the study also examines the effects of partially submerged, contact, and non-contact explosions on RC columns.

CHAPTER SIX

6.1 Conclusion

The following conclusions can be made from the air blast and UNDEX studies: -

In chapter 3, a comprehensive numerical model for air blast responses of RC columns was developed and validated using LS-DYNA. The validation process involved comparing the simulation results with experimental data obtained from previous studies, namely Yuan et al. (2017) and Yang et al. (2019). The numerical model exhibited good agreement with the experimental findings, thereby demonstrating its accuracy and reliability in replicating real-world blast scenarios.

In chapter 4, the modeling and validation of UNDEX responses of RC column was presented. The numerical model was calibrated and validated using experimental tests conducted by Zhuang et al. (2020). The UNDEX model was created using LS-DYNA, considering various aspects such as meshing, boundary conditions, material models, ALE coupling, erosion algorithm, simulation procedures, and output controls. The model was validated by comparing the peak displacements from the simulation with the experimental results, showing a good agreement with a deviation of 1.11%. The findings suggest that the numerical model is capable of predicting the response of behavior of RC columns subjected to UNDEX.

In chapter 5, a parametric study was conducted to analyze the effects of blast loads from TNT explosive charges on RC columns. The study considered various parameters such as stand-off distance, charge weight, and water depth. A total of 60 numerical simulations were run. The results obtained from the simulations provided valuable insights into the behavior of RC columns under different blast load scenarios.

It was observed that as the weight of the TNT charge increased, there was a corresponding increase in the maximum displacements experienced by the midpoint of the RC columns.

The study also revealed that the stand-off distance between the explosive source and the RC column had a significant impact on the column's response to blast loads. It was observed that decreasing the stand-off distance led to increased displacements at the midpoint of the column, indicating higher damage levels. Conversely, increasing the stand-off distance resulted in a significant reduction in displacements. This trend was particularly prominent in the case of partially submerged explosions.

It was observed that as the water depth increases, the column midpoint displacement also increases, aligning with expectations.

Compared to fully immersed and deeper explosions, partially submerged explosions exhibited a significant reduction in peak displacement, ranging from 30% to approximately 80%. Additionally, for partially submerged explosions, a clear exponential relationship between stand-off distance and midpoint displacement was observed, with the data points aligning perfectly with the exponential trendline.

Overall, this thesis study's significance lies in its pioneering work on investigating RC columns exposed to partially submerged explosions, addressing a notable knowledge gap in the existing literature. The literature review revealed limited research in this field, with no open-source materials available on the behavior of RC columns under partially submerged explosions. Through the parametric study, this thesis was able to conduct initial investigations into RC columns subjected to partially submerged explosions, partly filling the knowledge gap in this specific research area. Furthermore, the findings make valuable contributions to mitigating damages to critical offshore infrastructures, including RC bridge columns and water transport, particularly in the context of emerging maritime terrorism.

6.2 Limitations

This parametric study utilized a reduced-scale model of the water tank for computational efficiency. While this approach can be practical, it may not fully capture the complexities and intricacies of a full-scale blast scenario. The reduction in scale could potentially affect the accuracy and representativeness of the results.

Although the study considered important parameters such as stand-off distance, charge weight, and water depth, there may be other factors that could influence the response of RC columns to blast loads. For example, the study did not explore the effects of column geometry, reinforcement detailing, or column material properties, which could be significant factors in real-world scenarios.

While the study used a validated UNDEX model, it did not explicitly mention the validation of the specific parametric cases studied. Experimental validation of the simulated results would provide a higher level of confidence in the accuracy and reliability of the findings.

6.3 Recommendations For Future Works

The study highlighted the unique behavior of partially submerged explosions and their impact on RC columns. Further research and experimental studies should be conducted to gain a deeper understanding of the mechanisms involved and to develop more accurate modeling techniques for such scenarios.

While the study utilized validated UNDEX models and finite element analysis, further validation and calibration of these models are recommended. Experimental data from blast tests on RC columns should be collected and used to validate and refine the simulation models, ensuring their accuracy and reliability.

The findings of this parametric study open avenues for further research and future works in the field of blast load analysis on RC columns. Some potential areas of focus include:

Material response and failure criteria: Investigating the material response of concrete and reinforcement under blast loads and developing accurate failure criteria will enhance the accuracy of blast load analysis. This could involve experimental testing and the development of constitutive models to capture the behavior of materials subjected to high-velocity dynamic loading.

Developing innovative protective measures and retrofitting techniques by incorporating applications of Artificial Intelligence (AI) to enhance the blast resistance of RC columns and structures will be crucial.

Finally, researchers seeking to expand work in the area of blast loading of structures are referred to a collection of papers co-authored by George Mason University professors, graduate students, and collaborators [57 - 80].

REFERENCES

1. Cole RH. Underwater Explosions. Princeton, New Jersey: Princeton University Press, 1948.

2. Zare A. Shock factor investigation in a 3-D finite element model under shock loading. Janghorban, M 2013.

3. Luki´ S, Dragani'c H. Blast Loaded Columns-State of the Art Review. Journal of Applied Sciences 2021.

4. Fouché P, Bruneau M, Chiarito VP. Modified steel-jacketed columns for combined blast and seismic retrofit of existing bridge columns. Journal of Bridge Engineering 2016; 21, 4016035.

5. Bruneau M, Lopez-Garcia D, Fujikura S. Multi-hazard-resistant highway bridge bent. In Proceedings of the Structures Congress 2006: Structural Engineering and Public Safety, 2006, 1–4.

6. Fujikura S, Bruneau M, Lopez-Garcia D. Experimental investigation of multi-hazard resistant bridge piers having concrete-filled steel tube under blast loading. Journal of Bridge Engineering 2008; 13, 586 –594.

7. Chipley M. Reference Manual to Mitigate Potential Terrorist Attacks Against Buildings: Providing Protection to People and Building. Washington, DC, 2003.

8. Fujikura S, Bruneau M. Experimental investigation of seismically resistant bridge piers under blast loading. Journal of Bridge Engineering 2010; 16, 63–71.

9. Burrell RP, Aoude H, Saatcioglu M. Response of SFRC columns under blast loads. Journal of Structural Engineering 2015; 141, 4014209.

10. Wang Z, Wu H, Fang Q, Wu J. Experimental study on the residual axial capacity of ultra-high performance cementitious composite filled steel tube (UHPCC-FST) column under contact explosion. Thin Walled Structures 2020; 147, 106515.

11. Yuan S, Haob H, Zonga Z, Li J. A study of RC bridge columns under contact explosion. Int J Impact Eng 2017; 109: 378–390.

12. Wu K-C, Li B, Tsai KC. The effects of explosive mass ratio on residual compressive capacity of contact blast damaged composite columns. Journal of Constructional Steel Research 2011; 67, 602–612.

13. Hao H, Stewart MG, Li Z-X, Shi Y. RC column failure probabilities to blast loads. International Journal of Protective Structures 2010; 1, 571–591.

14. Yi Z, Agrawal A, Ettouney M, Alampalli S. Blast load effects on highway bridges. I: modeling and blast load effects. Journal of Bridge Engineering 2014; 19(4):04013023.

15. Liu H, Agrawal A, Torres D, Yi Z, Liu G. Simplified blast-load effects on the column and bent beam of highway bridges. Journal of Bridge Engineering 2015; 20(10):06015001.

16. Magali A, Alain R, Chhim S. Numerical dynamic simulations for the prediction of damage and loss of capacity of RC column subjected to contact detonations. VIII International Conference on Fracture Mechanics of Concrete and Concrete Structures FraMCoS-8, 2013.

17. Yang G, Wang G, Lu W, Zhao X, Yan P, Chen M. Cross-section shape effects on anti-knock performance of RC columns subjected to air and underwater explosions. Ocean Engineering 2019; 181: 252–266.

18. Keil AH. The Response of Ships to Underwater Explosions. 1961.

19. US Office of Naval Research & British Department of Navy (USNRBD). Underwater Explosion Research: A Compendium of British and American Reports. 1950.

20. De Candia S. Experimental and Numerical Investigations into the Underwater Explosion Induced Whipping Response of Submerged Platforms. 2018.

21. Fox PK. Nonlinear Dynamic Response of Cylindrical Shells Subjected to Underwater Side-On Explosions. 1992.

22. Liu MB, Liu GR, Lam KY, Zong Z. Smoothed particle hydrodynamics for numerical simulation of underwater explosion. Computational Mechanics 2003; 30 (2) :106-118.

23. Seunggyu L, Cho J, Lee C, Cho S. Experimental and numerical investigations of near-field underwater explosions. Journal of Structural Engineering & Mechanics 2021; 77.

24. Sanders J, Urgessa G, Löhner R. Literature Review on the Response of Concrete Structures Subjected to Underwater Explosions. CivilEng 2021; 2(4), 895-908.

25. Zhuang T, Wang M, Wu J, Yang C, Zhang T, Gao C. Experimental investigation on dynamic response and damage models of circular RC columns subjected to underwater explosions. Defense Technology 2020.

26. Hansson H, Skoglund P. Simulation of Concrete Penetration in 2D and 3D with the RHT Material Model. Swedish Defense Research Agency 2002.

27. Chen WF. Plasticity in reinforced concrete. J Ross Publishing 2007.

28. Holmquist T, Johnson GR. A Computational Constitutive Model for Concrete Subjected to Large Strains, High Strain Rates, and High Pressures. Proceedings of the 14th International Symposium on Ballistics, 1993, 591-600., 1993.

29. Riedel W, Thoma K, Hiermaier S, Schmolinske E. Penetration of reinforced concrete by BETA-B-500 numerical analysis using a new macroscopic concrete model for hydrocodes. 9th Int. Symp. Interaction of the Effects of Munitions with Structures., 1999.

30. Ramberg W, Osgood WR. Description of stress-strain curves by three parameters, National advisory committee for aeronautics. 1943.

31. Menegotto M, Pinto P. Method of analysis for cyclically loaded reinforced concrete plane frames. IABSE symposium, 1973.

32. Chang GA, Mander JB. Constitutive Model for Confined Concrete. Journal of Structural Engineering, 1994; Volume 120.

33. Johnson GR, Cook WH. Fracture Characteristics of Three Metals Subjected to Various Strains, Strain Rates, Temperatures and Pressures. Engineering Fracture Mechanics 1985; Vol. 21, No. I: 3148.

34. LSTC (Livermore Technology Software Corporation). LS-DYNA Keyword User's Manual, Version 971. 2007.

35. ANSYS-LS. LS-DYNA: The advanced simulation tool for nonlinear, linear, dynamic, and static analysis. Predictive Engineering LS-DYNA Specialist, 2020.

36. ANSYS-LS-DYNA Inc. LS-DYNA Theory Manual 2023, R14. ANSYS, Inc, 2023.

37. LS-DYNA Support. Hourglass. 2021.

38. Klenow B. Assessment of LS-DYNA and Underwater Shock Analysis (USA) Tools for Modeling Far-Field Underwater Explosion Effects on Ships. 2006.

39. LSTC. LS-DYNA Theory Manual. LS-DYNA Dev (r:11261). Livermore Software Technology Corporation, 2019.

40. Skill-Lync. All About Time-Step in LS Dyna. 2022.

41. Li J, Hao H. Numerical study of concrete spall damage to blast loads. Int J Impact Eng 2014; 68:41–55.

42. Tabatabaei ZS, Volz JS. A Comparison between Three Different Blast Methods in LS-DYNA: LBE, MM-ALE, Coupling of LBE and MM-ALE. 12th International LS-DYNA ® Users Conference Blast/Impact (3), 2012.

43. Wang Z, Lu Y, Hao H, Chong K. A full coupled numerical analysis approach for buried structures subjected to subsurface blast. Comput Struct 2005.

44. Nazem M, Carter JP, Airey DW. Arbitrary Lagrangian–Eulerian method for dynamic analysis of geotechnical problems. Comput Geotech 2009; 36(4):549-557.

45. Aerospace Working Group. LS-DYNA Aerospace Working Group Modeling Guidelines. Version 21-1 2021.

46. LSTC. LS-DYNA ALE (Arbitrary Lagrangian Eulerian) Capabilities Fluid Structure Interaction Modeling. 2003.

47. Trevino T. Applications of Arbitrary Lagrangian Eulerian (ALE) analysis approach to underwater and air explosion problems. 2000.

48. Michaloudis G, Mattern S, Schweizerhof K. Computer Simulation for Building Implosion Using LS-DYNA. Proceedings of High Performance Computing in Science and Engineering, Stuttgart, Germany, 2011.

49. Horta LG, Mason BH, Lyle KH. A Computational Approach for Probabilistic Analysis of LS-DYNA Water Impact Simulations. International Journal of Crashworthiness 2010; 15.

50. Xu K, Lu Y. Numerical simulation study of spallation in reinforced concrete plates subjected to blast loading. Computers & Structures 2006; 84(5-6):431-8.

51. Glance Paul. Simulation of Impact Proof Testing of Electronic Sub-Systems. 12th International LS-DYNA Users Conference Blast/Impact (3), 2019.

52. Huynh HD, Natarajan S, Nguyen-Xuan H. Polytopal composite finite elements for modeling concrete fracture based on nonlocal damage models. Comput Mech 2020; 66: 1257–1274.

53. FEMA. Chapter 4 Explosive Blast. 1989.

54. Sadwin LD, Swisdak MM, Gitterman Y, Lotan O. Shock Wave Energy: Explosions in Air, Ground and Water. 30th International Symposium on Shock Waves, 2017, 1307–1311.

55. Sulfredge CD, Morris RH, Sanders RL. Calculating the Effect of Surface or Underwater Explosions on Submerged Equipment and Structures. 2005.

56. Eneva M, Stevens J. Analysis of Russian Hydro-acoustic Data for CTBT Verification. 1999.

57. Urgessa, G. S., & Arciszewski, T. (2011). Blast response comparison of multiple steel frame connections. Finite Elements in Analysis and Design, 47(7), 668-675.

58. Urgessa, G. S., & Maji, A. K. (2010). Dynamic response of retrofitted masonry walls for blast loading. Journal of Engineering Mechanics, 136(7), 858-864.

59. Maji, A. K., Brown, J. P., & Urgessa, G. S. (2008). Full-scale testing and analysis for blast-resistant design. Journal of Aerospace Engineering, 21(4), 217-225.

60. Rocco, J. A. F. F., Urgessa, G. S., Dutra, R. L., Gonçalves, R. F. B., Iha, K., & Mendonça, F. B. (2020). EPS foam blast attenuation in full-scale field test of reinforced concrete slabs. Acta Scientiarum. Technology, 42.

61. Urgessa, G. S. (2009). Finite element analysis of composite hardened walls subject ted to blast loads. Journal of Engineering and Applied Sciences, 2(4), 804-811.

62. Bondok, D., Salim, H., & Urgessa, G. (2021). Quasi-static responses and associated failure mechanisms of cold-formed steel roof trusses. Engineering Structures, 231, 111741.

63. Urgessa, G. S., & Esfandiari, M. (2018). Review of polymer coatings used for blast strengthening of reinforced concrete and masonry structures. In International Congress on Polymers in Concrete (ICPIC 2018) Polymers for Resilient and

Sustainable Concrete Infrastructure 16 (pp. 713-719). Springer International Publishing.

64. Mendonca, F. B., Urgessa, G. S., & Rocco, J. A. (2017, April). Blast Response of 60 MPa Reinforced Concrete Slabs Subjected to Non-Confined Plastic Explosives. In Structures Congress 2017 (pp. 15-26).

65. Mendonca, F. B., Urgessa, G. S., Almeida, L. E., & Rocco, J. A. (2021). Damage diagram of blast test results for determining reinforced concrete slab response for varying scaled distance, concrete strength and reinforcement ratio. Anais da Academia Brasileira de Ciências, 93.

66. Derseh, S. A., Urgessa, G., & Mohammed, T. A. (2023, June). Finite element analysis of the response of conventional and special reinforcement detailed concrete beams subjected to impact loads. In Structures (Vol. 52, pp. 57-82). Elsevier.

67. Mendonça, F., Urgessa, G., & Rocco, J. (2018). Experimental investigation of 50 MPa reinforced concrete slabs subjected to blast loading. Ingeniería e Investigación, 38(2), 27-33.

68. Mendonça, F. B., Urgessa, G. S., Augusto, A. S., & Rocco, J. A. (2020). Experimental records from blast tests of ten reinforced concrete slabs. CivilEng, 1(2), 51-74.

69. Mendonça, F. B., & Urgessa, G. S. (2018). Pre-Test and Analysis of a Reinforced Concrete Slab Subjected to Blast from a Non-Confined Explosive. In Energetic

Materials Research, Applications, and New Technologies (pp. 272-287). IGI Global.

70. Urgessa, G. S. (2006). Strengthening masonry structures using fiber-reinforced polymers to mitigate blast effects. The University of New Mexico.

71. Mendonça, F. B., Urgessa, G. S., Iha, K., Rocha, R. J., & Rocco, J. A. F. F. (2017). Investigation of Reinforced Concrete Slabs Behavior Against Blast Varying Scaled Distance and Steel Reinforcement Ratios. In XIX Defense Operational Applications Symposium.

72. Mendonça, F. B., Gonçalves, R. F., Urgessa, G. S., Iha, K., Domingues, M., & Rocco, J. A. (2018). Computational Chemistry Employment in Verification and Validation of Detonation Pressure of Plastic Explosive-Pbx. Química Nova, 41, 310-314.

73. Mendonça, F. B., Gonçalves, R. F., Urgessa, G. S., Iha, K., Domingues, M., & Rocco, J. A. (2018). Emprego de química computacional na verificação e validação da pressão de detonação de explosivo plástico-PBX. Química Nova, 41, 310-314.

74. Ali, E., & Urgessa, G. (2021, March). Numerical Simulation of Functionally-Graded-Material Pipes Under Blast Loading. In International Conference on Advances in Structural Mechanics and Applications (pp. 167-178). Cham: Springer International Publishing.

75. Sanders, J., & Urgessa, G. Response of Reinforced Concrete Columns Subjected to Underwater Explosions. In Structures Congress 2023 (pp. 1-9).

76. Augusto, A. S., Mendonça, F. B., Urgessa, G., & Iha, K. Pre-test input optimization of high explosive blast effects on steel sheets using finite element analysis. institutions, 6, 26.

77. Mendonça, F. B., Urgessa, G., Domingues, M. G., Iha, K., & Fidel, J. A. F. Efeitos do EPS na leitura de pico de pressão refletida em ensaio de campo com explosivo militar. CEP, 12228, 900.

78. Mendonça, F. B., Urgessa, G., de Almeida, L. E. N., Iha, K., & Jachura, R. Variação do Momento Linear de Lajes de Concreto Armado em Ensaios Experimentais com PBX. CEP, 12228, 900.

79. Augusto, A. S., Mendonça, F. B., Urgessa, G., & Iha, K. (2021). Finite Element Analysis of Experimentally Tested Concrete Slabs Subjected to Airblast. Defence Science Journal, 71(5).

80. Mendonca, F. B., Urgessa, G., Iha, K., Rocha, R. J., & Rocco, J. A. F. F. (2018). Comparison of predicted and experimental behaviour of RC slabs subjected to blast using SDOF analysis. Defence Science Journal, 68(2), 138.

BIOGRAPHY

Getu Z. Abyu received his Bachelor of Science in Civil Engineering from Jimma University in 2009. He was employed as a Graduate Teaching Assistant for George Mason University in 2022/23 academic year and received his Master of Science in Structural Engineering at George Mason University in 2023